EXPERIMENTAL EVALUATION OF A NACA 0021 AIRFOIL EMPLOYING SHAPE-MEMORY ALLOY FOR ACTIVE FLOW CONTROL

A Thesis
Submitted to the Graduate Faculty
of the
North Dakota State University
of Agriculture and Applied Science

By

Adam James Stolt

In Partial Fulfillment of the Requirements
for the Degree of
MASTER OF SCIENCE

Major Department:
Mechanical Engineering

March 2018

Fargo, North Dakota

North Dakota State University
Graduate School

Title

Experimental Evaluation of a NACA 0021 Airfoil Employing Shape-Memory Alloy for Active Flow Control

By

Adam James Stolt

The Supervisory Committee certifies that this ***disquisition*** complies with North Dakota State University's regulations and meets the accepted standards for the degree of

MASTER OF SCIENCE

SUPERVISORY COMMITTEE:

Dr. Jordi Estevadeordal
Chair

Dr. Yildirim Suzen

Dr. Ivan Lima Jr.

Approved:

4/6/2018
Date

Dr. Alan R. Kallmeyer
Department Chair

ABSTRACT

Current aircraft use actuators to alter the wing geometry and generate the ideal flight characteristics which is known to be a method of active flow control. By replacing the heavy electric and hydraulic actuators currently used in aircraft wings with lighter and smaller shape memory alloys (SMAs), the mass of an aircraft can be reduced. Therefore, research was conducted to design and build an airfoil using SMAs as the actuator for improving the airfoil's aerodynamic performance. The SMA actuated airfoil was evaluated using advanced flow diagnostic methods and was found to operate with a higher lift coefficient than the non-actuated airfoil for certain angles of attack (AoAs). Testing the SMA airfoil at various frequencies also revealed its effect on the flow recovery after actuation. Lastly, comparison of the SMA to comparable actuators revealed that the SMA wires had a force to mass ratio that was over 100 times larger.

ACKNOWLEDGEMENTS

After 6 year at NDSU, I have had the pleasure of working with and learning from many peers and mentors. This goal in my life would not have been accomplished in the same manner had they not had such a positive impact on my academic career. With that, I would like to thank the following people. My graduate advisor and mentor, Jordi Estevadeordal, who has provided me with valuable academic, professional, and personal guidance when needed. My graduate committee, Yildirim Suzen and Ivan Lima Jr., who sought to challenge me in the pursuit to further my knowledge and understanding. Lastly, the NDSU Mechanical Engineering Department staff and faculty that has provided me with the knowledge to pursue my dream career.

DEDICATION

I would like to dedicate this disquisition to my friends and family. It hasn't been an easy journey to complete this milestone in my life, but the journey with those around me made it all worth it!

TABLE OF CONTENTS

LIST OF TABLES

LIST OF FIGURES

LIST OF ABBREVIATIONS

AoA.....Angle of Attack

SMA.....Shape Memory Alloy

PIV .....Particle Image Velocimetry

FEA .....Finite Element Analysis

LIST OF SYMBOLS

M .....Mach number

Re .....Reynolds number

V_∞ .....Freestream Velocity

a .....Speed of Sound

ρ .....Density

L .....Length

c .....Chord Length

μ .....Dynamic Viscosity

L_F .....Lift Force

D_F .....Drag Force

C_L .....Lift Coefficient

C_D .....Drag Coefficient

ρ_∞ .....Freestream Density

S .....Relative Surface Area

E .....Energy

P .....Power

m .....Mass

L_H .....Latent Heat of Transformation

C .....Specific Heat

T .....Temperature

t .....Time

I .....Current

V .....Voltage

R .....Resistance

ρ_R.....Resistivity

A.....Cross-Sectional Area

LIST OF APPENDIX FIGURES

INTRODUCTION

Background/Motivation

Flow control has become a popular aerodynamic research subject lately, but what many may not know is that the concept of flow control for airfoils was essentially discovered by the Wright brothers. They discovered that by changing an airfoil's camber and angle of attack, the airfoil's lift would be affected. They used this discovery as a method to steer their flyer by changing the airfoil's shape and angle of attack midflight. Surprisingly, their discovery went tens of years without becoming widely noticed as a valuable research topic to improve the performance of current aircraft. Fittingly defining it, flow control is the method of manipulating a fluid flow for a designed purpose of benefiting such things as aircraft, turbines, or vehicles [1]. Flow control with regards to airfoils is achieved by a device or structure implemented on or inside an airfoil to affect the fluid flow around the airfoil, and they can be broken into two categories: passive and active. A flow control device or structure that does not require the input of energy is defined as a passive method. These methods generally include vortex generators or geometric structures on the leading or trailing edges. Research on passive flow control employing leading dimples shows how simple geometry changes can have on airfoils [2]. Due to the limitations of passive methods, active flow control is a much more popular research topic. Active flow control methods are defined as requiring the input of energy to induce a change in the flow. Some active flow control methods involve plasma actuators, synthetic air jets, and morphing airfoils. Based on previous research and advancements in materials, the method of active control was determined to be the focus of this research.

Aerodynamics

When characterizing flow fields for reproducibility in research two dimensionless numbers are generally evaluated. The first dimensionless number is Mach number and is calculated using Equation 1. This value defines the freestream velocity, V_∞, relative to the speed of sound in the medium, a. It also defines the compressibility effect of the flow [3]. If M is below 1, the flow is considered subsonic, and if M is between 1 and 5, the flow is considered supersonic. Due to instabilities and a combination of subsonic and supersonic flow fields around a body, transonic is considered to occur between about 0.8 and 1.2. Besides comparing the flow field velocity to the speed of sound, the Mach number also defines the compressibility of the flow. If M is less than 0.3, the flow can be considered incompressible because the density change is insignificant [3]. This allows low speed research to be easily compared across subject focuses.

$$M = \frac{V_\infty}{a} \tag{1}$$

The second dimensionless number used to evaluate flow fields is Reynolds number which is calculated based on the flows density, ρ, freestream velocity, characteristic length, and dynamic viscosity, μ, which is calculated using Equation 2 below. Re is the comparison of inertial forces to viscous forces of a flow [3]. Assuming the airfoil to be thin, the airfoil can thus be assumed to be similar enough to a flat plate and will have similar critical Re. With the assumption of being similar to a flat plate, the characteristic length can be replaced by the chord length, c. Critical Reynolds numbers define the transition between laminar and turbulent flows with laminar being generally consistent and predictive flows and turbulent being chaotic flow fields. For a flat plate, the transition from laminar to turbulent flows occurs around 500,000 [3]. Comparing Re is just as important as M because different Re can produce significant changes in

the aerodynamic performance of airfoils. An airfoil with an operating Re of 100,000 can have reduced lift and possibly increased drag when compared to the same airfoil scenario with a Reynolds number of 1,000,000.

$$Re = \frac{\rho V_\infty c}{\mu} \tag{2}$$

As previously described, an airfoil's aerodynamic performance can be characterized by several factors such as the lift, drag, pressure, and moment. Lift is the force perpendicular to the freestream velocity whereas drag is the force parallel to the freestream velocity. Both are functions of the pressure and shear stress distribution across the surface of an airfoil. When improving an airfoil's performance, it is generally desired to increase the lift while maintaining or decreasing the drag. To uniformly evaluate the lift and drag for a variety of airfoils and flows, the forces are nondimensionalized into the corresponding coefficient. The lift and drag coefficients are defined in Equations 3-4 [3].

$$C_L = \frac{L_F}{\frac{1}{2}\rho_\infty V_\infty^2 S} \tag{3}$$

$$C_D = \frac{D_F}{\frac{1}{2}\rho_\infty V_\infty^2 S} \tag{4}$$

Airfoil flow control methods are designed to best improve the lift and drag coefficients for a single or variety of expected flight conditions. They improve the aerodynamic performance by mainly reducing or eliminating a specific situation: flow separation. Flow separation occurs when an adverse pressure gradient causes the flow over an airfoil to stop or reverse directions. The pressure/velocity change results in the flow separating from the surface of the airfoil. This separation causes the drag to increase due to the sizeable pressure drag being included and for the lift to exponentially decrease which is referred to as stalling. Stall can be categorized as leading-edge or trailing-edge stall. Leading edge stall is the abrupt occurrence of stall between a

very small AoA change. Trailing-edge stall is the gradual increase in flow separation propagating from the trailing edge. The propagation with respect to AoA allows for the lift coefficient to gradually taper off before decreasing [3].

The last concept to understand when evaluating airfoils is the thin airfoil theory. This is one of the first developed methods to calculate the lift of an airfoil. Based on the thin airfoil theory for a symmetrical airfoil, the lift slope is equal to 2π. For a cambered airfoil, the lift slope is also equal to 2π [3]. The difference between a symmetric and cambered airfoil is the point of zero lift (C_L=0). A symmetric airfoil will always have zero lift at an AoA of 0 degrees while a cambered airfoil can have either a positive or negative AoA with zero lift. Airfoils with increased thickness begin to deviate from the 2π lift slope making the prediction invalid.

PIV (Particle Image Velocimetry)

PIV (Particle Image Velocimetry) is a flow diagnostic method that has been advanced significantly with more accurate particle flow calculations along with 3D volume flow reconstruction. PIV is the velocity reconstruction of flow fields based on images captured of illuminated, seeded flow. The processes of obtaining PIV data first requires a flow to be seeded with appropriate sized particles that reflect light back to the cameras. The seeded flow is then illuminated with a pulsed laser sheet or volume. The laser is synchronized with the camera/s to capture image pairs with a set time step between them. By knowing the image time step, particle pixel shift, and the ratio of pixel to distance, the velocity of the flow can be calculated for each pixel containing illuminated particles. When capturing PIV raw images, it is required to alter the image time step to accommodate the flow velocity. At higher velocities, a lower time shift is required and vice versa for slower velocities. This affects the pixel shift of the particles. The optimal pixel shift is debated in the commercial and research communities. Some believe a pixel

shift of 12 is optimal while others consider 5-10 to be provide the best reconstruction [4, 5]. PIV is capable of reconstructing 2D and 3D flow fields depending upon the setup used. 2D PIV is also referred to Planar PIV, and it only requires 1 camera and a laser sheet to generate x and y coordinate velocity vectors on a single plane. The basic 3D PIV method is Stereo PIV, and it also generates velocity vectors on a single plane. The only difference is that with 2 cameras, the x, y, and z velocity vectors on the plane can be reconstructed. The more advanced and newest 3D PIV method is Tomographic PIV. Tomographic PIV uses a laser volume and generally 4 or more cameras to reconstruct a flow volume with x, y, and z velocity vectors. Tomographic requires more equipment and can be more difficult to process, but it allows users to fully visualize 3D flows which is ideal for unsteady, realistic flow situations.

Smart Materials

Just like flow control, smart materials have gain much popularity in recent years making them cheaper, more energy efficient, and having better material properties. Two common types of smart materials are piezoelectric and SMA materials. Both have very different material behaviors and applications. Piezoelectric materials use voltage to restructure the electric dipoles inside the material to change the normal strain in either the x, y, or z direction depending upon the arrangement of the dipoles and the direction of voltage application [6]. By applying piezoelectric materials to a base material as shown in Figure 1, the entire structure can shorten, lengthen, or bend based on the desired application. Unlike some smart materials, piezoelectric materials can actuate at high frequencies allowing the material to be used as a vibration damper or reversely as a vibration sensor.

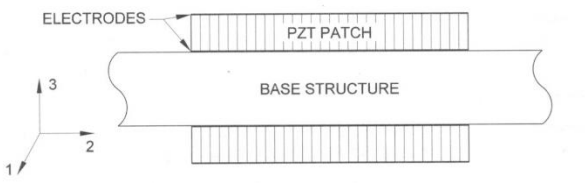

Figure 1. Common Piezoelectric/Base Structure Configuration [6]

SMA materials are another common smart material with material behaviors different than that of piezoelectric materials. SMAs use phase changes to change the materials stress strain relationship. The phase change occurs by heating or cooling the material to a specified critical temperature. Figure 2 shows the transformation between the austenite and martensite phases in order to return to its original shape after a deforming stress is applied. This phase change gives SMAs high recoverable strain percentages compared to other materials. Under the proper loading conditions, SMAs can fully recover up to 8% strain over thousands of cycles [6]. Despite having the ability to recover large strain rates, the major disadvantage to SMAs are their slow response time. SMAs can use Joule heating as a rapid, simple method to heat the material, but the cooling process is generally longer resulting in an overall long period. This period is usually greater than a second, which in some desired applications is impractical. Therefore, the applications of smart materials are very dependent upon the type of material used and its specifically designed structural behavior.

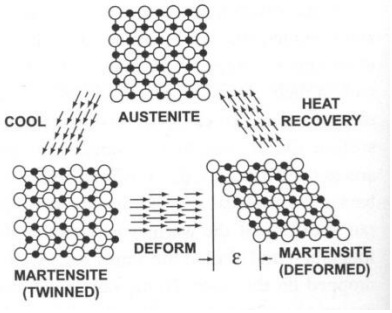

Figure 2. SMA Phase Change Process [6]

Research Goals, Approach, and Thesis Outline

The research documented in the pages to follow had several goals established in its infant stages. The first goal was to design an airfoil utilizing smart materials as the method of active flow control for low speed flight. This was completed by evaluating the advantages and disadvantages of different smart materials and incorporating SMAs into a symmetric airfoil to change its camber. The second goal was to make the active flow control method improve the symmetric airfoil's aerodynamic performance whether it was reducing drag and/or increasing lift. To ensure the variable camber airfoil would have an ideal shape for improved performance, ANSYS FEA (Finite Element Analysis) was utilized to potentially optimize the SMA placement inside the airfoil. Unlike other research involving smart material airfoils, advanced flow diagnostic methods have not been employed to fully evaluate the flow control method; therefore, PIV flow diagnostic methods were incorporated to best understand the flow fields along with XFLR-5 predicted lift and drag coefficients. The last research goal, which was added after the completion of the first goal, was to analyze the effects SMA actuation frequency had on the airfoil's performance. This goal was accomplished by repeating the testing conditions for the second goal with the addition of controlling the actuation period of the SMA wire.

LITERATURE REVIEW

PIV Active Flow Control

PIV has become a popular experimental method to evaluate flow fields due to ability to measure velocity profiles at a high frequency. The capability for PIV to decompose unsteady flows has allowed PIV to become a valuable tool when determining the effectiveness of active flow control methods. Current active flow control based PIV research includes but not limited to three different active flow control methods: controlled compressed air jets, synthetic jets, and plasma actuators. The research generally uses planar or stereoscopic PIV to obtain velocity vector profiles around airfoils or surfaces before a control method is implemented and after it is actuated.

The first flow control method reviewed for the incorporation of PIV techniques is controlled compressed jets. Several studies have been performed using controlled compressed jets incorporated into airfoils. Zhonglun Cai [7] improves upon most compressed jet airfoil designs by incorporating a controlled compressed air jet into the flap of an airfoil designed to mimic high-lift flight configurations used during takeoff and landing. In this specific research, tests were conducted at a freestream velocity of 20 m/s resulting in a turbulent Re of 550,000. Even though Cai's research was tested at a Re about 5 times higher than Re used in this dissertation's research, both values are still significantly lower than 1,000,000 and are considered low speed experiments. Therefore, the research is relatively comparable to the research conducted on the SMA airfoil designed at NDSU. Cai's use of a real world representative airfoil configuration is preferred when looking long term for implementation of the control method, which is something many researchers fail to consider. In this particular instance, the research focus was directed toward reducing separation occurring on the flap since the flap was designed

as an airfoil. The airfoil was deflected at 2^o, and the flap was deflected at 40^o [7]. Since most airfoils are evaluated for separation between 10^o and 20^o, the comparison between the effectiveness of this method to others would generally be difficult, but the use of PIV techniques allows for the flow separation to be visible and delayed along the flap. Besides trying to improve the aerodynamic characteristics for plane wings, Hecklau's [8] research was focused on the improvement of a stator blade. Even though the overall application was different, the flow control method and desired outcome are identical as the previous article reviewed. Hecklau specifically utilized Stereoscopic PIV to measure the 3D velocity vectors at different chord locations [8]. To do so, the system was placed on a translation stage to move the stator blade with respect to the cameras and laser sheet. The PIV results showed that the use of actuated compressed jets forces the flow that was originally separated at about 70% chord length to reattach around 80% chord length [8]. Hecklau was also able to use PIV to clearly visualize the blowing effect on corner vortices. Similarly, Wang researched how unsteady blowing actuation benefits wind turbine blades. They conducted their tests at a Re of 120,000 to resemble low speed conditions and operated the blade at an angle of attack of 20^o [9]. From their study, they were able to use PIV to observe that a separation bubble formed at about 40% of the chord. With determining the location of separation, Wang was able to determine that a blowing slot at 50% chord would best control the separation experienced by the turbine blades around 20^o [9].

The next active flow control method examined was synthetic jets. As Wang described it, "the principle of the synthetic jet is similar to that of unsteady blowing [9]." Instead of controlling the frequency of blowing, synthetic jets alternate between blowing and sucking fluid through an opening at a specified frequency creating an unsteady flow field. Of the research conducted involving PIV and synthetic jets, Gul, like Wang, researched unsteady control

methods to improve turbine blades [9, 10]. However, Gul tested the S809 airfoil blade at a transitional Re of 230,000 and 0 AoA. It was stated that the separation bubble in the laminar boundary layer is located at about 19.6% chord length, but their PIV results only depict the flow field from 51% to 65% chord [10]. Examining the velocity fields provided showed that there is a thin separation layer present despite the airfoil operating at 0 AoA, but without better vector plots, it was hard to fully comprehend the extent of actuator effectiveness. Whereas most researchers use planar and stereoscopic PIV techniques, Tang used tomographic PIV to visualize the effects of synthetic jet actuators [11]. For a NACA 0025 at an AoA of 12^{o}, it was determined from the instantaneous volumetric velocity fields that the actuation of the synthetic jets cause the separation layer fluctuations to change. Essentially, the inclusion of the jets caused the separation periods to increase to the point where separation and attachment occurred the same amount over the 200 images collected [11]. The unsteadiness in the separation layer isn't generally seen in static testing conditions. This may allude to the turbulence intensity of the wind tunnel used to be excessively high compared to most testing conditions that prefer turbulence intensity to be lower than 2%.

The last active flow control method reviewed was plasma actuators which are currently researched for their application in airfoils and surfaces. Unlike the other methods, some researchers consider plasma actuators to be a futile control method due to the increased power and space requirements to operate them. Even though some feel plasma actuators are not suitable for real world applications, they still remain a popular research topic. Of those, Walker used a plasma actuator to control the separation occurring on a NACA 0024 airfoil for a Re of 130,000 [12]. The PIV method employed involved placing the laser behind the airfoil resulting in areas missed by the laser sheet. Therefore, velocity vectors weren't obtained close to the

airfoil's bottom surface at AoAs greater than 8^{o} [12]. Most research avoids this placement so as to acquire complete vector profiles on at least one surface side of an airfoil along with profiles in front of the leading edge. Despite the loss of the flow profile, the use of the plasma actuator was able to reattach the flow for the airfoil at 16^{o}. Using the calculated velocity magnitudes, they were able to calculate the plasma actuator effectiveness for various AoAs and Re. They determined that the effectiveness consistently reduces when the Re increases, but it doesn't always lower when the AoA increases for the tested actuation voltage [12]. In addition, Francioso used a combination of pressure sensors, PIV, and plasma actuators to monitor and control the flow separation occurring on a curved wall placed inside a wind tunnel [13]. Using PIV techniques with a smoke generator as the seeding method, Francioso was able to calculate the velocity vectors over the curved wall with and without the plasma actuation. The PIV results along with the pressure sensor data were able to better understand the location and extent of the flow separation in this case [13]. Finally, Kotsonis studied the influence plasma actuators have on a rounded trailing edge airfoil in flows with Re of 140,000, 210,000, and 280,000 [14]. Unlike most of the other experiments conducted, this had a slightly larger aspect ratio of 2.5. The PIV results were able to determine the impact of plasma actuation on rounded trailing edge airfoils for different AoAs [14]. Plasma actuator research may be considered moot, but with the use of PIV, they have proven to be successful in preventing and reducing flow separation.

Despite the application, method, or specific PIV technique used to evaluate the flow field, the results in all the previously reviewed articles were the same. The active flow control method was able to either able to temporarily or permanently reattach the flow or reduced the significance of the separation. The PIV techniques utilized clearly quantitatively determined the extent of the flow separation occurring in each scenario.

SMA based Smart Airfoils

Based on current research, SMAs can be used as an actuation method to alter an airfoils geometry for the purpose of improving its aerodynamic performance. The SMA related literature reviewed below was divided into six different sets based on the method evaluated for altering the airfoils geometry with the intention of improving its efficiency: actuated flaps, combined SMA and Piezoelectric Flaps, multi-segment actuated flaps, trailing edge based camber changes, general camber changes, and dihedral and sweep changes. Each of these sections research different ways to improve an airfoils performance whether it is increasing lift, reducing drag, and/or reducing weight. The various methods of wing deformations evaluated in the articles are illustrated in Figure 3 below.

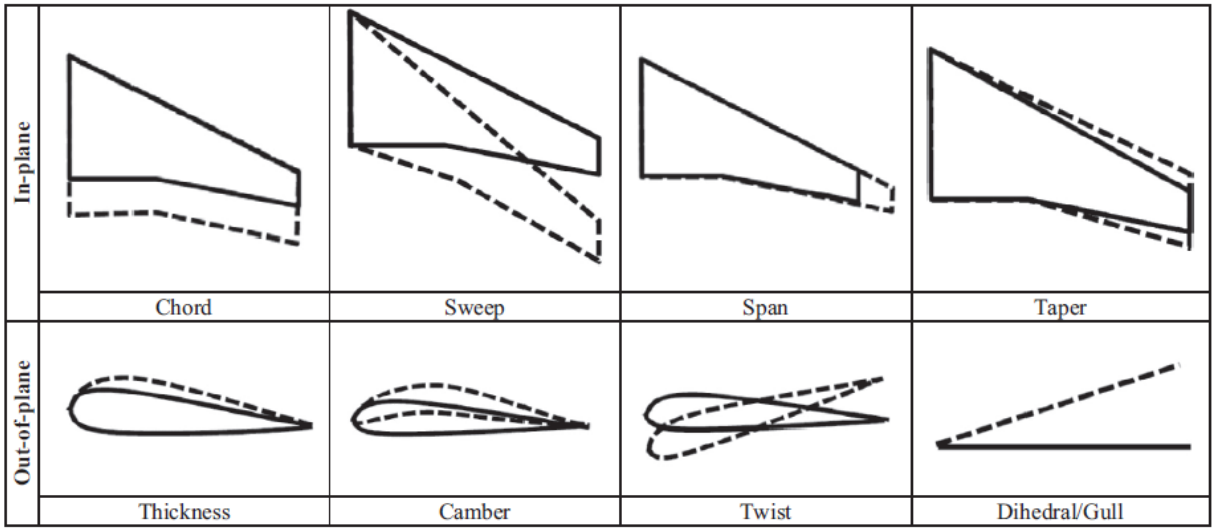

Figure 3. Various Methods of Wing Deformation [15]

Actuated Flaps

The first compiled literature section reviewed was the introduction of SMA's to actuate flaps on the trailing edge of an airfoil. Actuated flaps have been incorporated into all commercial, private, and military aircraft since the beginning of human air vehicle flight. Flaps are generally used to alter an air vehicle's pitch or roll while in flight. In Senthilkumar's

"Analysis of SMA Actuated Plain Flap Wing," a flap wing airfoil utilizing the NACA0012 airfoil geometry was fixed with several SMA wires and a spring to control the actuation of the trailing edge flap [16]. Respectively, the chord length and span of the airfoil was 220mm and 210 mm. The testing of the airfoil was conducted with a freestream velocity of 15 m/s and the purpose of the testing was to correlate applied current to flap angle and flap angle to CL. Unlike most of the articles that will be reviewed, this paper investigated the correlation between applied current and SMA performance. From a reader's point of view, the research performed by Senthilkumar was a way to accommodate existing wing designs. However, it does not address the frequency at which the SMA wire can be actuated at different applied currents. Without this information, the likelihood of the concept being applied to current aircraft is highly improbable.

Like Senthilkumar, Hanagud researched an actuated NACA 0012 airfoil using SMA wires [16, 17]. Their goal was to create an adaptive rotor blade on a remote control helicopter in order to generate a larger lift coefficient. Due to the application of their research, the full span of the airfoil was not actuated. Only 8" of the 28" blade span was actuated, and 1"out of the 2.5" chord length was actuated [17]. Even though this article only addressed the approach as a proof of concept, it was able to demonstrate the effectiveness of using an SMA actuated flap to improve the generated lift of an airfoil.

The last article reviewed regarding actuated flaps was slightly different than the two previous articles. In "Morphing Wing Mechanism Using an SMA Wire Actuator," a smooth transitioned flap was created [18]. The previous flaps researched did not have a smooth surface transition when the flap was actuated. This resulted in gaps in the airfoils surface geometry which can lead to increased drag and reduce the maximum lift coefficient the concept can generate. A Clark Y airfoil geometry was used with a chord length of 275 mm. Using an

internal frame structure along with SMA wires and a polyvinyl chloride skin, the continuous airfoil could deflect its flap up to 21° when current was applied. The maximum frequency that could be achieved for 21° was .1 Hz [18]. The results of the continuous flapped airfoil showed that the C_L/C_D ratio was larger than the unactuated airfoil geometry with a freestream velocity of 20 m/s [18]. Despite the testing was only conducted in a computational fluid dynamics solver, the detail provided in the article did not give concerns for the experimental results varying significantly.

Overall, using SMAs to actuate flaps can be a useful method to eliminate weight from existing aircraft but may not play a large role in future aircraft. Based on the extensive use of current actuators in aircraft, SMA's most likely won't replace them. The upside to researching flaps using SMAs is that this helps open up the door for future advanced applications in the field of aerospace and aeronautics.

SMA-Piezoelectric Flaps

Similar to the previous section of articles that researched an SMA actuated flap, "Synergistic Smart Morphing Aileron" uses SMA wire to control a leading edge flap [19]. However, the article explored the effects of actuating a trailing edge flap that is constructed of a piezoelectric composite. The airfoil geometry used in the research is a NACA 0012, but only the trailing edge was constructed. The article evaluated the amplitude of deflection achieved based on frequency by using square wave input signals to control the SMA hinge and the piezoelectric flap [19]. As expected, the SMA actuated at a higher amplitude but with a lower frequency (0.1 Hz) whereas the piezoelectric flap operated at higher frequencies (6Hz) before losing significant amplitude. When using both materials in unison, the flap was able to outperform either material at lower frequencies and began to mimic the piezoelectric results at higher frequencies [19].

This article shows the advantages of each material, and it is clear that not just one material can meet the demands of aerospace applications when just used on a conventional flap design. For future research, combining different smart materials to help compensate for each other's weakness may be the be answer to improving an airfoil's performance,

Multi-Segmented Flaps

In Karagiannis' article [20], a multi-segmented airfoil is constructed using SMA wires to actuate each hinged section. This construction only had three segments (2 SMA hinged locations) to create deflection of the trailing edge. The design was also analyzed with a FE model using a chord length of 620 mm and a span of 800 mm. The most common form of actuating SMA wire is through Joule heating; however, Karagiannis heated the wire by wrapping it in a kapton insulated electrical wire. This wire was then heated and the SMA wire was heated through conduction [20]. This may be a better method that direct joule heating since it had the potential for more uniform heating of the SMA wire. Unloaded, the segmented trailing edge was able to deflect up to about 50 mm at the trailing tip. When loaded with 8 kg spread over the last two sections, the tip was able to deflect up to 65 mm. Ideally, the testing performed would have a correlation between their actuated wing and lift and drag coefficients, but the paper was only set to "bridge the gap between theory and practice for aeronautical applications of SMA materials [20]."

In "Morphing Trailing Edges with Shape Memory Alloy Rods" and "A Novel SMA-based Concept for Airfoil Structural Morphing," the same approach to creating a rib based multi-segmented trailing edge was considered [21, 22]. The first article merely looked at the plausibility at constructing a rib structure for a segmented trailing edge along with analyzing the SMA material characteristics to determine the deflection exhibited for a specific design [21].

The later of the two articles analyzed the parameters required to proportionately build an optimized airfoil including the elastic hinge along with its required angles and diameter and different SMA actuator designs. The proposed conceptual design consisted of 5 sections with 4 elastic/SMA wire hinges. According to numerical simulations, max deflections of the segments were 246.7 mm without aerodynamic loads and 223.9 mm with loads [22].

In Barbarino's recent article, "Airfoil Structural Morphing Based on S.M.A. Actuator Series: Numerical and Experimental Studies," an actuated multi-segmented trailing edge is fully constructed [23]. Despite having most of the same researchers on this article as the previously stated one, the proposed concept was different. This design used titanium arches to act as a spring mechanism that was actuated by SMA ribbons [23]. A full-scale 3D flap bay was constructed based on standard aircraft. The actuated flap bay had a maximum thickness of 0.25m and was 0.8 m long to correlate to a 30% chord length. To create the desired deflection, 4 titanium arches were able to deflect the tip 185 mm without loads and 131 mm with aerodynamic loads. After 15 seconds of actuation, over 6500 Joules were applied, and full actuation was achieved in 37 s. After several cycles, Barbarino found that the deflection was only 123 mm. Due to their loading, the SMA started experiencing fatigue. The insulating bushings used between SMA ribbons also experienced warping [23]. Overall, this was the largest design approach in the reviewed articles, but there were still several areas that needed to be designed better to eliminate fatigue and possible future failure.

All of the multi-segmented methods proposed probably have the highest probability of being applied to the field of aerospace. This is mostly due to the fact that they can easily be scaled large enough to work on medium sized subsonic aircraft. However, after reading the articles, there were still issues with the designs that need to be addressed. Material fatigue was

the main concern. Gathered from the articles, most of the designs were trying to utilize the highest amount of strain and force the SMAs could generate. When life expectancy is an important factor, the maximum stress and strain a material can survive is greatly reduced. To ensure that the designs would have a chance at meeting FAA regulations, the designs would need to better handle the fatigue experienced by the SMA wires and ribbons. This could be accomplished by adding more SMA material, reducing the applied load per cycle, or reducing the amount of strain created per cycle.

Trailing Edge Based Camber Changes

Creating a trailing edge camber change can be characterized as many different actuation methods. Essentially, all the previous sections are trailing edge camber changes, but the description used in this section refers to creating a trailing edge camber change without the dislocation of the airfoil surface as seen in non-continuous flaps. The first article, "A Combined Smart-materials Approach for Next-generation Airfoils," reviewed altered a NACA 4412 geometry with a span of 200 mm and chord length of 425 mm [24]. SMA and piezoelectric actuators were used to deform the trailing edge starting about 200 mm after the leading edge. Using strain gauges, it was found that the airfoil could achieve about 20 mm of deflection in either camber direction. Including the total top actuation to bottom actuation, the wing design was able to achieve its goals of about 10% deflection in reference to the chord length. It also was able to achieve 1 mm deflection at a frequency less than 100 Hz when utilizing the piezoelectric composites imbedded in the airfoil surface [24].

Abdullah [25] employed a simple method of deflecting the trailing edge of a Clark Y airfoil with a span and chord length of 175 mm and 247 mm. He attached SMA wires from the leading edge to the lower camber about a third of the chord length from the front. The model

was fixed at this location causing the trailing edge to be deformed by the SMA wires. Using a flexible ABS skin, the result is a large trailing edge deflection and minimal leading edge change. Wind tunnel testing was performed at four different Reynold's numbers. For all the Reynold's numbers, the morphed airfoil had a better C_L/C_D when the C_L was lower than about 0.85. Preferably, they would have also correlated the C_L/C_D to angle of attack for the original and morphed airfoil to understand the effects to stalling angle of attack [25].

The focus of Kancharala's report [26] was to experimentally build SMA actuated airfoils that induced a deflection in the trailing edge. He used two different methods to create such a deflection. The first method was identical to Abdullah's where SMA wires were attached from the leading edge to a location further along the chord of the airfoil. Kancharala was able to receive similar results with using aluminum skin instead of ABS [25, 26]. His second method utilized a sliding mechanism on the lower camber to allow for the surface to easily transverse when a SMA wire, attached to the airfoils' bottom surface, contracted. The sliding mechanism allowed both meeting ends of the discontinuous surface to move and allowed for easier deflection of the airfoil while minimizing the effects of a discontinued surface. Kancharala did not present any testing data on the specifics of how the lift or drag coefficients were affected; however, he did state that the sliding mechanism created a deflection of about 17 mm whereas the continuous method with aluminum skin only deflected 2.5 mm [26].

In Sinn's thesis [27], he used the simple method of applying a tensile force to the end of a cantilevered beam to create deflection in which he later applied to an airfoil. By placing the cantilevered beam inside the airfoil along the camber line, he was able to deflect the airfoil in a similar fashion as if the airfoil was not present. Sinn performed extensive testing on the SMA wire, composite cantilevered beam, and the airfoil to understand the deformations. By using

strain gauges attached to the airfoils cantilever beams, he was able to get real-time data from the system as current was applied. He also performed CFD simulations and wind tunnels tests on the airfoil to receive the lift coefficients based on angle of attack and trailing edge rotational angle [27].

Lastly, Strelec used the same method as Abdullah and Kancharala by attaching SMA wires between the leading edge and the bottom airfoil surface [25, 26, 28]. Strelec took it one step further by placing another set of wires connecting the bottom airfoil surface to the trailing edge. By doing so, he was able to decrease the camber of the airfoil along with deflecting the trailing edge while using an ABS skin. After extensive testing and numerical simulations, it was found that the deformed airfoil did create higher lift coefficients up to at least an angle of attack of 10°. The increase wasn't large but varied from about 6 to 8% [28]. Between all the trailing edge deflection articles discussed, they all seem to produce similar results using either aluminum or ABS skin. The results make it seem that these concepts may be ready for larger scale testing like testing performed on the multi-segmented flaps.

Camber Alterations

Unlike the proposed methods described in the previous section where the camber was altered as a result of deforming the trailing edge, "Aerodynamic Performance Optimization of Smart Wing Using SMA Actuator" only alters the general camber of the airfoil [29]. Using an SMA actuator that acts like a lever, the upper camber of a NACA0021 airfoil was increased when the wire was heated. The wing had a span of 25 cm and a chord length of 16 cm. The camber was increased at 25% of the chord length from the leading edge. When the experimental, numerical, and analytical results were compared, the morphed airfoil generated larger lift coefficients from 0 to 25° angle of attack. All three evaluation methods also provided near

identical results [29]. The only irregularity in the results lied in the analytical analysis. After about 15° angle of attack, the article did not specify how the results were calculated. Therefore, the certainty of the data is questionable. This simple design may be useful in specific applications, but currently it is hard to see it being fully utilized based on the previous methods that can achieve more with the same amount of effort.

Dihedral and Sweep Alterations

The article "Experimental Study of a Bio-inspired Robotic Morphing Wing Mechanism Actuated by Shape Memory Alloy Wires" used SMAs to significantly alter an airfoils geometry in the X and Z axes which was a completely different approach than any of the other papers reviewed [15]. Using two sets of SMA wires and springs, the airfoil design could deflect in either direction independently. Between both directions, the maximum deflection angle achieved is about 19°; therefore, Basaeri and his colleagues designed the system with the intention of connecting several in series to produce the desired angle rotation of the airfoil [15]. For clarity on the direction in which the deformation is occurring, Figure 4 depicts the expected dihedral and sweep alterations to the airfoil with several sections attached together. As the last article reviewed, this definitely presented a completely different concept to improving an airfoil's flight performance. Even though this article was tailored more toward insects and miniature scale aircraft (RC plane scale), if designed properly, it may have the potential to make its way into small sized aircraft (2-seater aircraft) in the future.

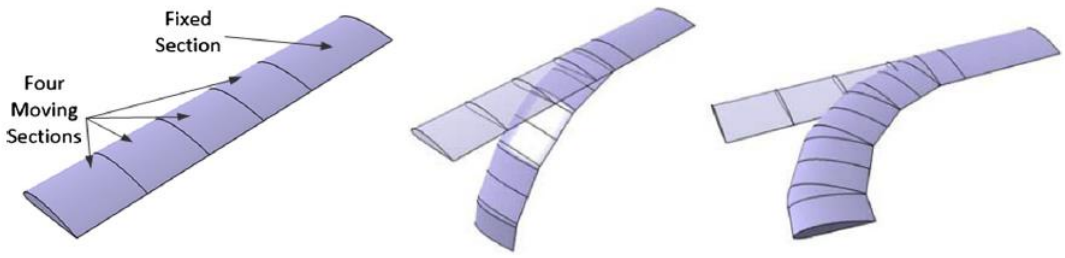

Figure 4. Original, Dihedral, and Sweep Airfoil Shapes [15]

AIRFOIL DESIGN

Smart Material Selection

To allow the airfoil to deform without the use of conventional actuators, a nickel-titanium SMA also known as nitinol was chosen to provide the actuation force. Nitinol was chosen over other SMAs and piezoelectric materials for several reasons. The first reason nitinol was chosen was due to the amount of deflection it would generate. Piezoelectric materials can only cause their attached beam to bend with a limited radius, and with the appropriate internal design, nitinol would be easily be able to generate more deflection. Another reason nitinol was chosen over a piezoelectric material was that it required less power to operate. The third reason nitinol was chosen was that it requires very little space for all the required equipment. Since nitinol requires less power than piezoelectric materials, the power supply could be a battery with sufficient output amperage. For larger scale models where everything would be required to be housed in the aircraft, it would make sense to choose the option that required less space and thus adding less mass to the aircraft. The main draw back to nitinol over piezoelectric materials was the actuation frequency. At its quickest, it requires approximately 1 second to fully contract and another 2 seconds to return to its original length. However, if the deformed airfoil was capable of outperforming the original geometry, then the deformed geometry may be able to be continually generated instead of cycled between the two geometries. When comparing various SMAs, Nitinol was utilized due to the relatively inexpensive cost and that it seems to have more favorable mechanical properties than copper and other metal based SMAs [30]

For the airfoil, the nitinol used to generate the actuation force was purchased from the manufacturer DYNALLOY, Inc. which provides various diameter and activation temperature actuator wires. Figure 5 shows the available wire sizes with information regarding the

corresponding resistance, recommended current application, applicable force, and cooling times. The company also provides various physical properties of the alloy as provided in Table 1.

Diameter Size inches (mm)	Resistance ohms/inch (ohms/meter)	Pull Force* pounds (grams)	Cooling Deformation Force* pounds (grams)	Approximate** Current for 1 Second Contraction (mA)	Cooling Time 158°F, 70°C "LT" Wire *** (seconds)	Cooling Time 194°F, 90°C "HT" Wire *** (seconds)
0.001 (0.025)	36.2 (1425)	0.02 (8.9)	0.008 (3.6)	45	0.18	0.15
0.0015 (0.038)	22.6 (890)	0.04 (20)	0.016 (8)	55	0.24	0.20
0.002 (0.050)	12.7 (500)	0.08 (36)	0.032 (14)	85	0.4	0.3
0.003 (0.076)	5.9 (232)	0.18 (80)	0.07 (32)	150	0.8	0.7
0.004 (0.10)	3.2 (126)	0.31 (143)	0.12 (57)	200	1.1	0.9
0.005, (0.13)	1.9 (75)	0.49 (223)	0.20 (89)	320	1.6	1.4
0.006 (0.15)	1.4 (55)	0.71 (321)	0.28 (128)	410	2.0	1.7
0.008 (0.20)	0.74 (29)	1.26 (570)	0.50 (228)	660	3.2	2.7
0.010 (0.25)	0.47 (18.5)	1.96 (891)	0.78 (356)	1050	5.4	4.5
0.012 (0.31)	0.31 (12.2)	2.83 (1280)	1.13 (512)	1500	8.1	6.8
0.015 (0.38)	0.21 (8.3)	4.42 (2004)	1.77 (802)	2250	10.5	8.8
0.020 (0.51)	0.11 (4.3)	7.85 (3560)	3.14 (1424)	4000	16.8	14.0

Figure 5. Available Nitinol Wire and Performance Properties [31]

Table 1. DYNALLOY Nitinol Material Properties [31]

Density (ρ)	6.45 g/cm^3
Specific Heat (C)	0.83736 J/(g*K)
Latent Heat of Transformation (L_H)	24.1904 J/g
Martensite Electrical Resistivity (ρ_R)	80 μΩ*cm
Austenite Electrical Resistivity (ρ_R)	100 μΩ*cm

In order to actuate the wires, the Joule heating method was employed. The amount of power required to actuate the wires in 1 second was determined utilizing Equation 5 which calculates the required energy and Equation 6 which calculates the required power. In Equations 5 and 6, m is the mass of the wire, L_H is the latent heat of transformation of nitinol, C is the specific heat of nitinol, ΔT is the difference between the activation and ambient temperatures, and t is time. With the required actuation power calculated, Equations 7 and 8 can be utilized to determine the required amperage for actuation. The required current (I) in Equation 7 can be solved by calculating the wire resistance (R) based on the resistivity of nitinol (ρ_R), wire length (L), and wire cross-sectional area (A). Calculating the resistance and required current from the provided properties results in the current and resistance matching the values provided by DYNALLOY. Therefore, the data provided by DYNALLOY, Inc. was used to design the electrical system of the airfoil.

$$E = mL_H + mC\Delta T \tag{5}$$

$$P = \frac{E}{t} \tag{6}$$

$$P = VI = I^2R \tag{7}$$

$$R = \frac{\rho_R L}{A} \tag{8}$$

Desired Airfoil Shape

One of the most critical pieces to ensure the airfoil's performance would be improved through actuation was understanding and creating the appropriate deformed airfoil shape. Initial concept testing proved that the last 1/3 of the chord could be easily deformed with the actuation of nitinol. By fixing the length of nitinol that was used to actuate the airfoil and assuming a strain change of 4%, the only variable that affected the airfoil's deformed shape was the wire placement on the lower surface. 4% stain was used because the manufacture states that

designing for 4% strain allows for longer life cycle to minimize fatigue. ANSYS finite element analysis methods were used to evaluate the wire location at 10, 20, 30, and 40 mm from the beginning of the deformable chord length which was 50 mm in length. To accurately analyze the deflections generated by ANSYS, the symmetric airfoil's trailing geometry was imported into the software. Through measurements and angle calculations, wires were attached at the corresponding chord length and the same start point upstream of the trailing connections. Since only the deformable section of the airfoil was included in the simulations, boundary conditions had to be defined. At the locations where the deformable area connected with the fixed airfoil surface, the surface was not allowed to translate or rotate which corresponded to a fixed boundary. Do to complexity issues, the wire connections to the deformable area had to be allowed to rotate but not allow for removal from the surface. Therefore, the boundary condition used was No Separation. Lastly, the actuation force was modeled using a distance displacement since that was easily calculated from the strain percentage and original nitinol length. To correctly use a distance displacement, the direction had to be parallel with the wires original direction. To ensure the wire wouldn't reduce the amount of displacement transmitted to the airfoil surface, the modulus of elasticity of the wire was vastly increased beyond the material's original modulus. The FEA simulation determined that placing wires at the 20 mm location would possibly provide the best performance when deformed. The 20 mm location would be promising based on a few factors. The first factor being that it limited the vertical deformation of the trailing edge. This location deformed the trailing edge by 2 mm while the others were between 2 and 4 mm. The second factor was the large radius of curvature of the deformed region. Having a large radius of curvature would possible limit the amount of separation seen in the airfoil's wake. Figure 6 depicts the process of actuation with wire placement at 20 mm from

66.67% chord. The remaining FEA results are located in the Appendix. As the simulation confirmed, the change from the symmetric geometry to the deformed geometry in this specific airfoil design does change the airfoil three dimensionally. However, the deflections generated in the span direction are so miniscule that they can be ignored for calculations, behavioral assumptions, and flow field effects.

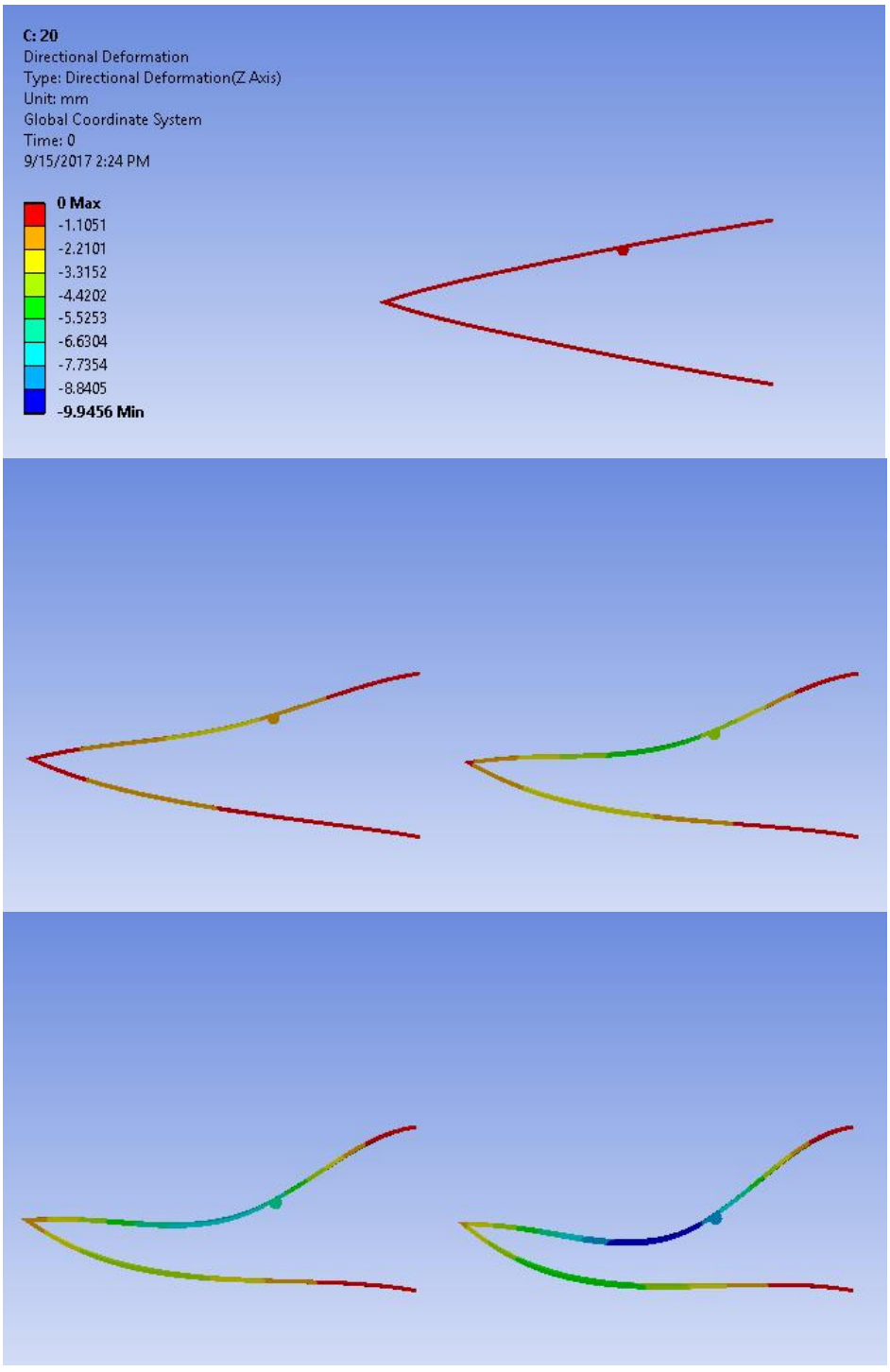

Figure 6. Deformation Steps for Wire Location 30 mm from Trailing Edge

Internal Airfoil Design

The airfoil designed to transform from a symmetric NACA 0021 geometry to a cambered geometry utilized nitinol actuation wires inside to generate deflection near the trailing edge. To accomplish this, the airfoil's design required a combination of a rigid and flexible structure to deform only in the desired locations and an electrical system to activate the deformation. The structure was constructed of an internal rigid structure made from ¼" plywood that was laser cut to the precise geometry of a NACA 0021 airfoil. The airfoil shapes were adhered with spacing dowels to create 7 internal compartments. The number of compartments was determined to allow space inside the airfoil for the nitinol wire while ensuring the surface material placed over the structure would not deform inward during testing. To ensure the airfoil's deflection could be assumed as 2-D deflection, nitinol wires were placed in 4 of the 7 sections. From initial testing, it was discovered that a single wire in each section would suffice to deform the airfoil during testing. During initial testing, it was also discovered that overheating of the wire was a problem that could easily occur which would result in the failure of the wire. To mitigate the overheating, two wires were placed instead of one to reduce the chance of wire failure. The wires' pulling force was maximized by fixing both ends towards the leading edge and looping the wires at point near the trailing edge. This method allows the wires to actuate the 4% while doubling the pull force in each actuated compartment. To create a smooth surface for the airfoil, the leading edge was covered in a thin aluminum sheet to provide rigidity, while the last third of the chord was covered in a polyester sheet for flexibility. Figures 7 and 8 show the basic structure and wire placement of the designed airfoil.

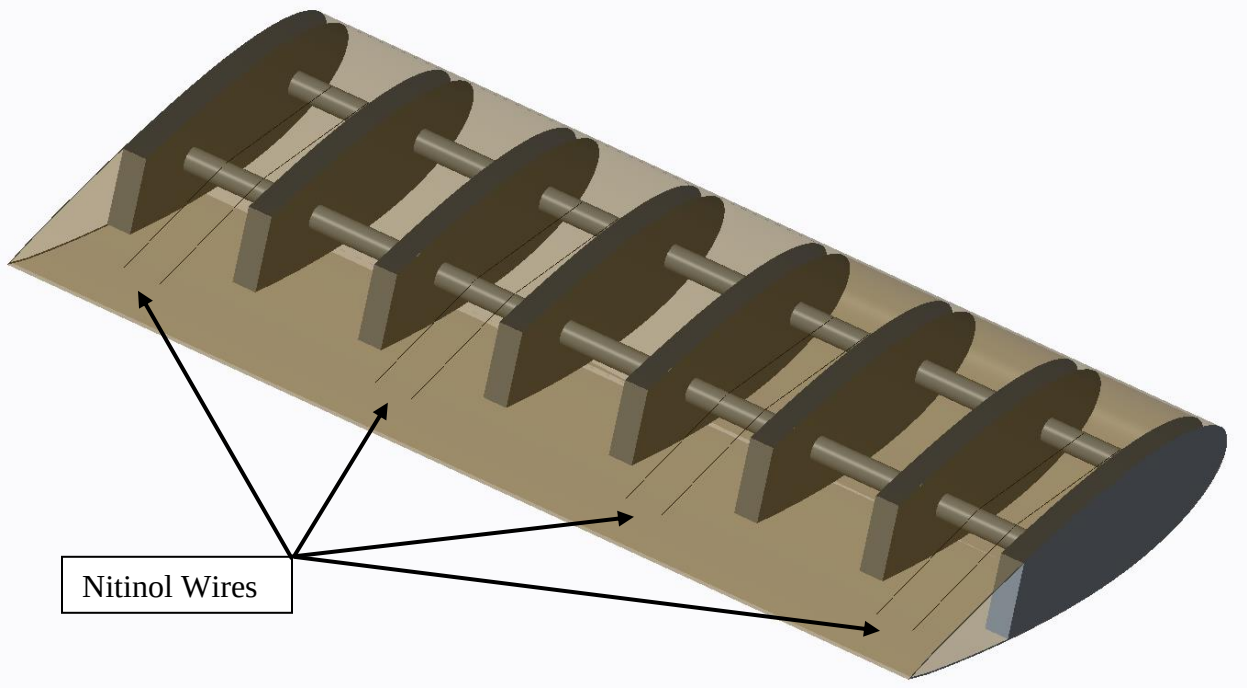

Figure 7. Experimental Airfoil Internal Structure

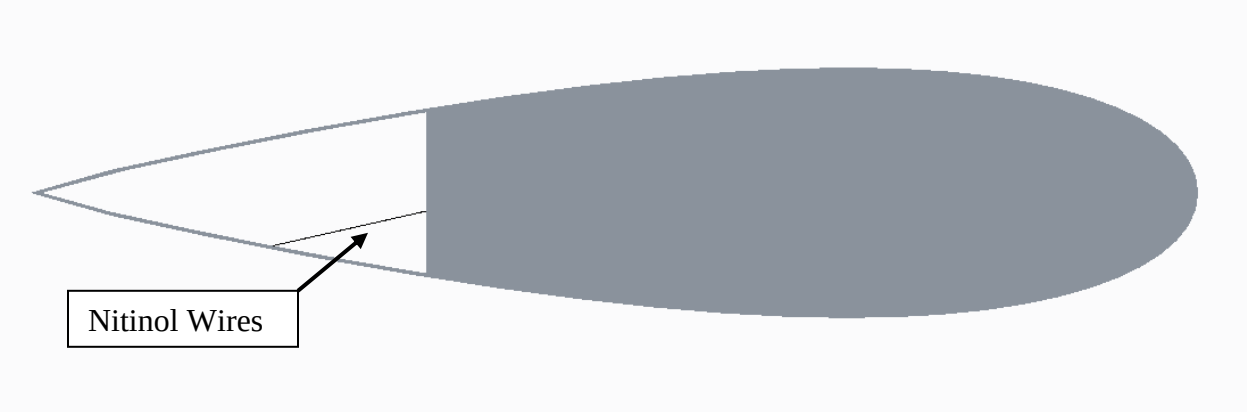

Figure 8. Side View of the Nitinol Placement on the Polyester surface

The second component of the airfoil's design was the electrical system. The electrical system required a current based power supply and a switch to actuate the nitinol wires which acted as resistors. Figure 9 illustrates the layout of the electrical system used to control the airfoil. Each resistor represents a wire segment thus making two wires in each of the four compartments. The power supply was capable of outputting a specific current or voltage, but for this specific application, the supply was set to a fixed current of 0.82 A. The switch used was a

relay switch controlled by an Arduino microcontroller. The microcontroller was connected through a USB connection to a computer and programmed using MATLAB. Several scripts were created to control the actuation frequency of the wire. For initial testing of the two geometries before actuation frequency was studied, the microcontroller merely activated the wires for an uninterrupted time period before opening the circuit to return the geometry to the symmetric NACA 0021.

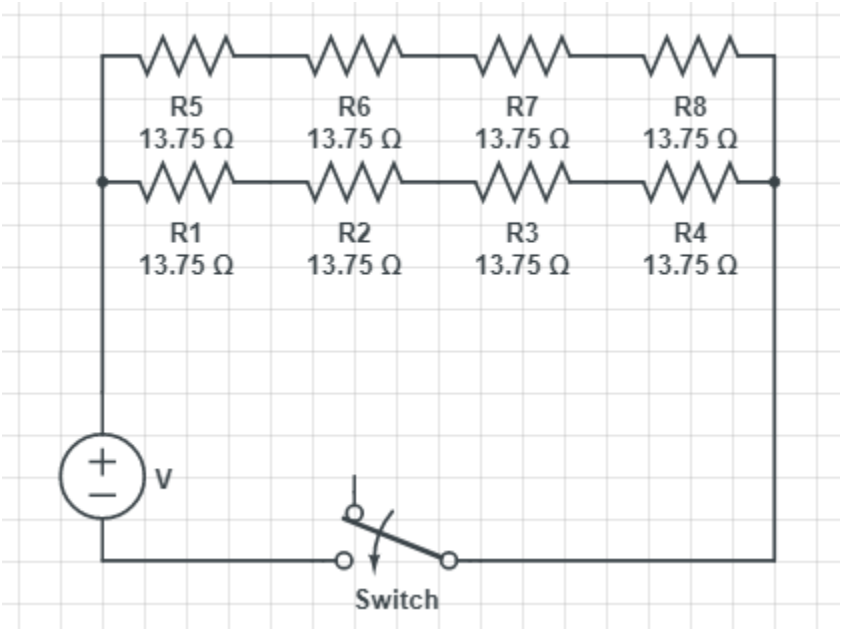

Figure 9. Electrical Diagram of the Airfoil

Overall, the integration of the two components of the airfoil were able to alter the airfoils original geometry and allow it to return to that original state. The experimental airfoil's deformed geometry can be seen in Figure 10 below which was constructed from two camera images.

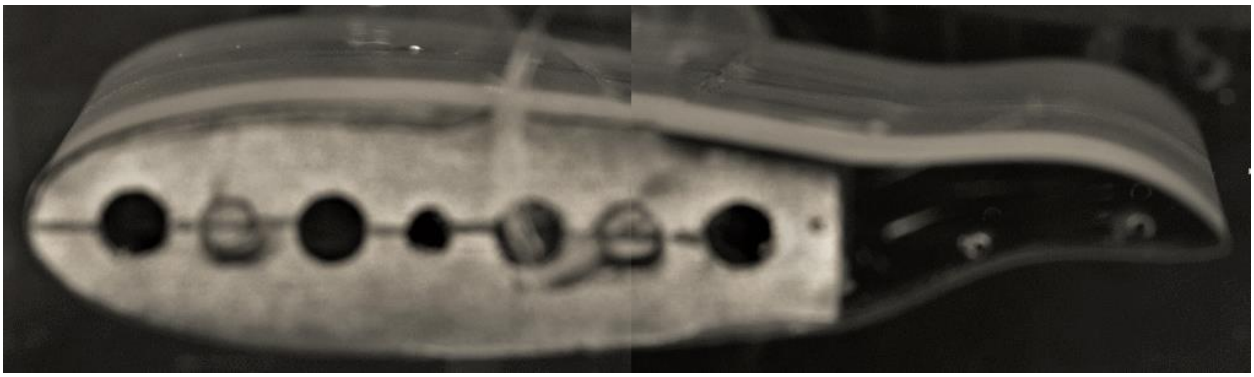

Figure 10. Experimental Deformed Airfoil

EXPERIMENTAL SETUP AND PROCESSING

The experimental airfoil was tested in a low speed open-circuit wind tunnel with approximately a 0.3 m * 0.3 m cross sectional test section. Both configurations of the airfoil were tested under the same wind speed conditions of 10 m/s. This freestream velocity at room temperature conditions equates to a Reynold's number of ~100,000. At this speed, the calculated turbulence intensity of the wind tunnel was 5-6%. To properly evaluate the two airfoil geometries, they were tested at an AoA of 0, 10, 12.5, and 15 degrees. This specific set of AoAs allows for the differences between the symmetric and cambered configurations to be examined at a baseline angle and near stall angles. After recording data for the two geometries, the actuation frequency was also studied. In this set of experiments, the actuation frequency was set to 0.33, 0.167, and 0.11 Hz.

XFLR-5 was used to generate lift and drag coefficients for both geometries for an assumed infinite span. Parameters inside XFLR-5 were respectively set with the following Ncrit, M, and Re: 5.0, 0.0, and 150,000. Due to complications with the deformed geometry solutions, a Reynolds number of 150,000 was used instead of 100,000. When running XFLR-5 at Re=100,000, the lift and drag coefficients were only generated from 8 to 15 degrees. With such a small range to compare and the exclusion of the linear slope region, it was required to make the XFLR-5 Re=150,000 in order to more fully generate lift and drag curves. This increase in Reynolds number did affect the lift and drag coefficients for the AoA range investigated, but the coefficient differences between the two Reynolds numbers was miniscule enough that the Reynolds number effect was ignored. The complications to produce lift and drag coefficients for a wide range of AoAs also led to lack of the 0 lift AoA for the cambered geometry. To generate the solutions, the 2-D geometries were created in the software. The symmetric NACA 0021

geometry was already loaded into the software, but the deformed geometry had to be created by importing an image of the deformed configuration, creating a spline over the top of the image, continually refining the spline data points for a smooth surface profile, normalizing the airfoil's length, and rotating the spline to orientate it to the correct 0 AoA.

The airfoil was installed in the middle of the test section to minimize wall effects on the flow fields near the airfoil. Illumination was provided by a double-pulsed Nd:YAG laser (NewWave MiniLase-III) that emits two laser pulses of up to 100 mJ at a wavelength of 532 nm. The laser beam was diverted through two prisms and a mirror to direct it into the wind tunnel. The beam was shaped to a thin laser sheet (thickness <1 mm) by using spherical and cylindrical lenses. To visualize the illuminated flow, it was seeded with submicron 'DEHS' droplets produced from Laskin nozzles to acquire high fidelity data. Two LaVision Imager LX GigE Model cameras with 1608 x 1208 pixels were used to capture the flow structures. The cameras and the Nd:YAG laser were connected to a workstation with a programmable timing unit (ISSI PDG-2) and a pulse generator which controls the timing of the laser illumination and the image acquisition. LaVision DaVis software was used for control of the parameters. The experimental time delay between the camera frames was set to 100 μs to deliver adequate pixel displacements of the seeded flow for the experimental freestream velocity. With everything connected, the entire system was operated at combined max frequency of 10 Hz. The PIV setup can be summarized with Figure 11 seen below.

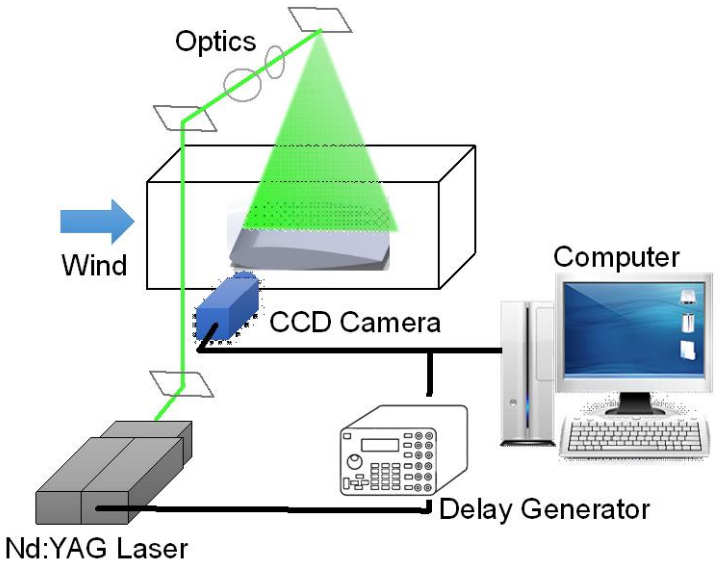

Figure 11. Diagram of Standard PIV System [2]

With the raw images collected, such as those seen in Figures 12 and 13, for the two geometries and various actuation frequencies, the data was processed using LaVision's DaVis software. The "PIV (particle image velocimetry)" operation was used to properly correlate the camera calibration with the raw images to construct the velocity fields. Areas not illuminated by the laser sheet such as the bottom surface of the airfoil were masked out using a geometric mask. The vector calculations used a sequential cross-correlation process with multiple passes reducing the window size from 96 x 96 to 24 x 24 over the 6 passes utilizing an overlap of 50%. Lastly, vector postprocessing was utilized to remove outliers in the flow fields and insert vectors based on surrounding results. With the raw images processed, the time-averaged results were obtained by averaging several flow fields of the same configuration. For the baseline geometry experiments, the time-averaged flow fields consisted of 100 images. The time-averaged results for the actuation frequency experiments ranged from 10 to almost 100 images depending upon the geometry and the actuation frequency. The time averaged and instantaneous PIV results were all acquired during consistant geometry conditions. This means that the data was averaged or

used individually either before any actuation changed the airfoil geometry, the actuation geometry was fully deformed and at a fixed shape, or after the actaution was removed and the airfoil had fully returned to its original geometry.

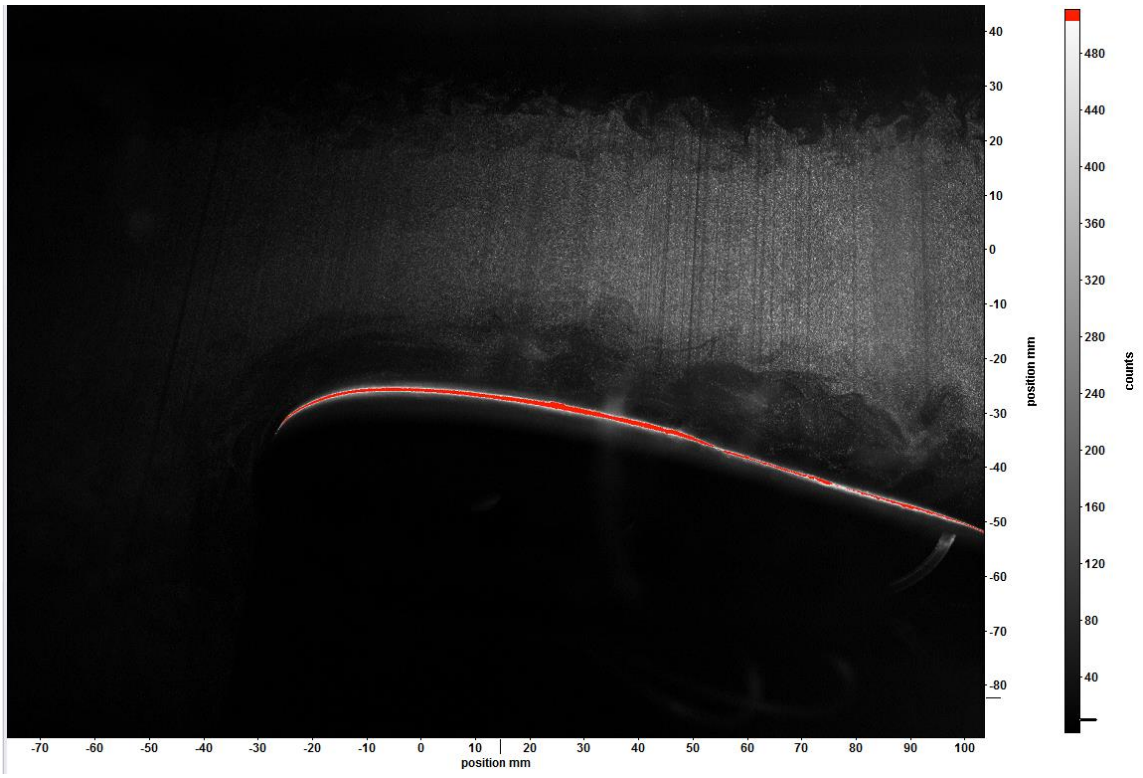

Figure 12. Leading Camera Raw PIV Image

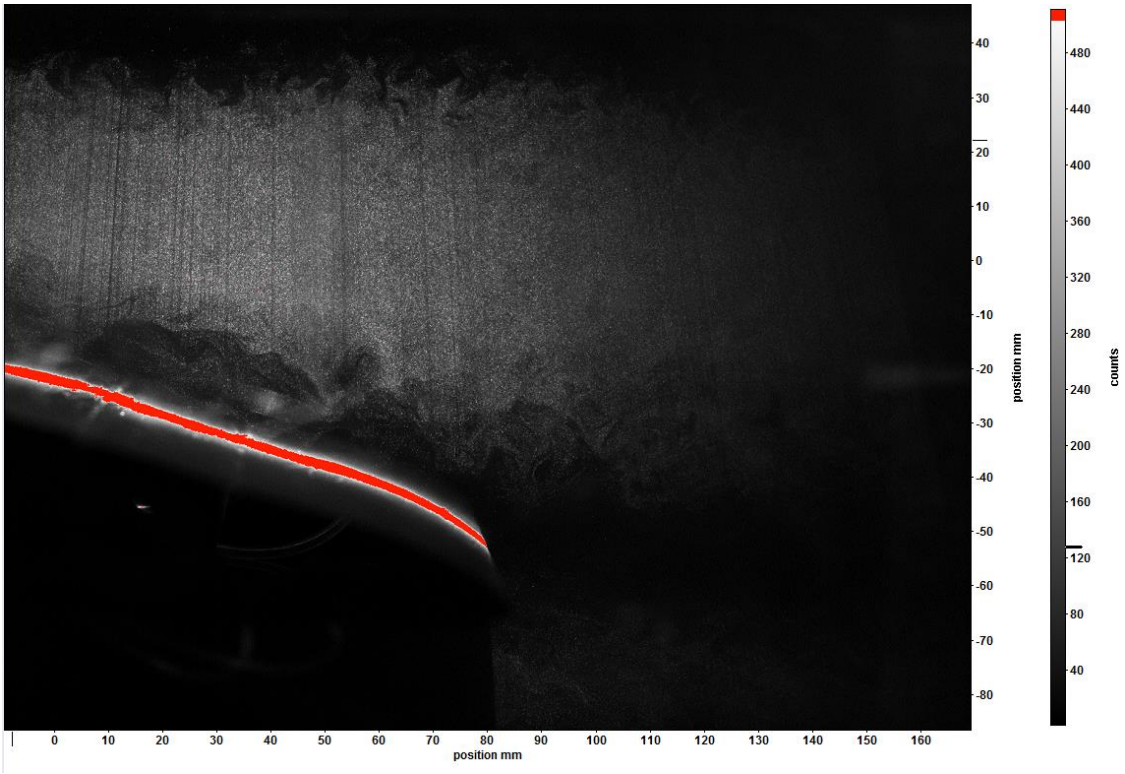

Figure 13. Trailing Camera Raw PIV Image

RESULTS AND DISCUSSION

Lift and Drag Predictions

XFLR-5 was used to generate lift and drag coefficients for the symmetric and deformed NACA 0021 geometries. The simulation was able to predict lift and drag for both geometries from nearly 0 to 17 degrees. The simulation assumed an infinite span for both geometries to calculate the optimal coefficients. Based on thin airfoil theory, both airfoils should have a linear lift slope area equal to 2π, but the simulations deviate slightly. The symmetric geometry was determined to have a slope of 1.7π, and the deformed geometry has a linear slope of 2.8π. Since both airfoil geometries are considered to be larger than a "thin" airfoil, it makes sense that the lift slopes are not exactly 2π. Thin airfoil theory also states that cambered airfoils like the deformed geometry do not run through the 0 AoA. Even though the simulation data does not completely reach 0 AoA, it can be seen that there will be a lift coefficient greater than 0 at 0 AoA. Despite having a larger lift slope, the deformed linear lift area only occurs up to 7.5 degrees while the symmetric linear slope continues till 10 degrees. After the linear slope region, both geometries have vastly different lift curves. The symmetric NACA 0021 appears to have no stalling effects up to 20 degrees with a nearly horizontal lift curve reaching a max lift coefficient of approximately 1. On the other hand, the deformed geometry experiences stall at 15 degrees reaching a max lift coefficient of 1.5. The lift coefficients calculated for the symmetric and deformed NACA 0021 geometries with respect to AoA are depicted in Figure 14. Unlike the lift curves, the drag curves predicted by XFLR-5 were similar in structure. Both airfoil geometries had parabolic drag curves, with the deformed geometry having a consistently larger drag coefficient of about 0.02 before stalling occurs in the deformed geometry. Figure 15 displays the predicted drag coefficient curves for both airfoils.

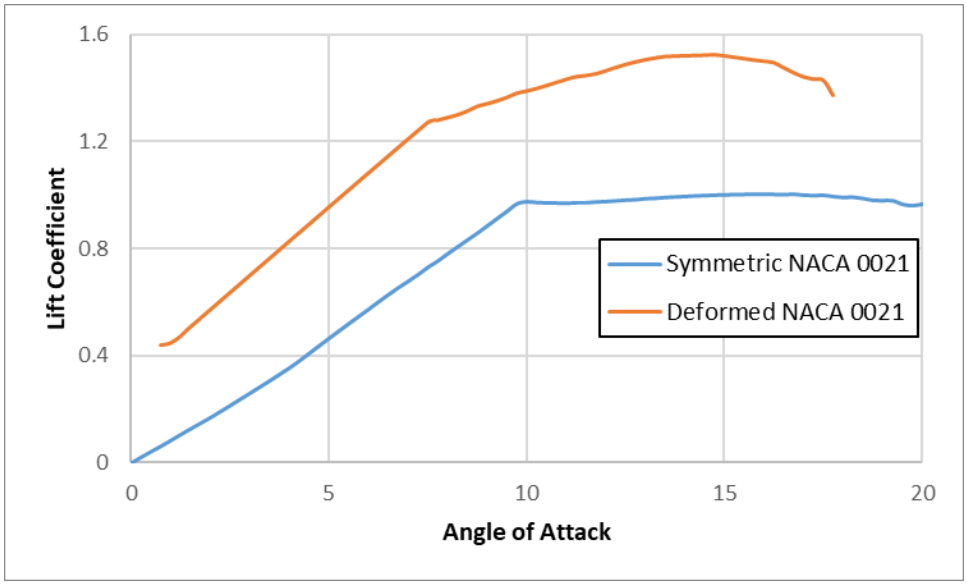

Figure 14. Comparison of Lift Coefficient

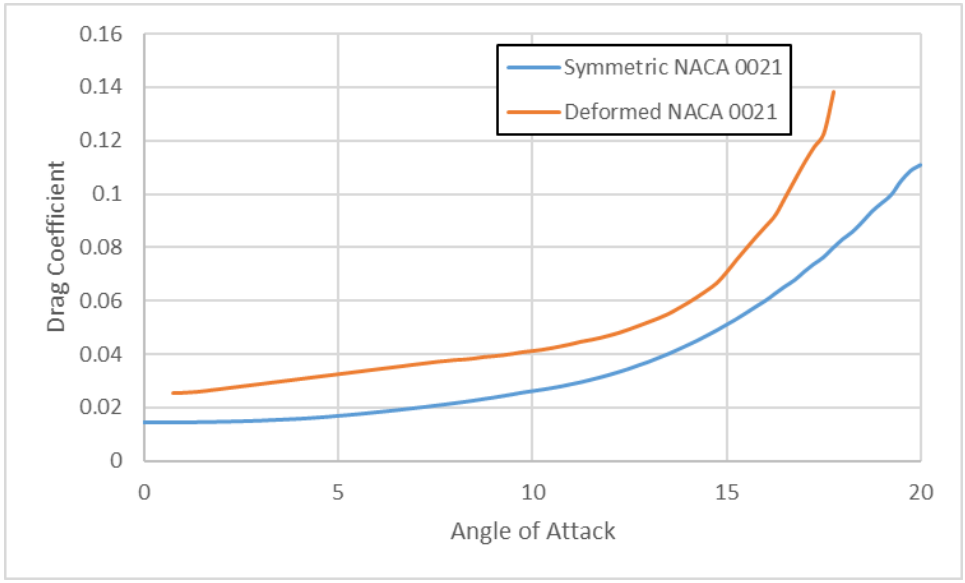

Figure 15. Comparison of Drag Coefficient

Apparent from Figure 16, the lift and drag of both geometries increase at nearly the same rate from 0 to 20 degrees. The only significant difference is between 0 and 5 degrees where the symmetric continues toward 0 and the cambered geometry trends toward 15. The symmetric and deformed reach similar max C_L/C_D values of 37 and 34, respectively. The increased lift versus drag at low AoAs is ideal during takeoff and landing. During cruising conditions, it appears that

the optimal geometry would be the symmetric airfoil since the extra lift would most likely not be necessary and the reduced drag would conserve fuel.

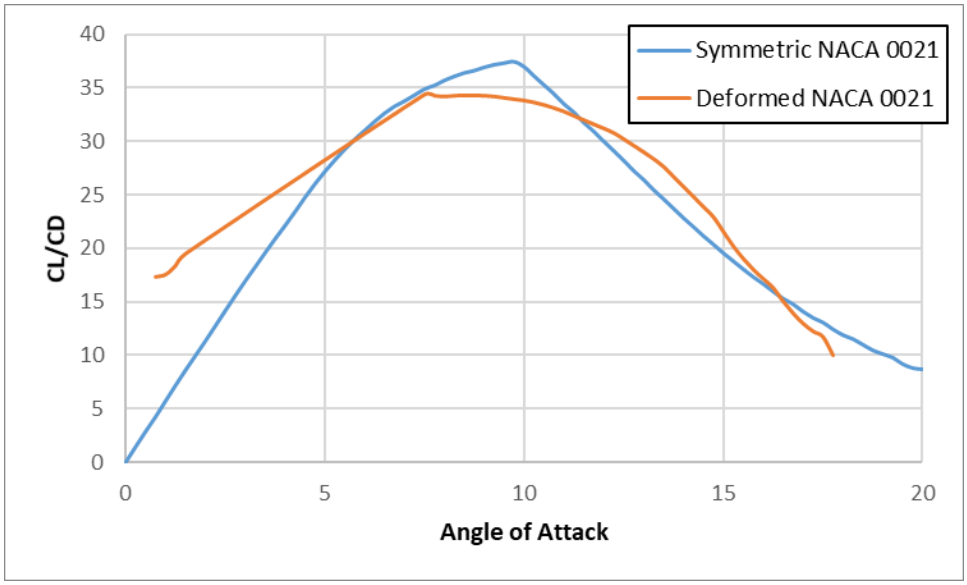

Figure 16. Comparison of Lift Coefficient/Drag Coefficient

Effects of Deforming NACA 0021

PIV Results

PIV was performed on the camber changing airfoil while inside the wind tunnel at a fixed freestream velocity. For both geometries, data was collected near the center span of the airfoil to minimize the downwash effects generated from the wing tip vortices. Without the use of end plates, the wing tip vortices are expected to affect the flow fields reconstructed during the PIV process. Therefore, the experimental AoA is predicted to contain an induced AoA effectively reducing the actual AoA experienced by the airfoil. Another important detail of the experimental process was that instead of recording separate data for the airfoil at each angle of attack and geometry, the airfoil was programmed to change shape during the experiment and change back. This resulted in the actuation cycle consisting of a period of symmetric geometry, followed by

the deformed geometry, and finishing with the symmetric geometry. To achieve this specific cycle, the microcontroller was activated after 10 seconds to obtain flow structures for the symmetric geometry, then it was actuated to maintain the deformed geometry for 10 seconds before returning the airfoil to its symmetric state. Allowing each phase of the airfoil to be present for 10 seconds with a data capture rate of 10 Hz made it possible use almost 100 images for the time-averaged results. PIV data was collected throughout the entire cycle, but the time-averaged PIV plots did not use images taken while the airfoil was in the actuation or return process. This way data would approximately be consistent for the geometries being evaluated.

Time-averaged PIV results for the symmetric and deformed geometries can be seen in Figures 17-26. In order to validate the use of time-averaged PIV velocity magnitude plots, the standard deviation plots are generally used; therefore, the standard deviation plots for each corresponding AoA and airfoil geometry are located in the Appendix. The leading edge images depicted as Figure 17 show there is very little variation between the two geometries at 10 degrees. The velocity magnitudes from the leading edge of the airfoil to the right side of the plots are nearly identical in values and distribution. As the plots show, the max velocity over the upper surface of the airfoil in both geometries is about 15 m/s compared to the freestream velocity of 10 m/s. The presence of the airfoil affects the flow above by increasing it to between 11 and 14 m/s. This is also seen at 12.5 and 15 degrees, so the images were not necessary to comment on and are present as in the Appendix. The remaining 10 AoA PIV plots show the trailing edge camera data before (symmetric geometry), during (deformed geometry), and after actuation (symmetric geometry). Since the airfoil chord was 150 mm in length, the cameras were able to capture overlapping data. The vertical black line in the PIV figures represent where the figures would align if the leading and trailing camera PIV images were combined. The black

curves on the PIV figures represent the airfoil surface. Due to masking constraints, data was collected in areas that the airfoil occupied for the deformed PIV figures. While the airfoil is symmetric, it experiences no areas of flow separation at 10 degrees. The velocity magnitude in the wake shows that the pressure on the bottom surface is greater than the pressure on the upper surface. With a velocity less than 10 m/s present on the bottom, the pressure can be assumed to be greater than the freestream pressure. This also reveals that the streamlines coming off the upper surface with velocity magnitudes greater than 10 m/s will have a pressure lower than the freestream pressure. The significantly decreased velocity at the tip of the trailing edge suggests that the geometry is on the verge of trailing edge based stall that will propagate upward across the upper surface with increased AoA. The near zero velocity magnitude at the trailing edge also suggests that the symmetric airfoil is about to leave the linear region of its lift curve. When the airfoil is deformed in the actuation cycle, the deformed geometry does experience flow separation occurring at 93% chord. With the flow separation just beginning to occurring, it can be determined that the geometry is no longer in the linear region of its lift curve. Using Figures 18-20 along with the predicted lift curves from Figure 14, the induced AoA for the experimental testing can be predicted to be around 2.5 degrees. After the deformation period, the airfoil geometry is returned to its symmetric state resulting in the flow to mimic the velocity field before the airfoil was deformed.

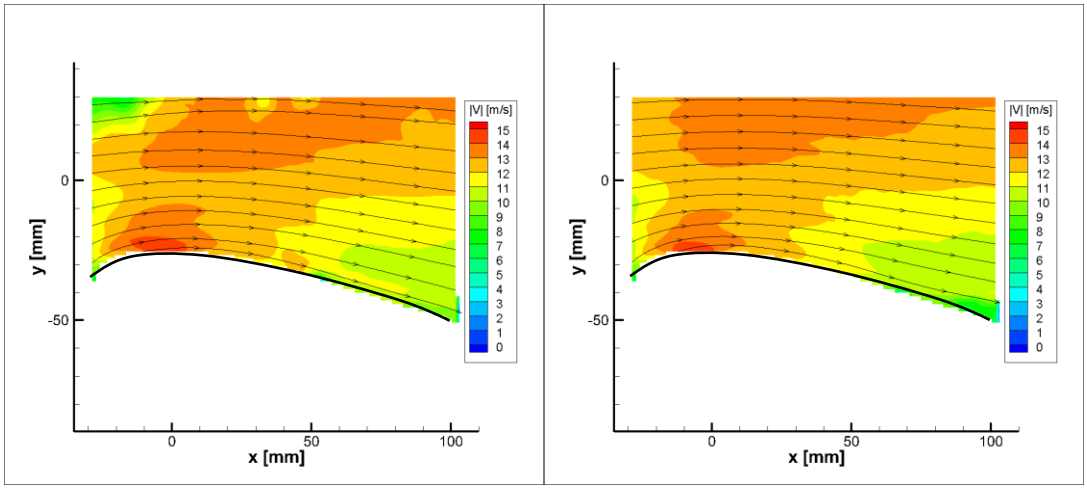

Figure 17. Time-Averaged Velocity Profile of NACA 0021 Airfoil (left) and Cambered Airfoil (right) at 10 AoA

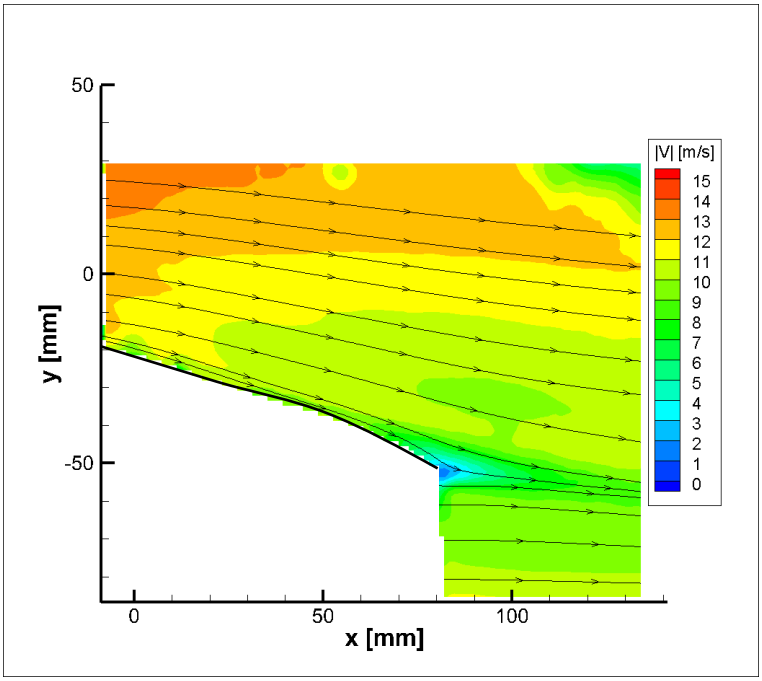

Figure 18. Time-Averaged Velocity Profile of NACA 0021 Airfoil at 10 AoA Before Applied Actuation

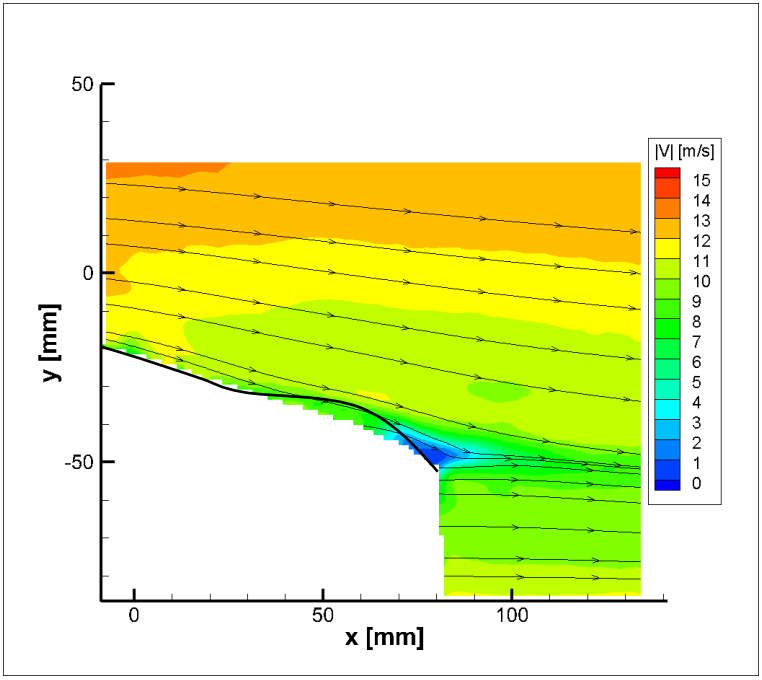

Figure 19. Time-Averaged Velocity Profile of Cambered Airfoil at 10 AoA During Applied Actuation

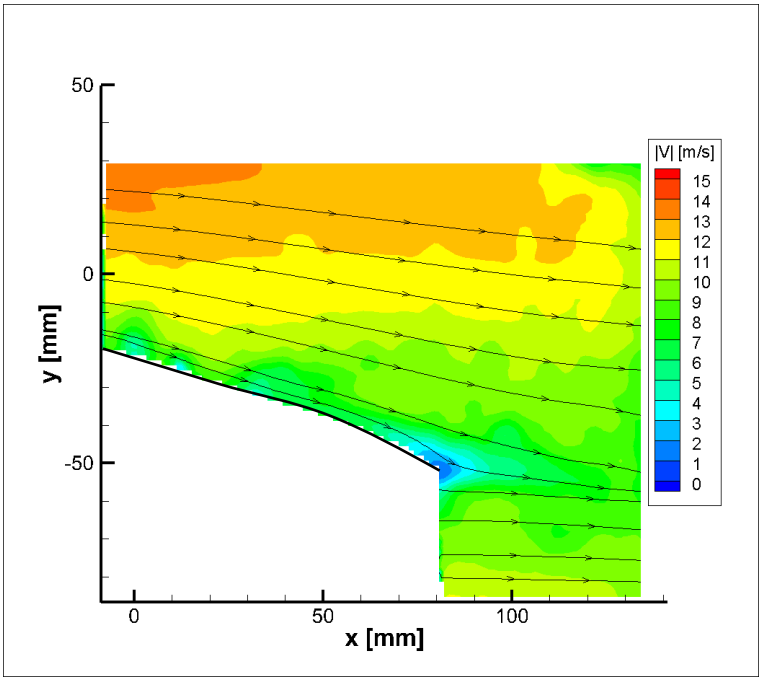

Figure 20. Time-Averaged Velocity Profile of NACA 0021 Airfoil at 10 AoA After Applied Actuation

As predicted, the separation layer develops further upstream on the upper surface of the airfoil for both geometries when the AoA is increased to 12.5 and 15 degrees. For the symmetric

geometry at 12.5 and 15 degrees, the flow has separated enough from the surface for it to be quantified with beginning respectively at 93% and 89% chord before actuation has occurred. When the airfoil is deformed to its cambered geometry, the separation increases to 86% and 65% chord. The only variation in the velocity magnitudes between the symmetric and camber geometries is located between x = 50 and 150 mm. Along the streamlines just above the surface of the airfoil, the velocity magnitude is about 1 m/s faster for the cambered airfoil. This could also suggest that the pressure on the cambered airfoil's upper surface is less than that of the symmetric airfoil. At 12.5 degrees, the flow is still beginning to separate at a slow rate, but as seen for the deformed geometry at 15 degrees, stalling is about to occur. Based on the flow fields calculated for the 12.5 and 15 degree cases, the induced AoA can be determined to be around 2.5-3 degrees. This is consistent with the induced AoA predicted for 10 degrees. As with any finite wing, the lift curve is not identical to that of 2D infinite wing predictions, but the lift curves still give insight to the overall performance of the geometry. The predicted induced AoA will also generate an induced drag force, but from the PIV images it is irrelevant without evaluating the inlet and outlet flows to theoretically measure lift and drag based on the flow velocities. Similar with the PIV plots at 10 degrees, the time-averaged flow fields for 12.5 and 15 degrees before and after actuation are nearly identical with slight velocity magnitude differences. With the flow fields returning to their original state, it indicates that the long term cyclic process of altering the geometry does not affect the overall flow around the airfoil. This is ideal when considering the applications of this flow control method.

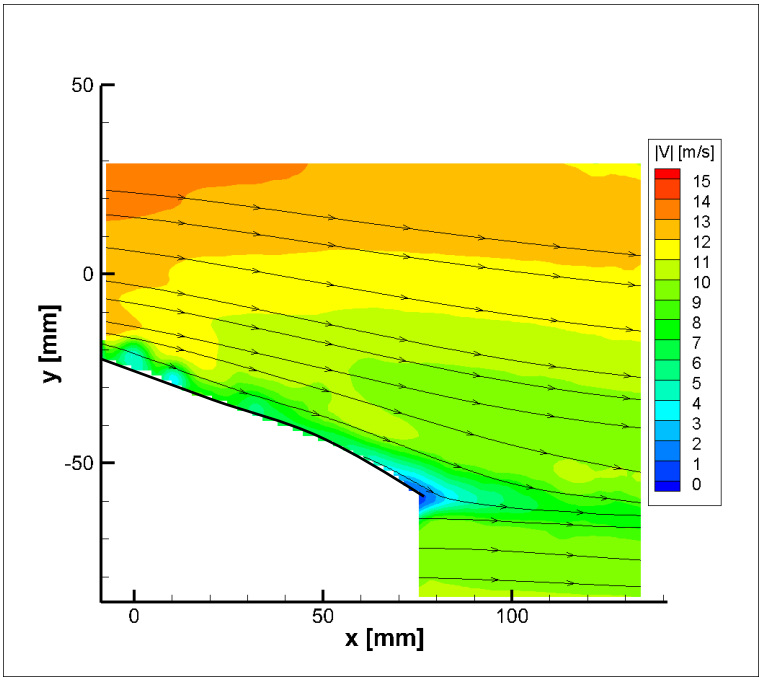

Figure 21. Time-Averaged Velocity Profile of NACA 0021 Airfoil at 12.5 AoA Before Applied Actuation

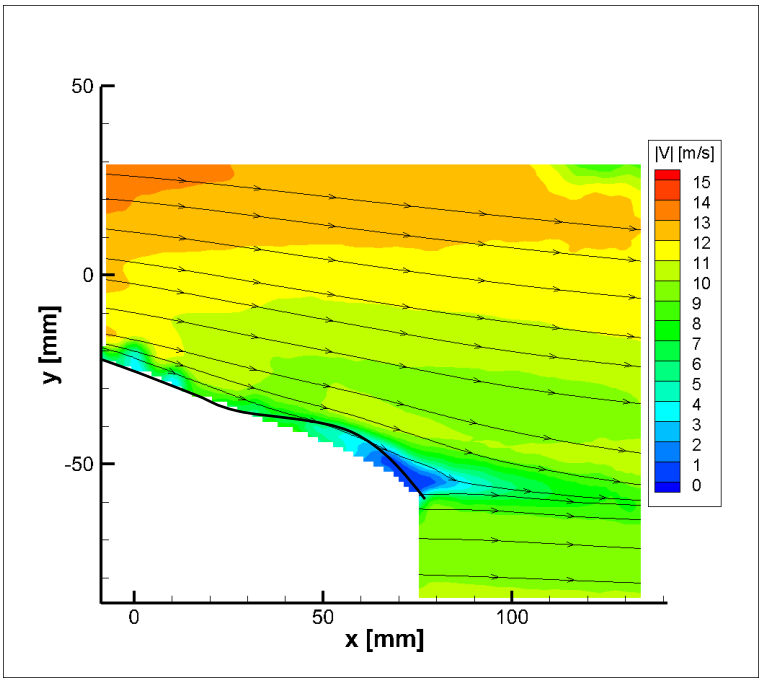

Figure 22. Time-Averaged Velocity Profile of Cambered Airfoil at 12.5 AoA During Applied Actuation

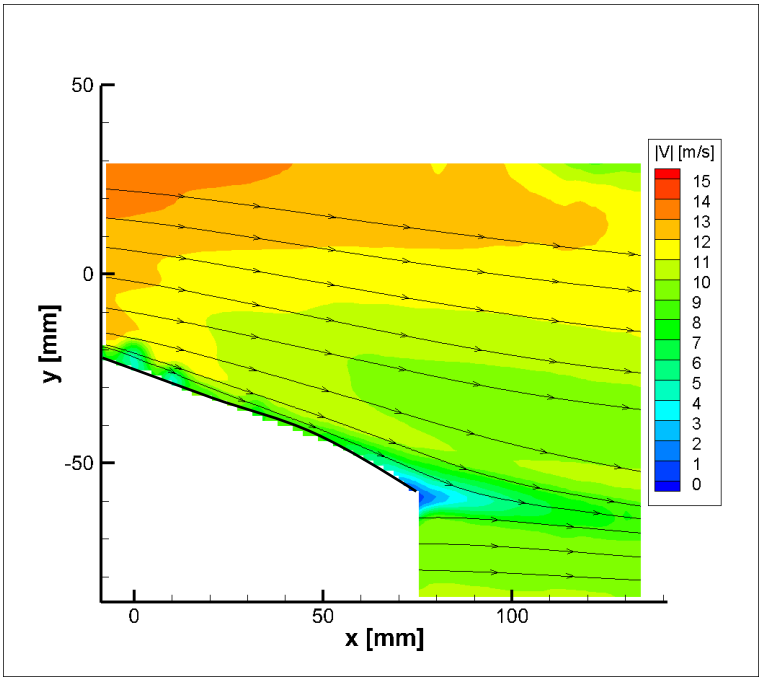

Figure 23. Time-Averaged Velocity Profile of NACA 0021 Airfoil at 12.5 AoA After Applied Actuation

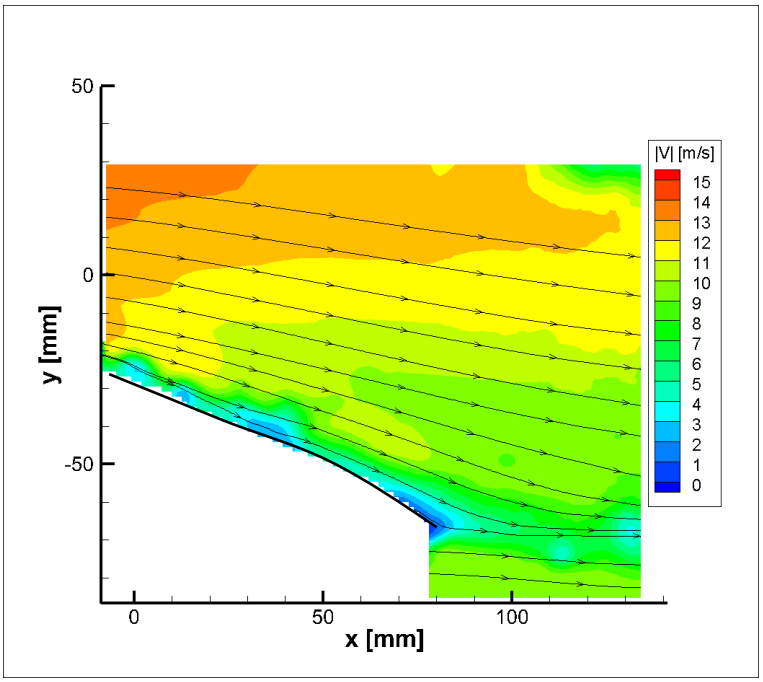

Figure 24. Time-Averaged Velocity Profile of NACA 0021 Airfoil at 15 AoA Before Applied Actuation

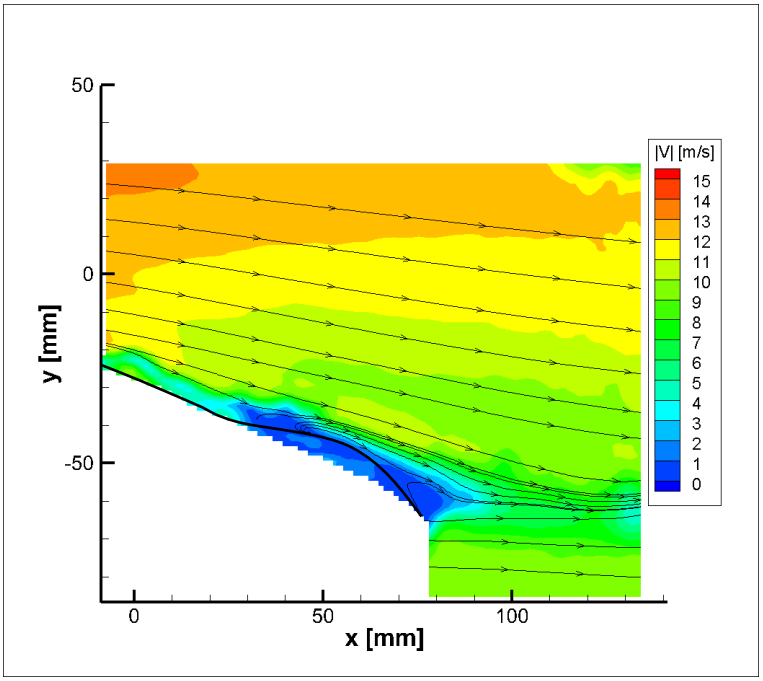

Figure 25. Time-Averaged Velocity Profile of Cambered Airfoil at 15 AoA During Applied Actuation

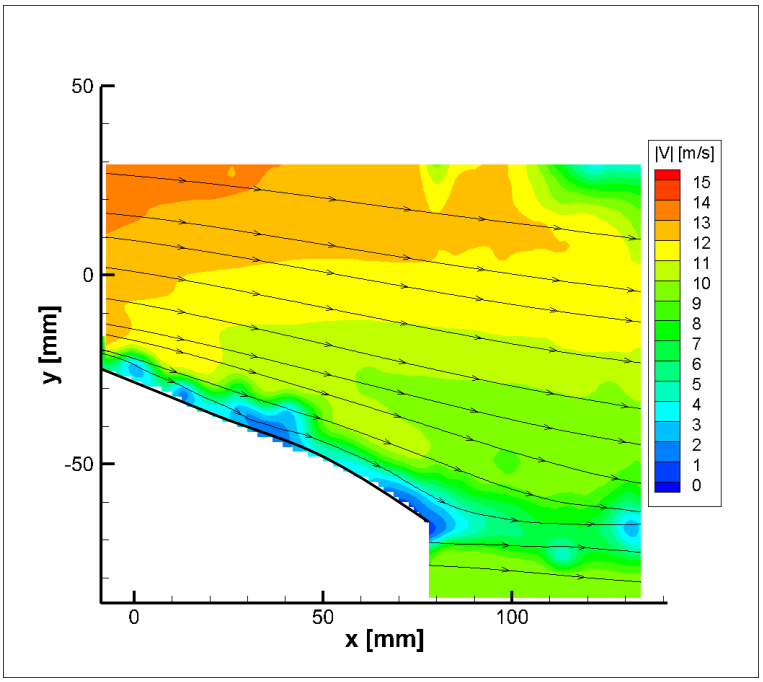

Figure 26. Time-Averaged Velocity Profile of NACA 0021 Airfoil at 15 AoA After Applied Actuation

Time-averaged PIV plots are ideal for clearly showing the location of flow separation that occurs at higher AoAs, but they lack at visualizing vortex generation on the upper surface of the airfoil and vortex shedding in the wake. The instantaneous velocity vector plots for 0, 10, 12.5 and 15 degrees are seen in Figures 27-36. At 0 degrees, the symmetric airfoil's velocity flow field shows no separation with velocity slowing at the trailing edge due to the merging of upper and lower surface velocities. The cambered airfoil geometry experienced some separation but only in areas trailing the deformed region. At 10 degrees, both geometries have flow fields that resemble the time-averaged flow fields. The symmetric geometry, in both scenarios, has no separation while the cambered geometry is beginning to show separation near the trailing edge. There is also no vortex generation occurring at 10 degrees for both airfoil geometries like in the time-averaged flow fields. However, the instantaneous flow fields at 12.5 and 15 AoA depict a different picture of the flow occurring across the upper surface of the airfoil. For both geometries at 12.5 and 15 AoA, vortex generation occurs along the upper surface of the airfoil and moves along the surface before being shed into the trailing wake. At 12.5 degrees, the vortices generated appear to be very small in diameter and don't appear in every reconstructed flow field. When the AoA is increased to 15 degrees, the vortices generated appear to occur more often and are larger in diameter. In some cases, several vortices are captured in the same frame as seen in Figure 37. This is different than what the time-averaged PIV plots showed with only separation occurring at 89% chord. Examination of Figure 38 shows that the cambered geometry experiences slightly more vorticity occurring upstream of the deformed region. This is denoted by the light and dark blue regions presented more prominently for the cambered geometry. The cambered airfoil also reaches a lower vorticity with a minimum value of about $-5\ s^{-1}$ compared to the symmetric airfoils minimum of $-4\ s^{-1}$. However, it is seen that the wake of

both geometries are very similar. Both wakes have areas of high and low vorticity. Comparing the vector plots in Figure 38 confirm the vorticity present in the flow fields at 15 degrees AoA.

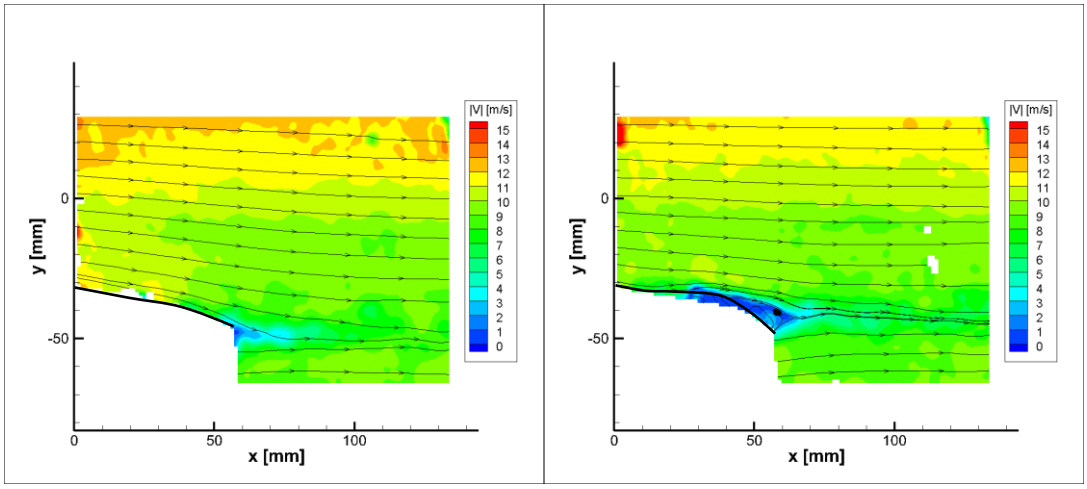

Figure 27. Instantaneous Velocity Profile of Trailing Edge Flow Fields for the NACA 0021 (left) and Cambered Airfoil at 0 AoA

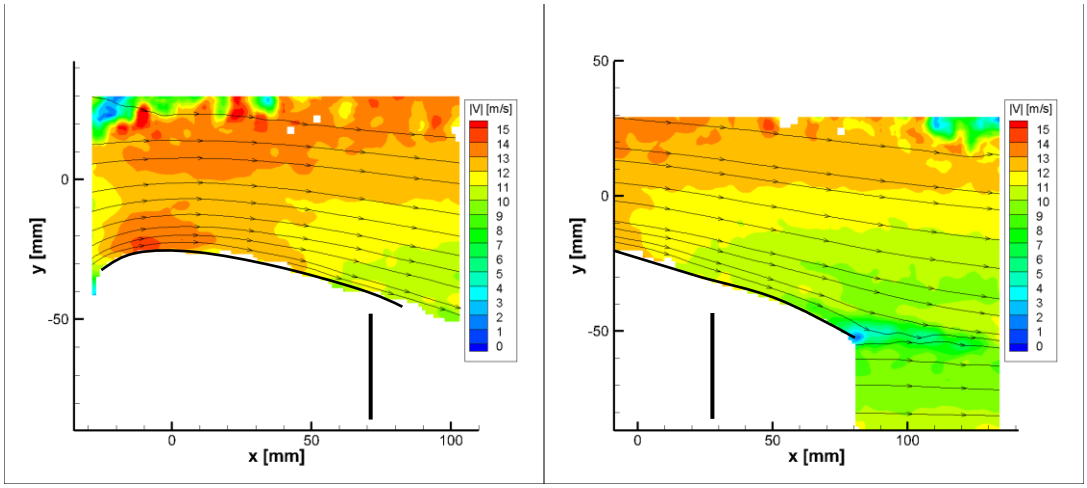

Figure 28. Instantaneous Velocity Profile of Leading Edge (left) and Trailing Edge (right) Flow Fields for the NACA 0021 Airfoil at 10 AoA Before Actuation

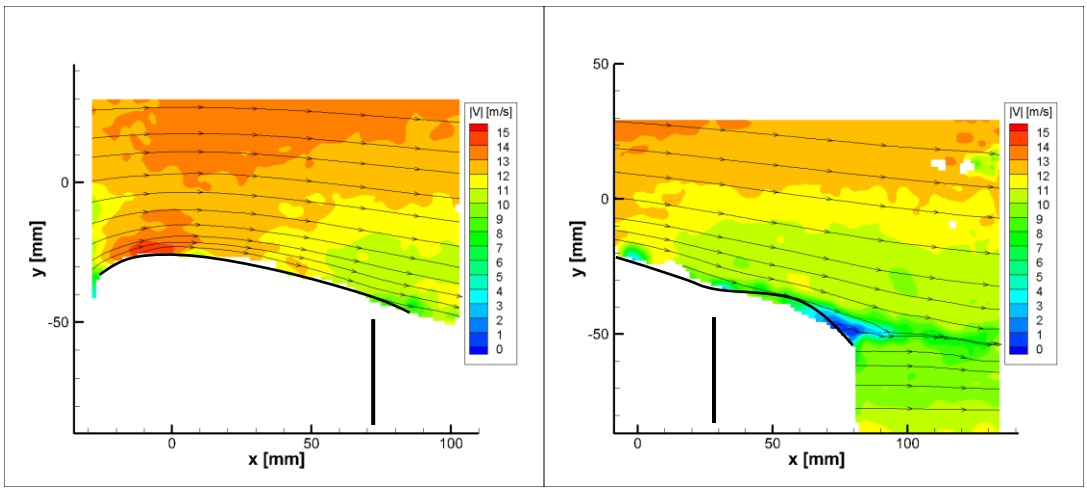

Figure 29. Instantaneous Velocity Profile of Leading Edge (left) and Trailing Edge (right) Flow Fields for the Cambered Airfoil at 10 AoA During Actuation

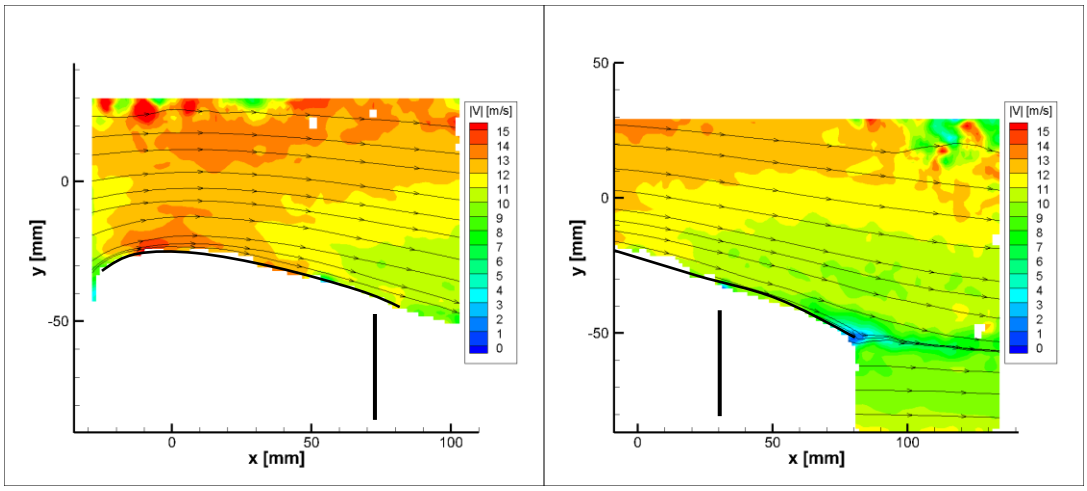

Figure 30. Instantaneous Velocity Profile of Leading Edge (left) and Trailing Edge (right) Flow Fields for the NACA 0021 Airfoil at 10 AoA After Actuation

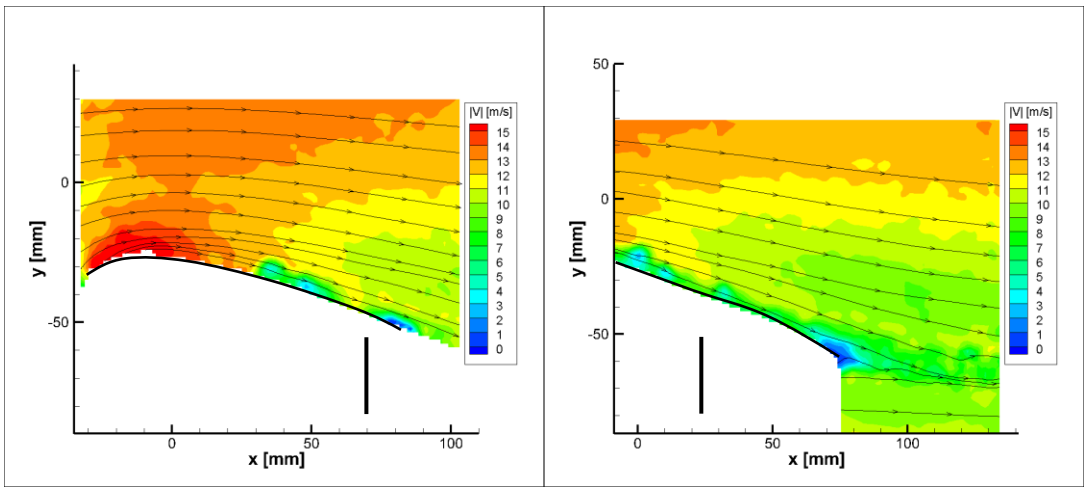

Figure 31. Instantaneous Velocity Profile of Leading Edge (left) and Trailing Edge (right) Flow Fields for the NACA 0021 Airfoil at 12.5 AoA Before Actuation

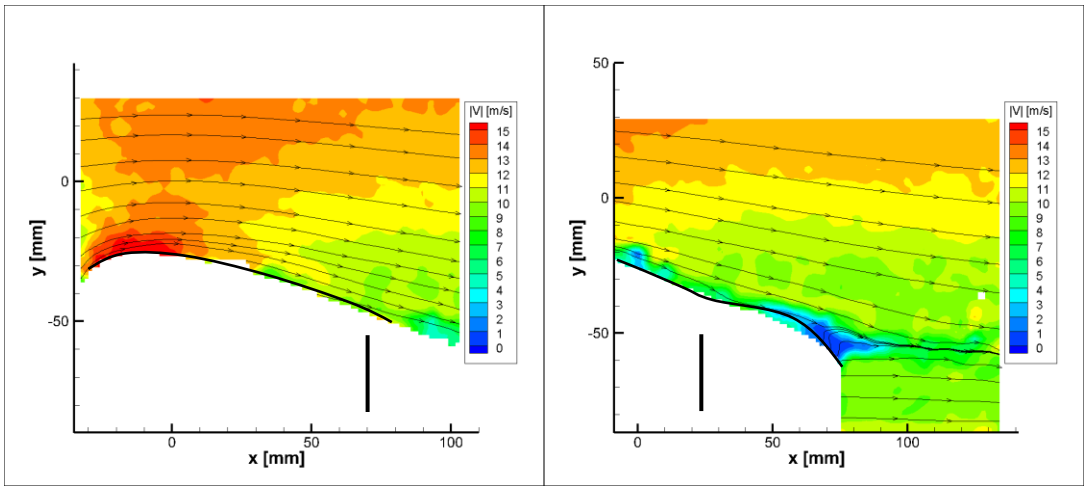

Figure 32. Instantaneous Velocity Profile of Leading Edge (left) and Trailing Edge (right) Flow Fields for the Cambered Airfoil at 12.5 AoA During Actuation

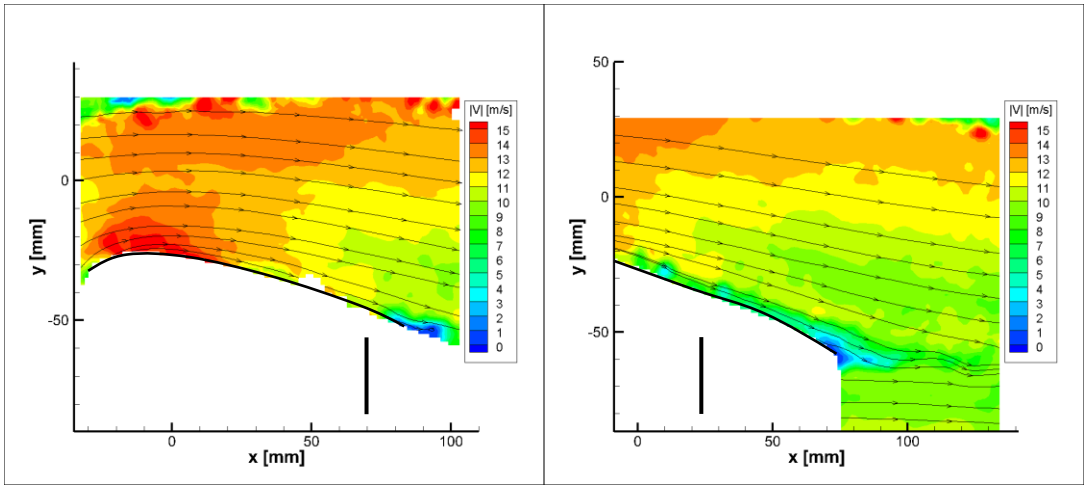

Figure 33. Instantaneous Velocity Profile of Leading Edge (left) and Trailing Edge (right) Flow Fields for the NACA 0021 Airfoil at 12.5 AoA After Actuation

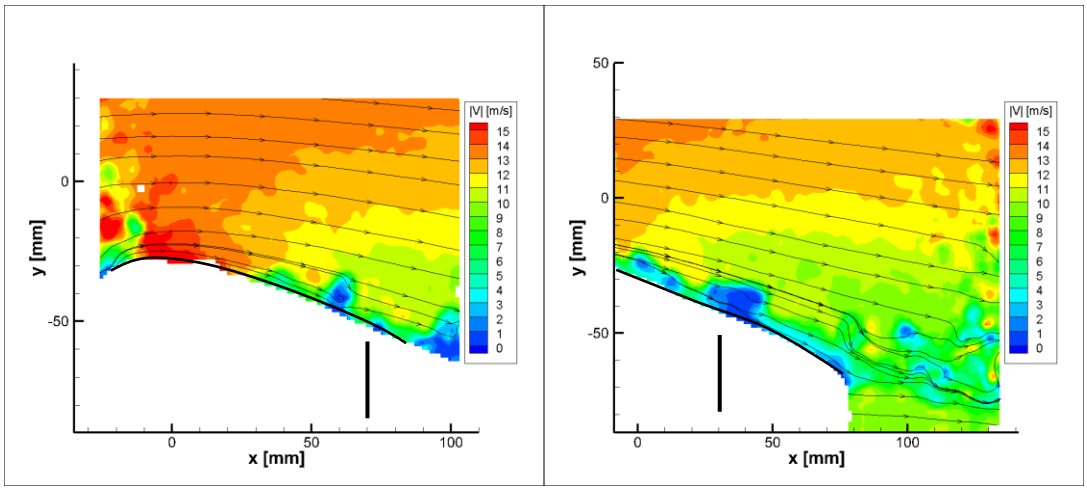

Figure 34. Instantaneous Velocity Profile of Leading Edge (left) and Trailing Edge (right) Flow Fields for the NACA 0021 Airfoil at 15 AoA Before Actuation

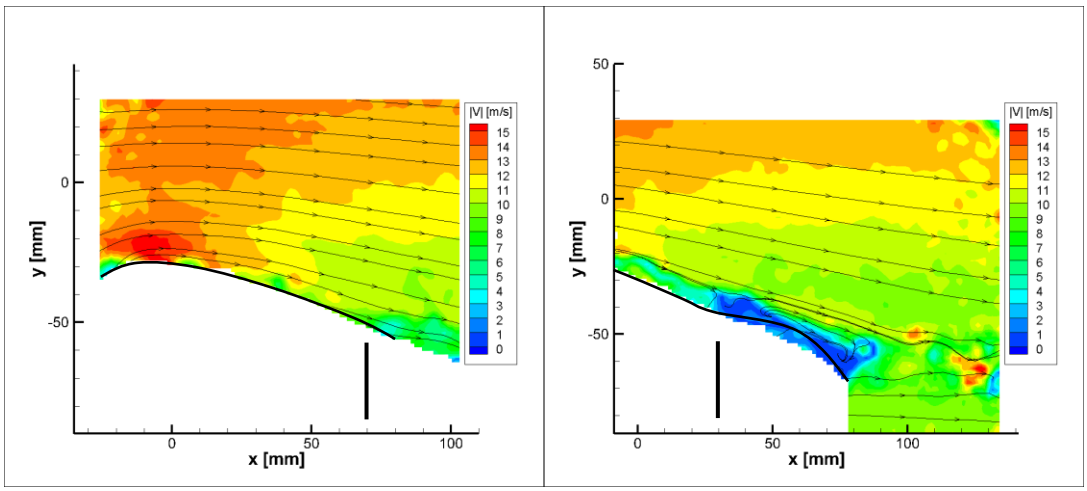

Figure 35. Instantaneous Velocity Profile of Leading Edge (left) and Trailing Edge (right) Flow Fields for the Cambered Airfoil at 15 AoA During Actuation

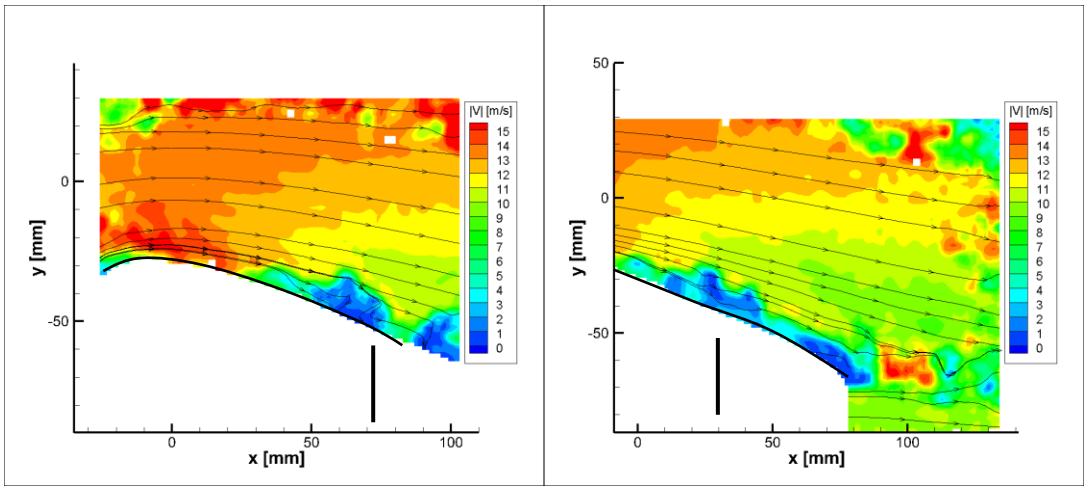

Figure 36. Instantaneous Velocity Profile of Leading Edge (left) and Trailing Edge (right) Flow Fields for the NACA 0021 Airfoil at 15 AoA After Actuation

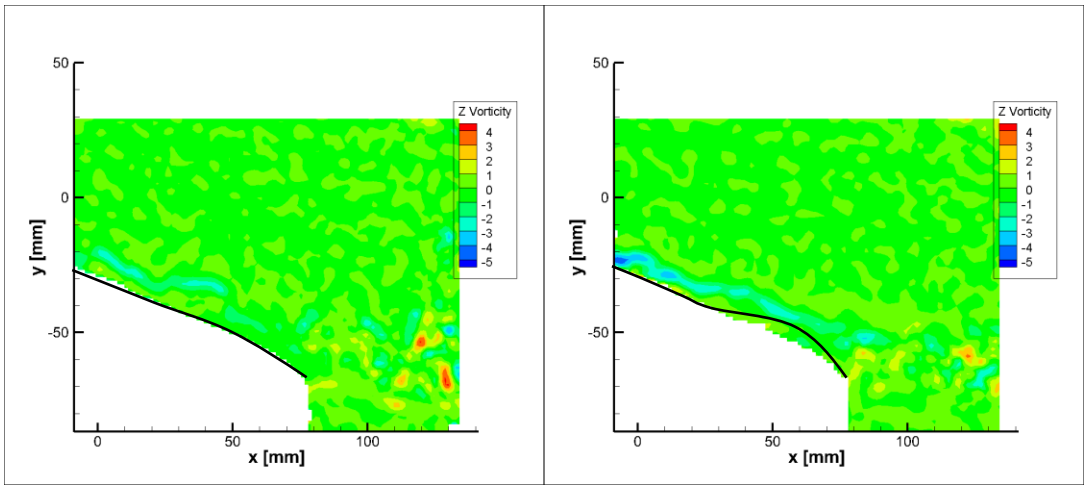

Figure 37. Contour Profile of Z Vorticity (s^{-1}) for NACA 0021 (left) and Cambered Airfoil (right) at 15 AoA

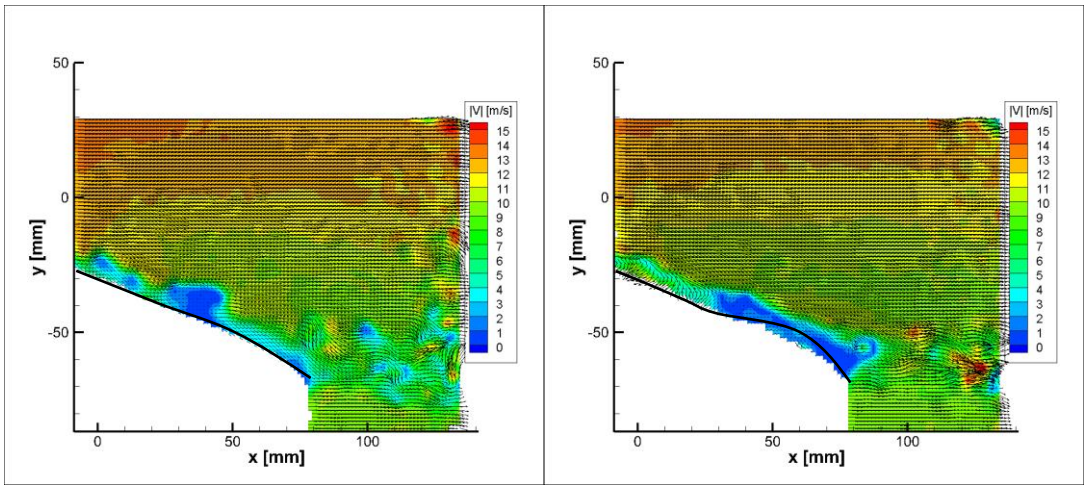

Figure 38. Instantaneous Velocity Vector Profile of NACA 0021 (left) and Cambered Airfoil (right) at 15 AoA

Comparing the time-averaged flow field of the cambered airfoil at 15 AoA to its corresponding instantaneous flow field, it surprisingly is almost an identical match. Therefore, the change in camber of the airfoil seems to have an impact on the flow stability in this specific case with the cambered airfoil having a near steady flow field while the symmetric airfoil has a very unsteady flow field over the airfoil's surface. By comparing the time-averaged and instantaneous flow fields, it can be shown that both flow fields have some similar flow

structures, but there is a several aspects of the flow that are described differently. This is why it is important to assess both when evaluating airfoils.

Effects of Actuation Frequency

Evaluation of the two airfoil geometries with time-averaged and instantaneous PIV determined what flow structures would develop when those geometries were used over long periods, but failed to determine the effects actuation frequency would have on the flow fields. To account for this, the airfoil was again tested at AoAs of 10, 12.5, and 15 degrees but the actuation frequency was set to 0.33, 0.167, or 0.11 Hz. The frequencies were determined based on the actuation capabilities of the nitinol wire. At its fastest, the wire can contract in 1 second and lengthen in 2 seconds. This relates to a cycle frequency of 0.33 Hz. From there, the total cycle period was doubled and tripled to 6 and 9 seconds to obtain frequencies of 0.167 and 0.11 Hz. Because the experiment involved a periodic actuation reducing the available reconstructed PIV flow fields, it was best to use instantaneous PIV to evaluate the frequencies. The instantaneous PIV results for the airfoil geometries at 10 AoA for the three frequencies are located in Figures 39-41. For all the frequencies at an AoA of 10 degrees, the NACA 0021 flow field velocity distributions matched that of the NACA 0021 geometry's flow field velocities in-between actuation cycles, therefore, it was irrelevant to include the plots. The cambered geometry also had similar PIV plots as the instantaneous PIV plots for the deformed geometry from the previous section. The same results were discovered at 12.5 degrees and are visible in Figures 42-44.

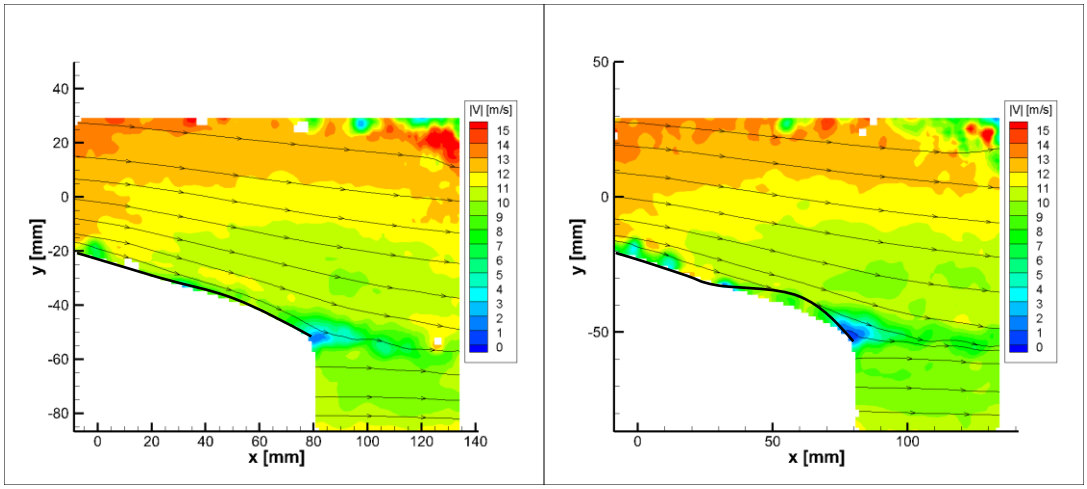

Figure 39. Instantaneous Velocity Profile of NACA 0021 (left) and Cambered (right) Airfoil Geometries at 10 AoA and an Actuation Frequency of 0.33 Hz

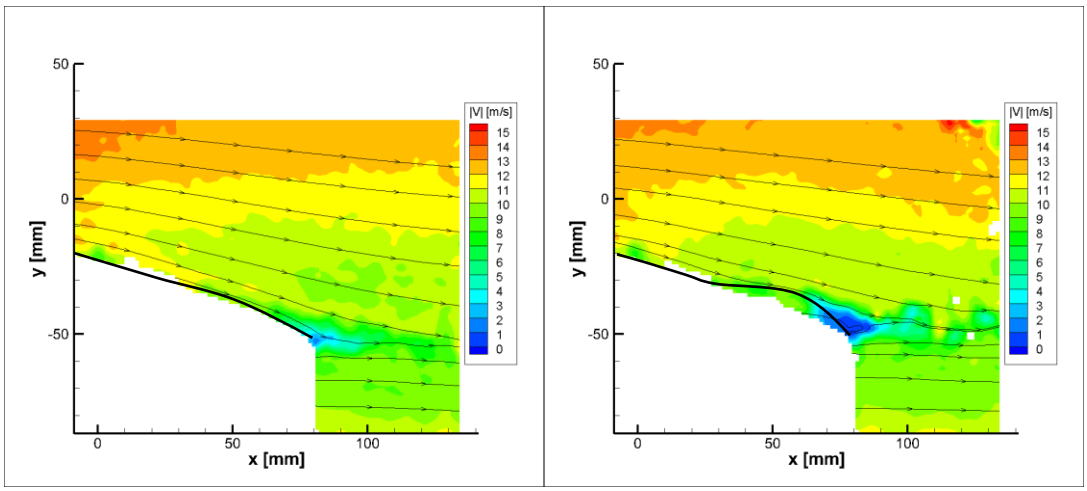

Figure 40. Instantaneous Velocity Profile of NACA 0021 (left) and Cambered (right) Airfoil Geometries at 10 AoA and an Actuation Frequency of 0.167 Hz

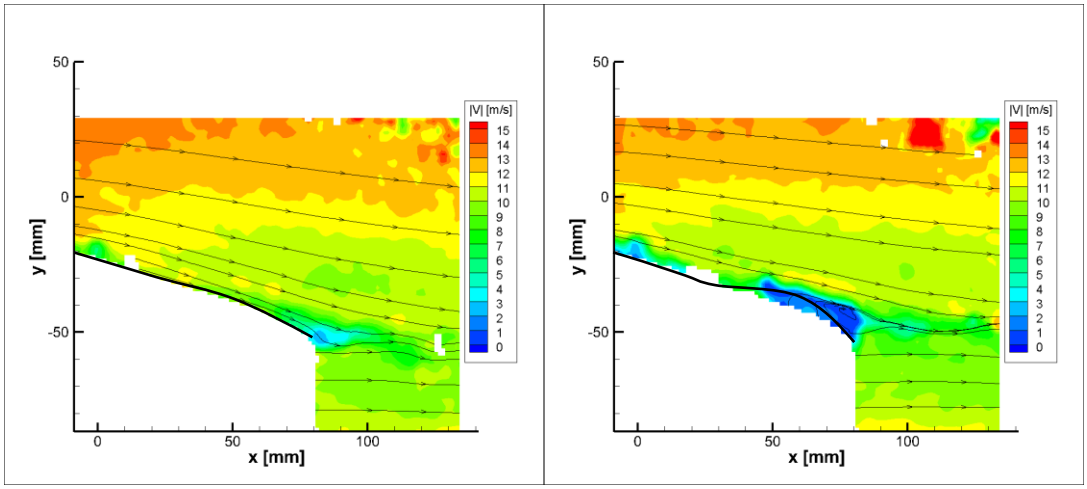

Figure 41. Instantaneous Velocity Profile of NACA 0021 (left) and Cambered (right) Airfoil Geometries at 10 AoA and an Actuation Frequency of 0.11 Hz

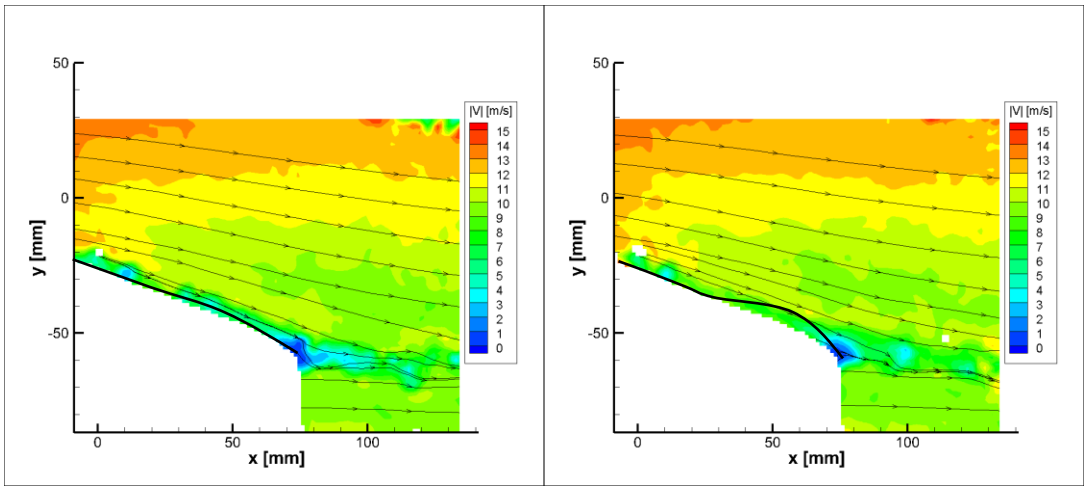

Figure 42. Instantaneous Velocity Profile of NACA 0021 (left) and Cambered (right) Airfoil Geometries at 12.5 AoA and an Actuation Frequency of 0.33 Hz

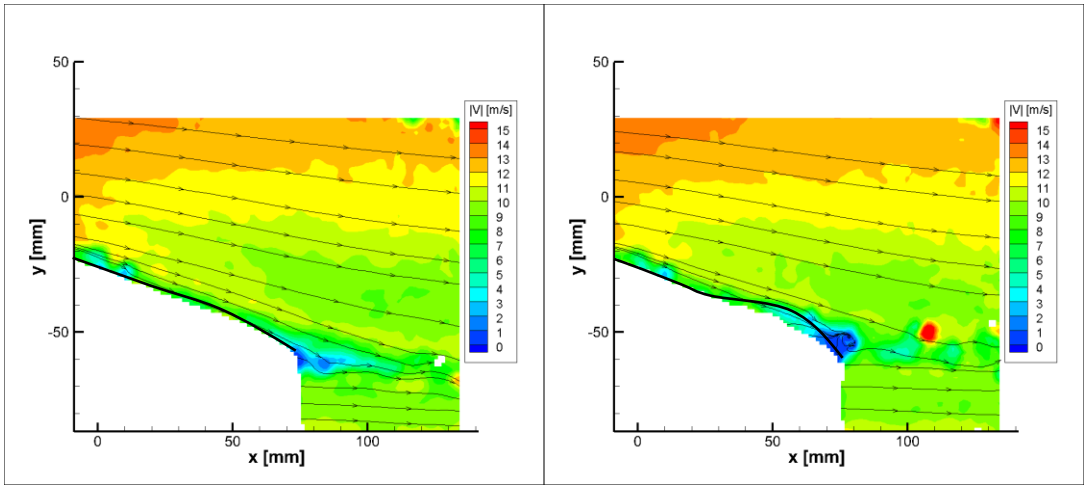

Figure 43. Instantaneous Velocity Profile of NACA 0021 (left) and Cambered (right) Airfoil Geometries at 12.5 AoA and an Actuation Frequency of 0.167 Hz

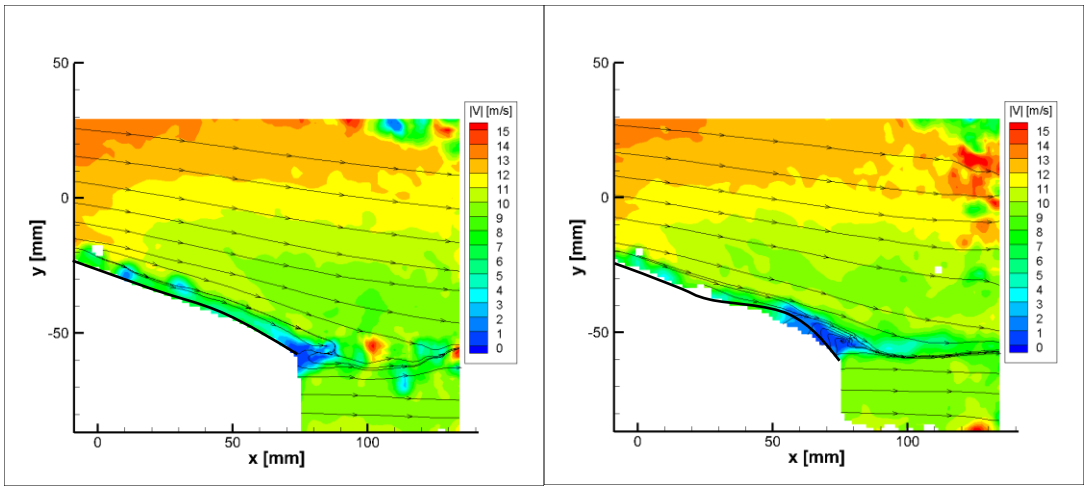

Figure 44. Instantaneous Velocity Profile of NACA 0021 (left) and Cambered (right) Airfoil Geometries at 12.5 AoA and an Actuation Frequency of 0.11 Hz

Even though the before and in-between cycle results were the same at an AoA of 10 and 12.5 degrees, did not mean they were the same at larger AoAs. When the airfoil was pitched to 15 degrees, variations were present between the starting NACA 0021's flow field and the flow field in-between actuation cycles. Before an applied actuation frequency of 0.33 Hz, the NACA 0021 airfoil experiences little separation at the trailing edge. Like that of the PIV plots gathered during the experiments excluding actuation frequency, the 0.33 Hz actuation to the cambered

airfoil drastically increases the separation layer present on the upper surface of the airfoil. The main difference between the actuation frequency results and the geometry results at an AoA of 15 degrees is that after the airfoil is actuated at 0.33 Hz and is in-between another actuation cycle, the separation present for the cambered geometry is now present for the symmetric geometry. This may be caused by the "high" frequency with respect to freestream velocity, in which the flow may not have enough time to return to its stable state before another actuation cycle occurs. This is corroborated when comparing the 0.33 Hz data with the 0.167 and 0.11 Hz results shown in Figures 45-47.

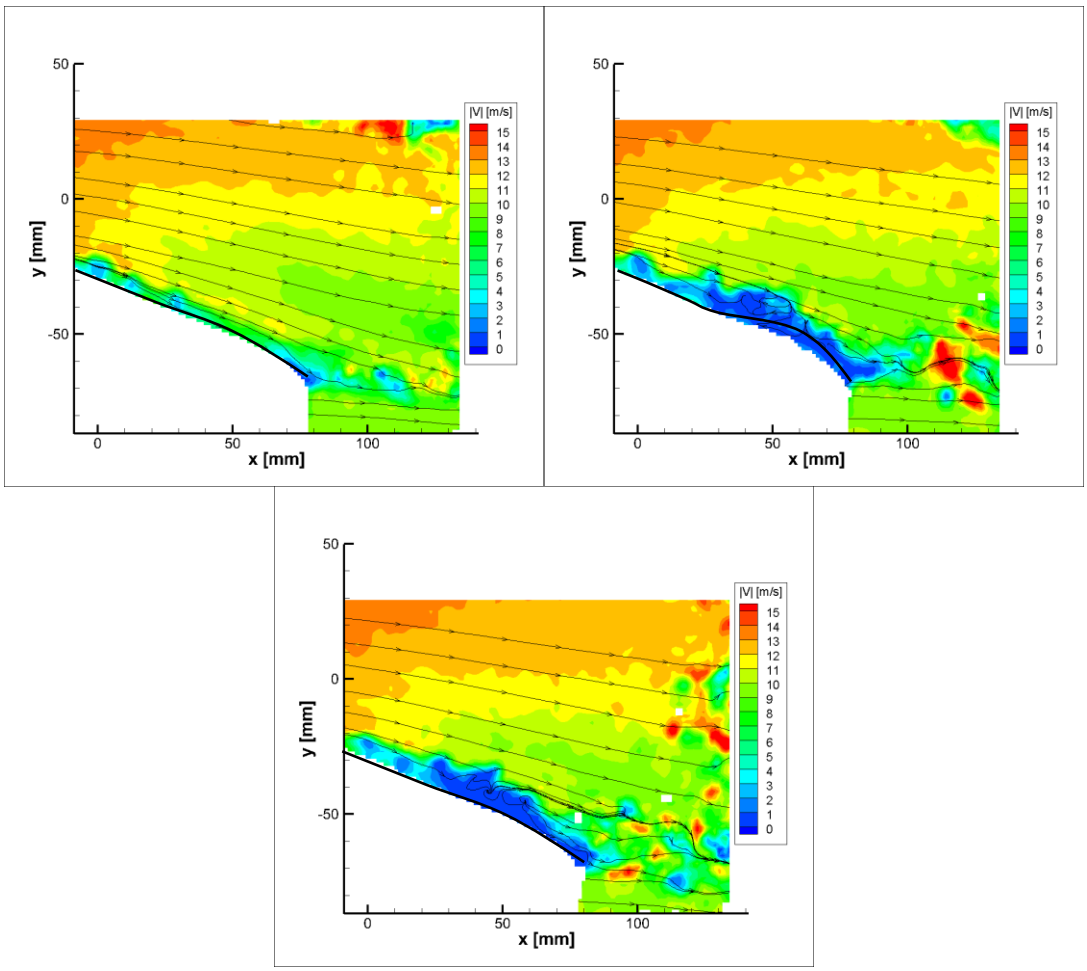

Figure 45. Instantaneous Velocity Profile of Experimental Airfoil Before (top left), During (top right), and In-between (bottom) Actuation Cycles at 15 AoA and 0.33 Hz

The 0.33 Hz PIV data for the NACA 0021 and cambered geometries shows a different relationship between the actuation frequency and the flow over the upper surface of the airfoil. Only at 0.33 Hz does the flow remain separated after the actuation cycle has ended and before another begins. At 0.167 Hz, it seems that the flow has just about returned to its stable state since the flow at the trailing edge of the airfoil slightly varies from the before actuation to the after actuation cycle PIV plots. Lastly, the PIV results for 0.11 Hz at 15 AoA shows the same flow fields for the before actuation as the after actuation case. This supports the notion that at larger actuation frequencies, the flow is not provided enough time to adjust after the geometry is changed from the cambered to the symmetric orientation.

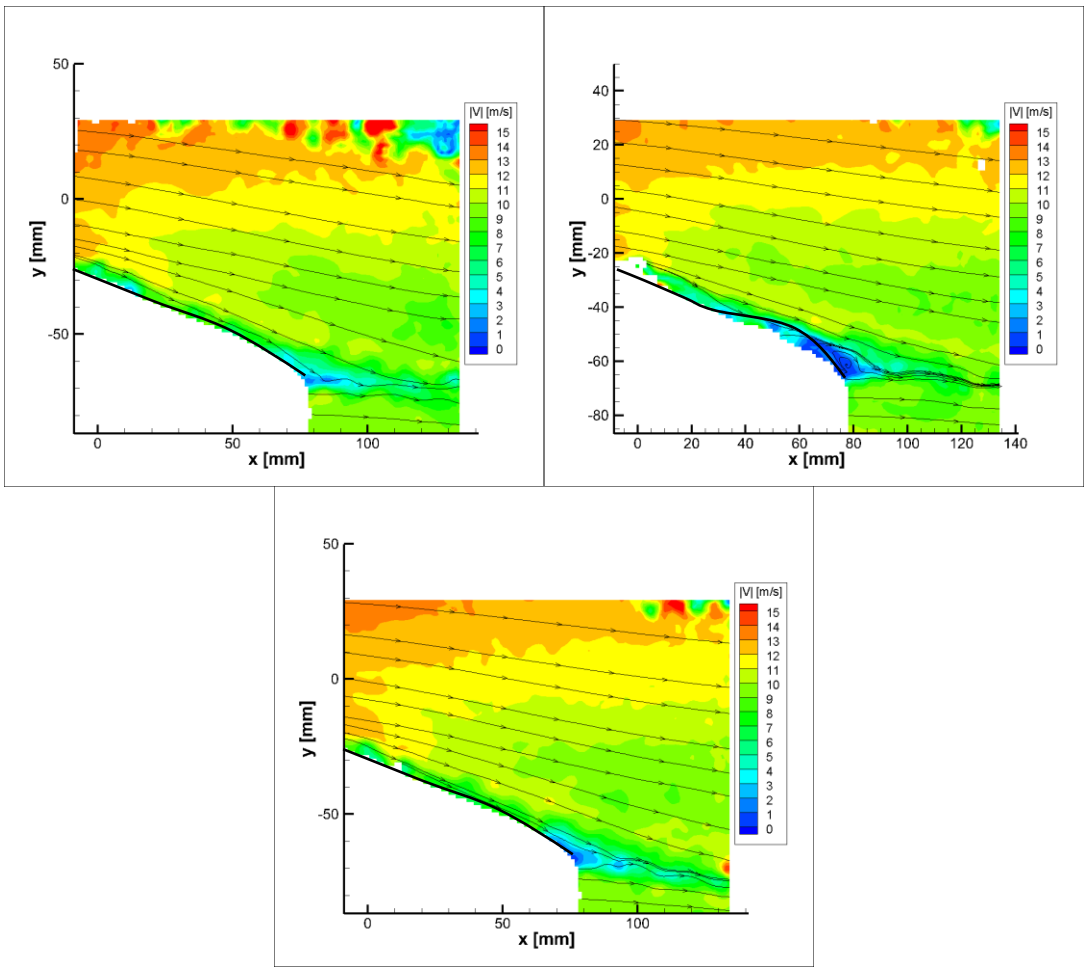

Figure 46. Instantaneous Velocity Profile of Experimental Airfoil Before (top left), During (top right), and In-between (bottom) Actuation Cycles at 15 AoA and 0.167 Hz

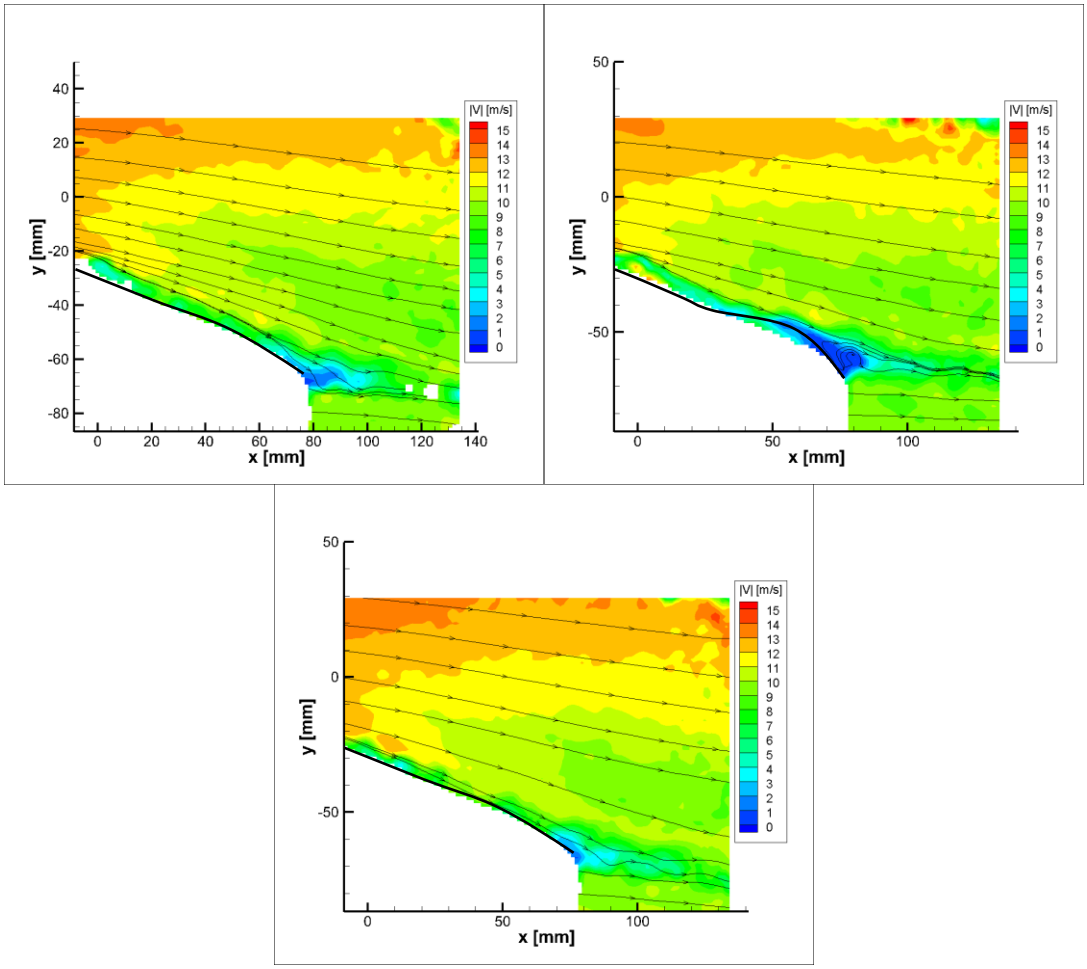

Figure 47. Instantaneous Velocity Profile of Experimental Airfoil Before (top left), During (top right), and In-between (bottom) Actuation Cycles at 15 AoA and 0.11 Hz

Comparison to Conventional Actuators

Current commercial, military, and personal aircraft use hydraulic and electric linear actuation methods to control their airfoil flaps. This has been the method for tens of years to alter the lift and drag during takeoff and landing as well as cruising. Even though this technique has been around for a long time, the equipment used to create the actuation is heavy and consumes large amounts of energy to operate. Being able to substitute the current methods with lightweight actuators would be more ideal to reduce fuel consumption. The use of nitinol may be a substitute for the current actuators used in industry. Comparing the nitinol used in the

actuated airfoil to current aircraft actuators is hard to accomplish due to scaling complications, but a comparison can be made with alternatives to actuating the experimental airfoil. To actuate the experimental airfoil with the same stroke and force, replacement actuators would have to have a combined stroke of at least 4-5 mm and an applicable force of 50 N. Since hydraulics are not common in the size required to be incorporated into the airfoil the method of actuation would be substituted with electric linear actuators. Two linear actuators that would be viable replacements for the nitinol wire are the L16 and PQ12 actuators. The specification documents are located in Appendix X for reference. The L16 is larger than the PQ12 and delivers a larger force and stroke. In order to obtain an assumed 2D deflection like with the nitinol and with applying the same force, 2 L16 actuators of a 35:1 gearing ratio or 2 PQ12 actuators of a 63:1 gearing ratio would be required. Both provide strokes larger than 5 mm, therefore, they would be viable replacements for the nitinol wires. The main downside to these actuators is that each L16 weighs 56 g and each PQ12 weighs 15 g [32]. The nitinol wire used inside the airfoil weighs less than 1 g. This is at least 29 g less than the smaller actuator replacement. The approximate power required to contract both actuators within 1 second is about 7 W and 4.5 W, respectively. Using Equations 5 and 6, the required power for the nitinol wire is calculated to be approximately 16.4 W. Despite having a larger estimated power requirement, the nitinol is still a small fraction the weight. The large reduction is mass is present when comparing the ratio of force to mass. The L16 and PQ12 actuators have ratios of 0.55 N/g and 1.67 N/g while the nitinol wires has a ratio of ~250 N/g. At this small scale, the ratio of force to mass is considerably higher for nitinol compared to the electric actuators. This allows for the case to be made that nitinol is a suitable replacement for conventional actuators at this scale.

CONCLUSIONS

The documented research was completed by accomplishing the three main goals stated in the outline of this thesis. The first goal was to design and build an airfoil capable of exploiting the material properties and characteristics of SMAs to change its camber when tested at low Reynolds number. Due to the proper placement of nitinol wires inside the airfoil and a simple electrical system, the airfoil was able to continuously and cyclically deform the last 33% of its chord without destruction of the airfoil or the nitinol wire. However, the nitinol wire did fail during experimental data collection. The failure was most likely due to current overload from the current source. The current overload would allow the nitinol wire to be overheated and reduce the material properties of the wire. For future implementation of the wire, safeguards to current overloads should be incorporated into the electrical system. The second achieved goal of the research was to improve the aerodynamic performance of the airfoil with the use of the SMA material during flight conditions. When the airfoil was actuated to its camber geometry, the predicted lift coefficient was approximately 0.4 larger than the symmetric airfoil for AoAs between 0 and 15 degrees. The planar PIV taken at 10, 12.5, and 15 degrees corroborated the lift predictions with the flow fields experiencing little separation for the tested AoAs of both airfoil geometries. Due to wingtip vortices generated on the ends of the airfoil, it was determined that an induced AoA was most likely between 2.5 and 3 degrees, so the critical AoA of either geometry was not evaluated. Due to a small discontinuity in the upper surface resulting filled with adhesive, the surface was not entirely smooth. Some of the flow structures generated may have resulted of the surface roughness generating vortices behind. For future research, it would be ideal to have a continuous smooth surface to eliminate potential surface roughness effects. The computational and experimental data for both geometries showed that the SMA actuated

airfoil is a viable flow control method. It also concludes that the cambered airfoil would be a preferred geometry during takeoff and landing flight conditions when a higher lift coefficient is required at lower speeds, and the symmetric airfoil would be ideal during cruising when the aircraft is at cruising speeds therefore not requiring a large AoA to maintain its altitude. The last accomplished goal of the research as to analyze the SMA airfoil for various wire actuation frequencies. Testing the airfoil at wire actuation frequencies of 0.33, 0.167, and 0.11 Hz showed that the frequency affects the flows recovery back to its original state. For a Re = 1*10^5 and frequency of 0.33 Hz, the flow was not able to return back to the flow corresponding with the symmetric geometry before the next actuation cycle occurred. Unlike 0.33 Hz, the 0.167 and 0.11 Hz data showed that the flow was able to return to its original flow field. This eludes to the flow field being dependent upon the inertial forces, viscous forces, and actuation frequency for this flow control method. Aside from the goals, the use of nitinol was also compared to electric actuators for the same scale airfoil. To apply the same force and displacement, the electric actuators examined weighed between 30 and 110 grams compared to the nitinol's .2 grams. On this scale, the nitinol proves to be a better actuation option based solely on the weight savings.

Overall, the research conducted was successful, but there are still areas of improvement/consideration for future research. The actuated airfoil was only tested for one wire placement location. Having several wire sets attached to different locations on the trailing surface of the airfoil would produce different results, so it is beneficial to determine the best location/s for the specific airfoil and flow condition. Another consideration for future research involving the SMA actuated airfoil is to alter the design to best allow for 3D deformation. 3D deformation, if designed properly, has potential to improve an airfoil's performance more than 2D deflection due to 3D unsteadiness experiences in the freestream velocity and the flow field

around the surface of the airfoil. The 3D unsteadiness of the flow field can allow for the flow to reattach at different locations along the airfoil. With a 3D geometry, capturing PIV measurements on the bottom surface of the airfoil would be required to fully understand the flow field around the airfoil. To accurately determine the 3D deflection, surface mapping could be incorporated into the experimental setup. Surface mapping routinely scans a surface for slight changes in vibration and geometry. This method would provide better correlations between the fluid and solid interactions. Continuing with 3D deformation and surface mapping is controlling the airfoil with a closed loop electrical system. The ideal active flow control method could adapt to any flow experienced by processing data transmitted from sensors fabricated into the airfoil and adjusting any flow alteration methods to optimize the aerodynamic performance. To do so, the active flow control method would have to be extensively tested for each achievable control to understand which is best for every scenario. The last research consideration is to increase the scale of the SMA airfoil. Some universities are currently working on making large scale wing sections using SMAs, but they only go as far as testing the geometry. There has been little research of wind tunnel testing with large scale SMA actuated airfoils.

REFERENCES

[1] Gad-el-Hak, M., 2001, Flow Control: Passive, Active and Reactive Flow Management.

[2] Stolt, A., Estevadeordal, J., Krech, J., and Zhang, Y., 2017, "A tomographic PIV and TSP Study of Leading-Edge Structures on Stall Behaviors of NACA 0015," AIAA SciTech 2017, AIAA, Grapevine, Texas.

[3] Anderson, J. D., 2001, Fundamentals of Aerodynamics, McGraw-Hill.

[4] Adrian, R. J., and Westerweel, J., 2011, Particle Image Velocimetry, Cambridge University Press, New York.

[5] Anderson, S., 2011, "LaVision Training."

[6] Srinivasan, A. V. V., and McFarland, D. M., 2000, Smart Structures: Analysis and Design, Cambridge University Press.

[7] Cai, Z., Chen, P., Angland, D., and Zhang, X., 2014, "Active flow separation control by a position-based iterative learning control algorithm with experimental validation," International Journal of Control, 87(3), pp. 633-641.

[8] Hecklau, M., van Rennings, R., Zander, V., Nitsche, W., Huppertz, A., and Swoboda, M., 2011, "Particle image velocimetry of active flow control on a compressor cascade," Experiments in Fluids, 50(4), pp. 799-811.

[9] Wang, G., Lewalle, J., Glauser, M., and Walczak, J., 2013, "Investigation of the benefits of unsteady blowing actuation on a 2D wind turbine blade," Journal of Turbulence, 14(1), pp. 165-189.

[10] Gul, M., Uzol, O., and Akmandor, I. S., 2014, "An Experimental Study on Active Flow Control Using Synthetic Jet Actuators over S809 Airfoil," Journal of Physics: Conference Series, 524(1), pp. 1-12.

[11] Tang, H., Salunkhe, P., Zheng, Y., Du, J., and Wu, Y., 2014, "On the use of synthetic jet actuator arrays for active flow separation control," Experimental Thermal and Fluid Science, 57, pp. 1-10.

[12] Walker, S., and Segawa, T., 2012, "Mitigation of flow separation using DBD plasma actuators on airfoils: A tool for more efficient wind turbine operation," Renewable Energy, 42, pp. 105-110.

[13] Francioso, L., Pascali, C. D., Pescini, E., Giorgi, M. G. D., and Siciliano, P., 2016, "Modeling, fabrication and plasma actuator coupling of flexible pressure sensors for flow separation detection and control in aeronautical applications," Journal of Physics D: Applied Physics, 49(23), pp. 1-14.

[14] Kotsonis, M., Pul, R., and Veldhuis, L., 2014, "Influence of circulation on a rounded-trailing-edge airfoil using plasma actuators," Experiments in Fluids, 55(7), pp. 1-14.

[15] Basaeri, H., Yousefi-Koma, A., Zakerzadeh, M. R., and Mohtasebi, S. S., 2014, "Experimental study of a bio-inspired robotic morphing wing mechanism actuated by shape memory alloy wires," Mechatronics, 24(8), pp. 1231-1241.

[16] Senthilkumar, M., 2012, "Analysis of SMA Actuated Plain Flap Wing," Journal of Engineering Science and Technology Review, 5(1), pp. 39-43.

[17] Roglin, R. L., and Hanagud, S. V., 1996, "A helicopter with adaptive rotor blades for collective control," Smart Materials and Structures, 5(1), pp. 76-88.

[18] Kang, W., Kim, E.-H., Jeong, M.-S., Lee, I., and Ahn, S.-M., 2012, "Morphing Wing Mechanism Using an SMA Wire Actuator," International Journal of Aeronautical and Space Sciences, 13(1), pp. 58-63.

[19] Pankonien, A. M., Duraisamy, K., Faria, C. T., and Inman, D., 201, "Synergistic Smart Morphing Aileron: Aero-structural Performance Analysis," 22nd AIAA/ASME/AHS Adaptive Structures Conference, American Institute of Aeronautics and Astronautics.

[20] Karagiannis, D., Spathopoulos, T., Stamatelos, D., Solomou, A., Machairas, T., Chrysohoidis, N., Saravanos, D., and Kappatos, V., 2014, "Airfoil morphing based on SMA actuation technology," Aircraft Engineering and Aerospace Technology: An International Journal, 86(4), pp. 295-306.

[21] Barbarino, S., G Dettmer, W., and Friswell, M., 2010, "Morphing Trailing Edges with Shape Memory Alloy Rods," 21st International Conference on Adaptive Structures and Technologies (ICAST) University Park, PA.

[22] Barbarino, S., Pecora, R., Lecce, L., Concilio, A., Ameduri, S., and Calvi, E. A., 2009, "A Novel SMA-based Concept for Airfoil Structural Morphing," Journal of Materials Engineering and Performance, 18(5), pp. 696-705.

[23] Barbarino, S., Pecora, R., Lecce, L., Concilio, A., Ameduri, S., and De Rosa, L., 2011, "Airfoil Structural Morphing Based on S.M.A. Actuator Series: Numerical and Experimental Studies," Journal of Intelligent Material Systems and Structures, 22(10), pp. 987-1004.

[24] Scheller, J., Jodin, G., Rizzo, K. J., Duhayon, E., Rouchon, J. F., Triantafyllou, M., and Braza, M., 2016, "A Combined Smart-Materials Approach for Next-Generation Airfoils," Solid State Phenomena, 251, pp. 106-112.

[25] Abdullah, E., Bil, C., and Watkins, S., 2010, "Testing of Adaptive Airfoil for UAV using Shape Memory Alloy Actuators," 27th International Congress Of The Aeronautical Sciences (ICAS), I. Poll, ed., International Congress of The Aeronautical Sciences, Sweden, pp. 1-9.

[26] Kancharala, A. K., 2008, "Design and Analysis of a Morphing Wing with Integrated Shape Memory Alloy Wires," Master of Engineering, Indian Institute of Science, Bangalore, India.

[27] Sinn, T., 2010, "Development of an Adaptive Flap/Flaperon Flight Control System with Shape Memory Alloy Actuation," M.S., University of Kansas.

[28] Strelec, J. K., Lagoudas, D. C., Khan, M. A., and Yen, J., 2003, "Design and Implementation of a Shape Memory Alloy Actuated Reconfigurable Airfoil," Journal of Intelligent Material Systems and Structures, 14(4-5), pp. 257-273.

[29] Dileep, E., Nebish, M., and Loganathan, V., 2013, "Aerodynamic Performance Optimization of Smart Wing Using SMA Actuator," Research Journal of Recent Sciences, 2(6), pp. 17-22.

[30] Hodgson, D. E., Wu, M. H., and Biermann, R., J., 1990, "Shape Memory Alloys," ASM Handbook, 2(Properties and Selection: Nonferrous Alloys and Special-Purpose Materials), pp. 897-902.

[31] DYNALLOY, I., 2018, "DYNALLOY, Inc. Makers of Dynamic Alloys", http://dynalloy.com/index.php.

[32] Inc., A. M. D., 2018, "Actuonix Motion Devices Inc.," https://www.actuonix.com/.

APPENDIX A. FIGURES

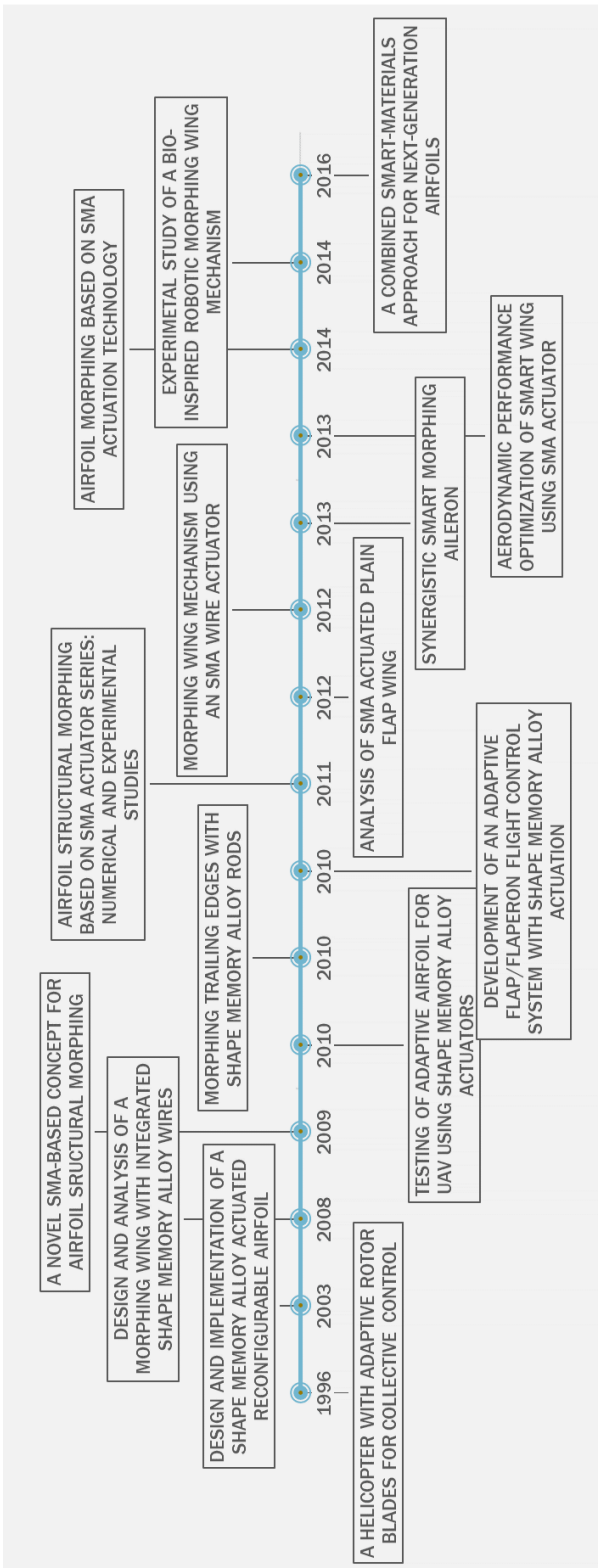

Figure A1. SMA Airfoil Research Timeline

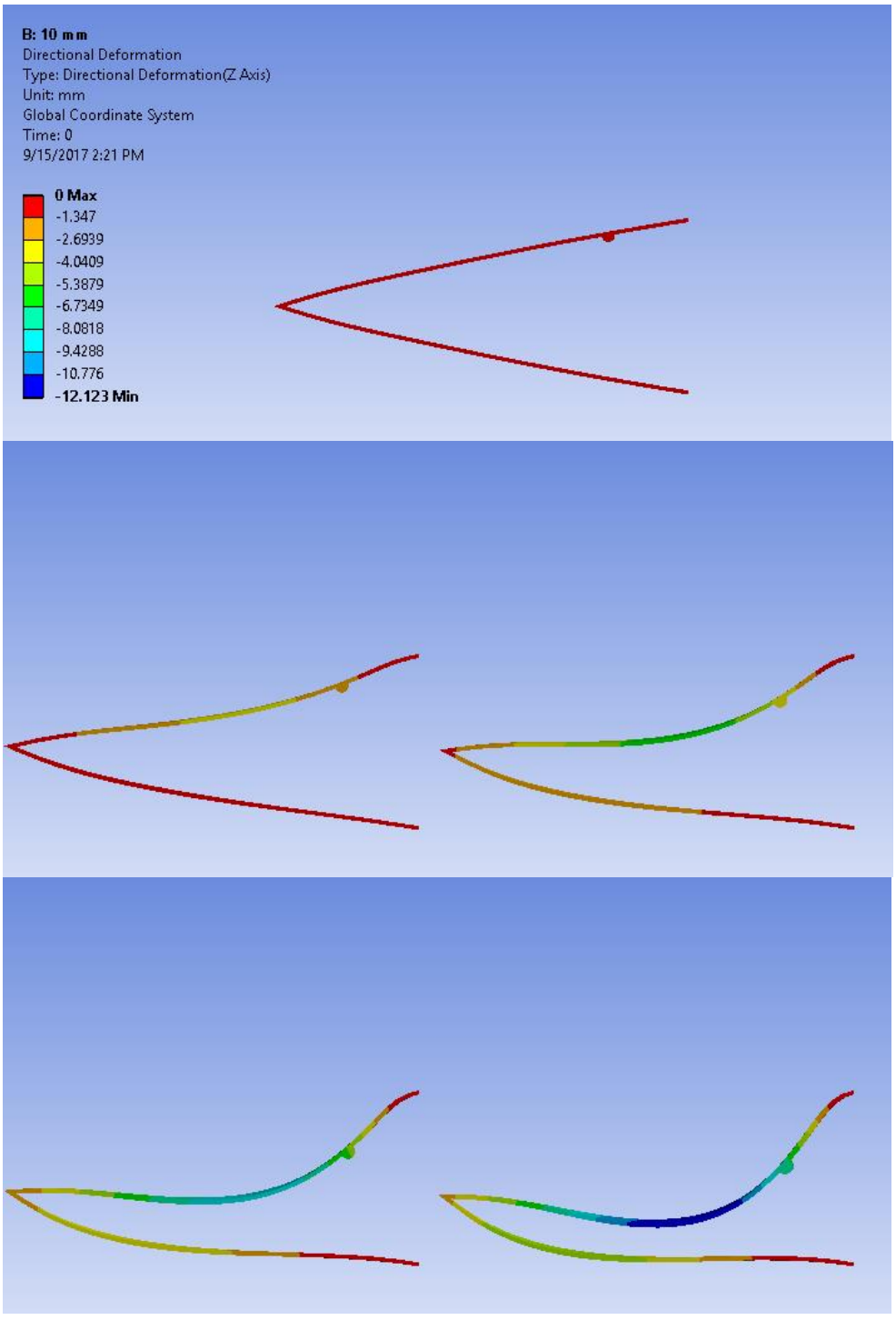

Figure A2. Deformation Steps for Wire Location 40 mm from Trailing Edge

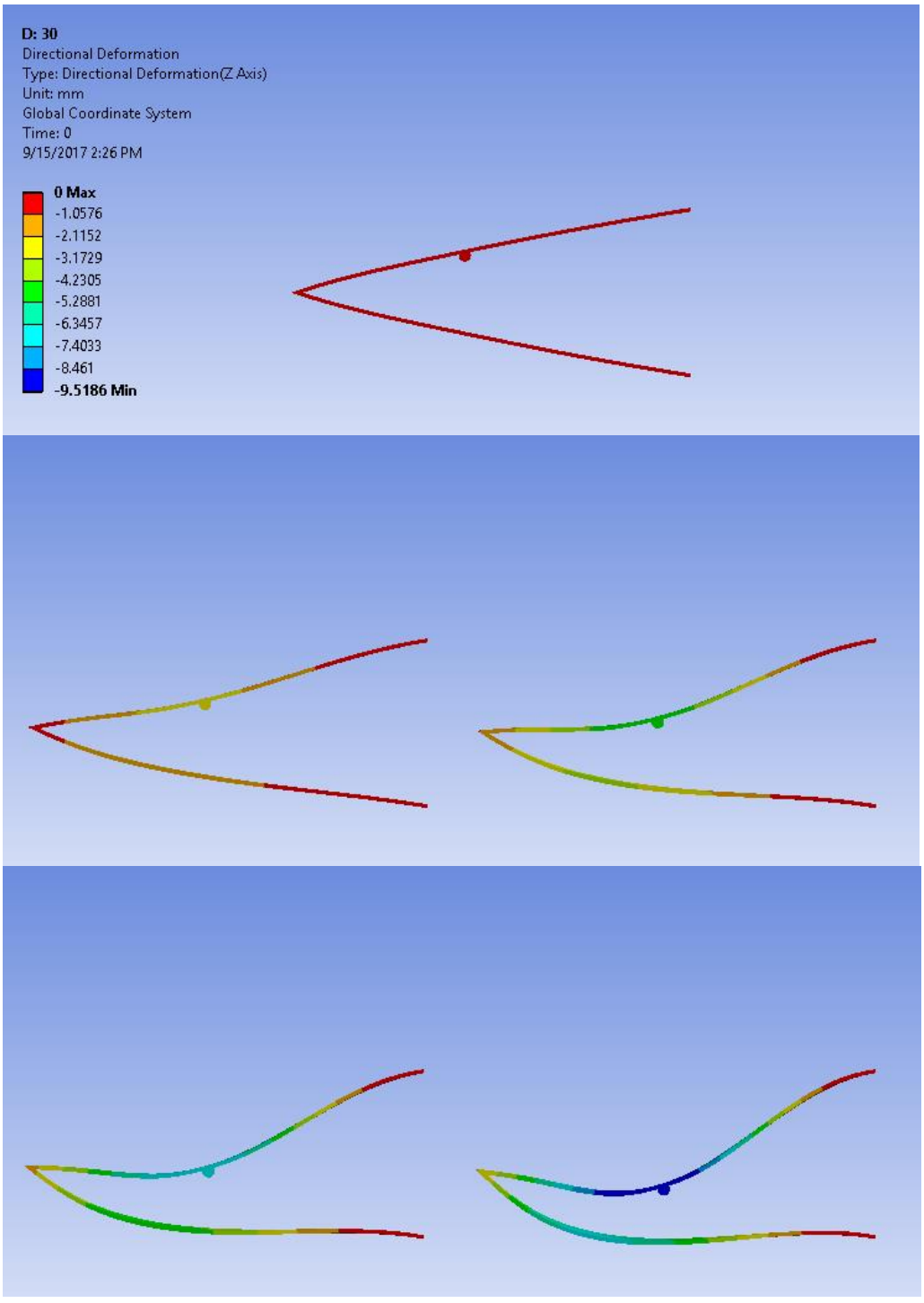

Figure A3. Deformation Steps for Wire Location 20 mm from Trailing Edge

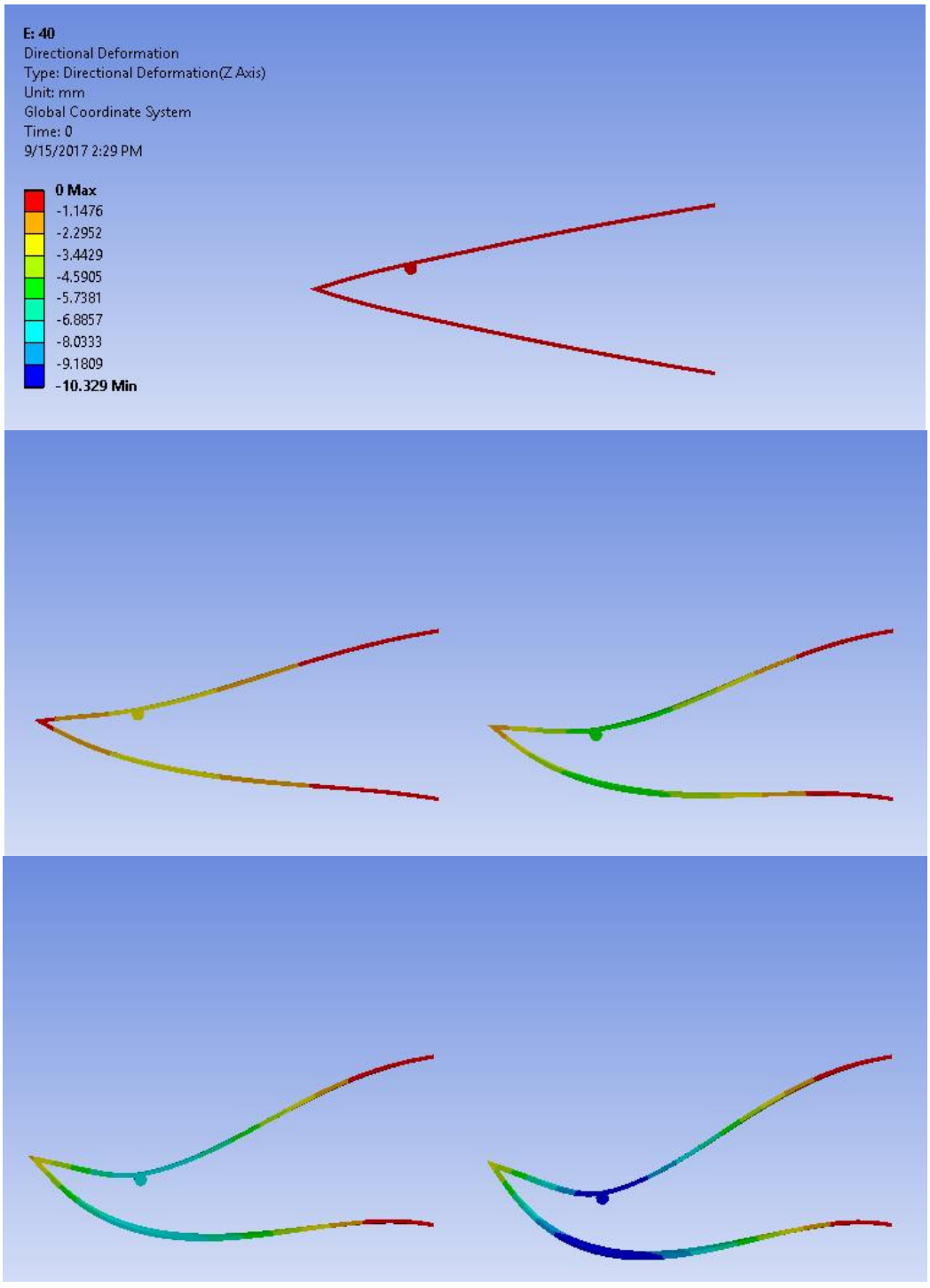

Figure A4. Deformation Steps for Wire Location 10 mm from Trailing Edge

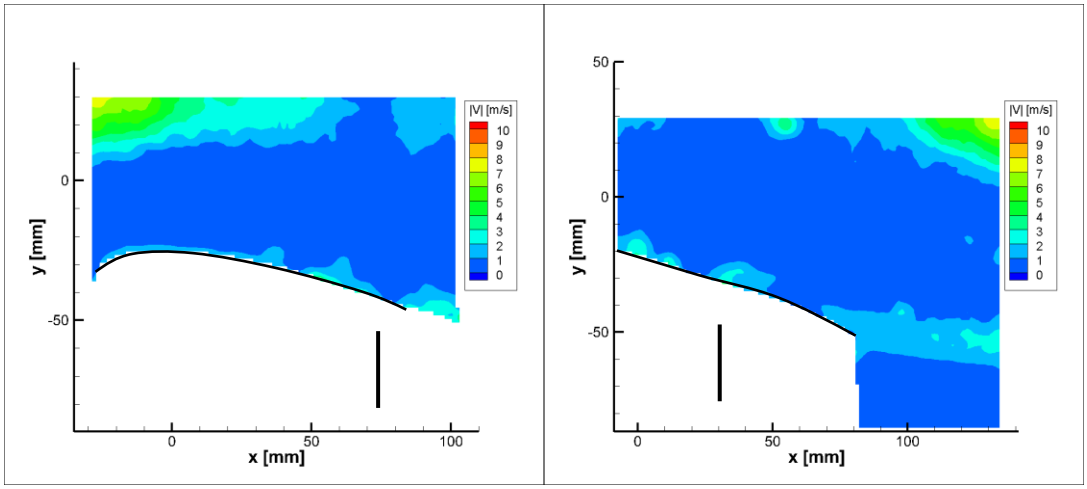

Figure A5. Time-Averaged Velocity Standard Deviation Profile of NACA 0021 Airfoil at 10 AoA Before Applied Actuation

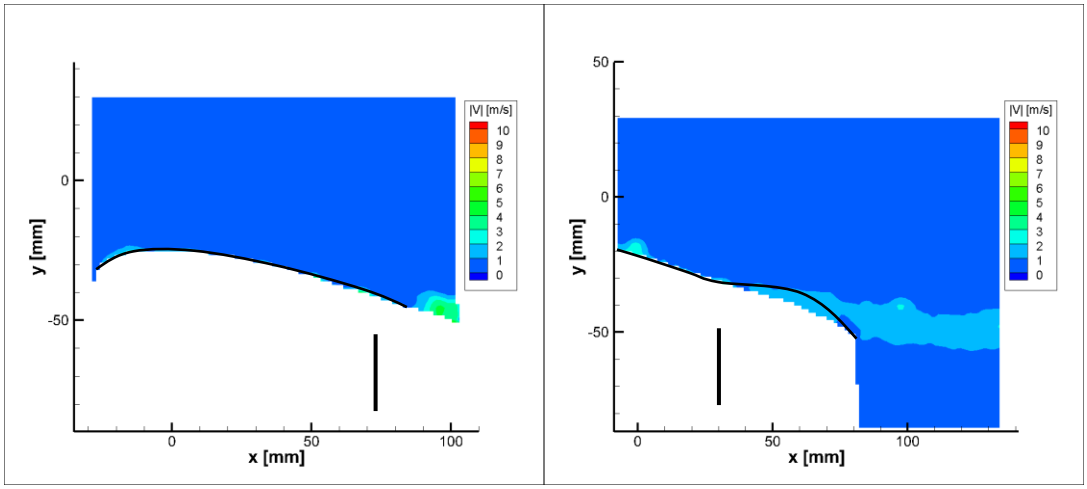

Figure A6. Time-Averaged Velocity Standard Deviation Profile of NACA 0021 Airfoil at 10 AoA During Applied Actuation

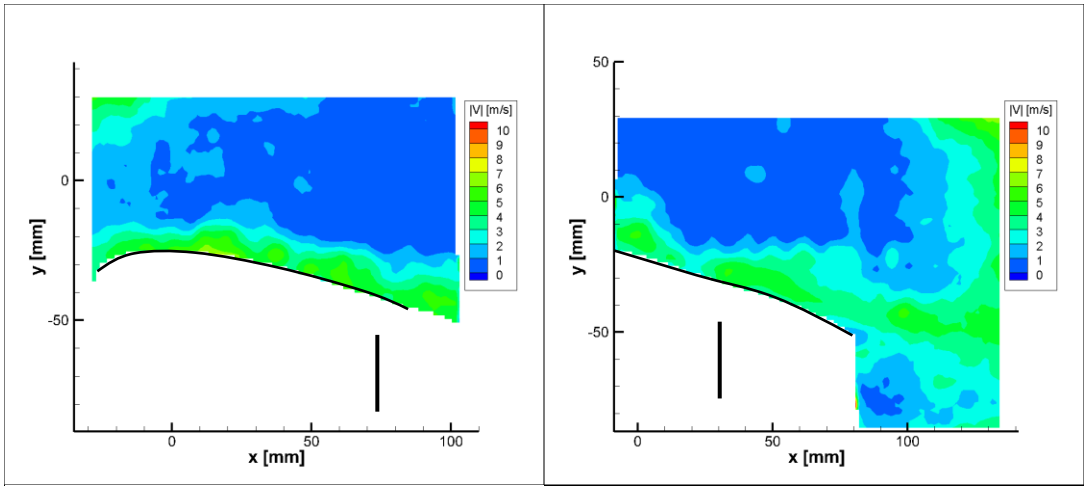

Figure A7. Time-Averaged Velocity Standard Deviation Profile of NACA 0021 Airfoil at 10 AoA After Applied Actuation

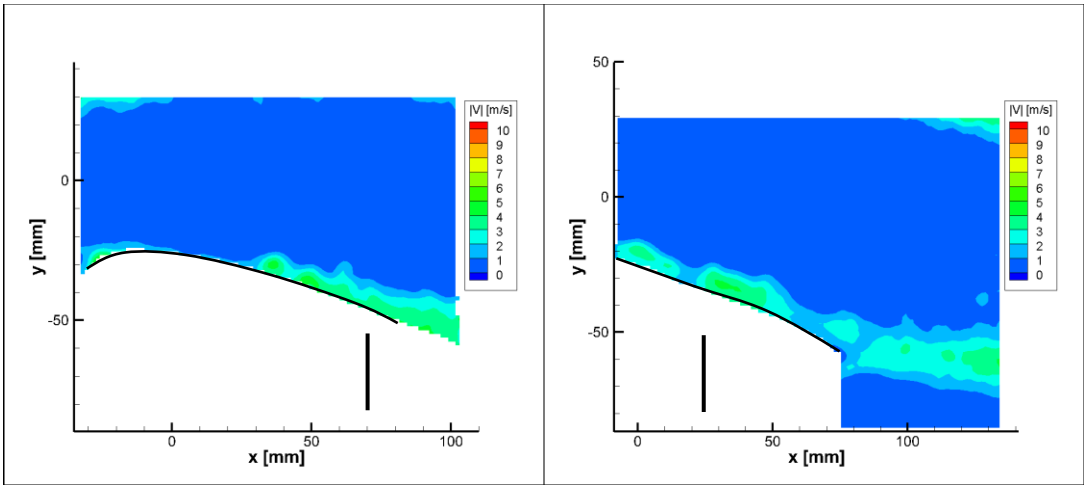

Figure A8. Time-Averaged Velocity Standard Deviation Profile of NACA 0021 Airfoil at 12.5 AoA Before Applied Actuation

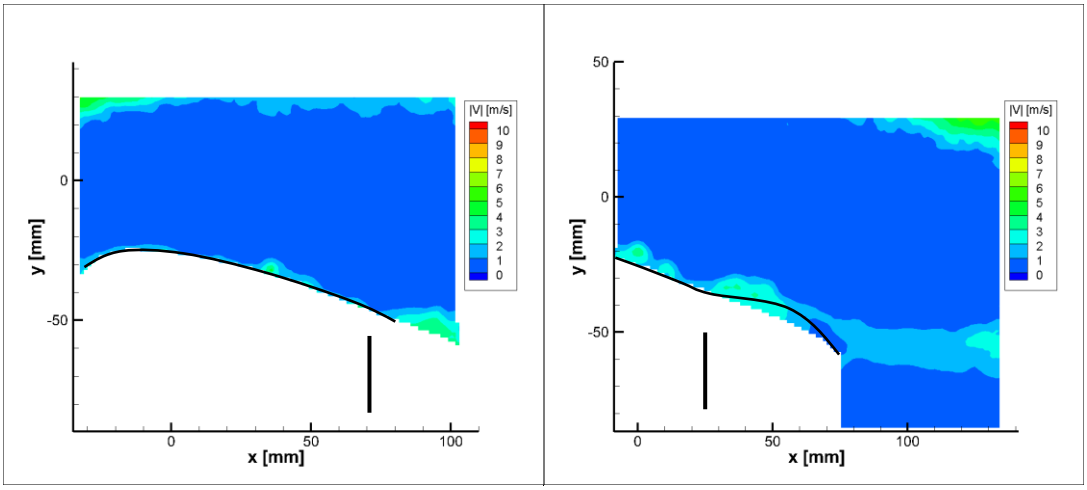

Figure A9. Time-Averaged Velocity Standard Deviation Profile of NACA 0021 Airfoil at 12.5 AoA During Applied Actuation

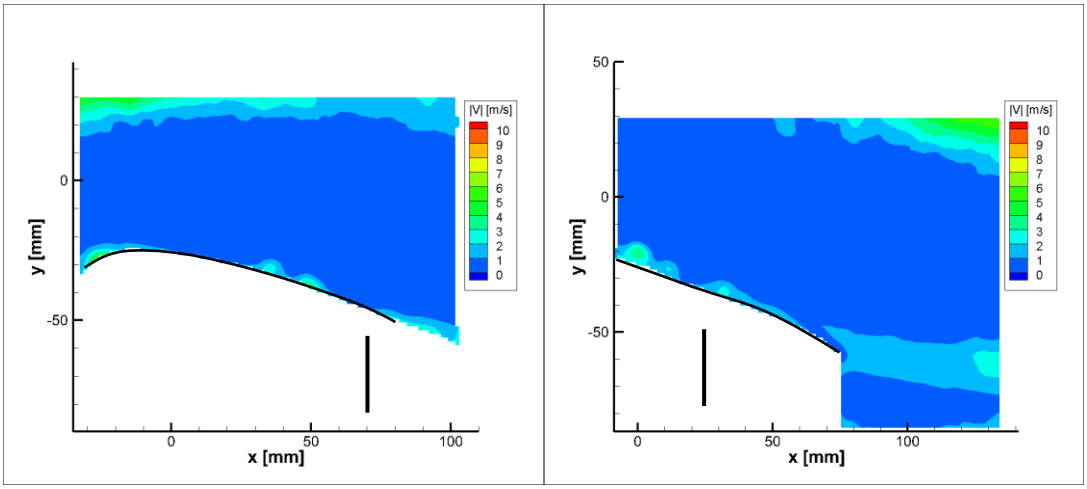

Figure A10. Time-Averaged Velocity Standard Deviation Profile of NACA 0021 Airfoil at 12.5 AoA After Applied Actuation

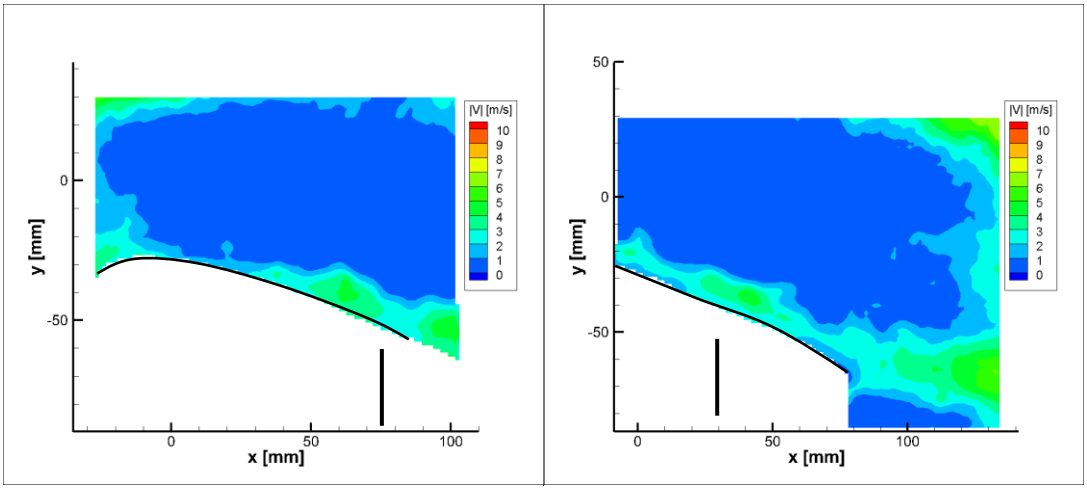

Figure A11. Time-Averaged Velocity Standard Deviation Profile of NACA 0021 Airfoil at 15 AoA Before Applied Actuation

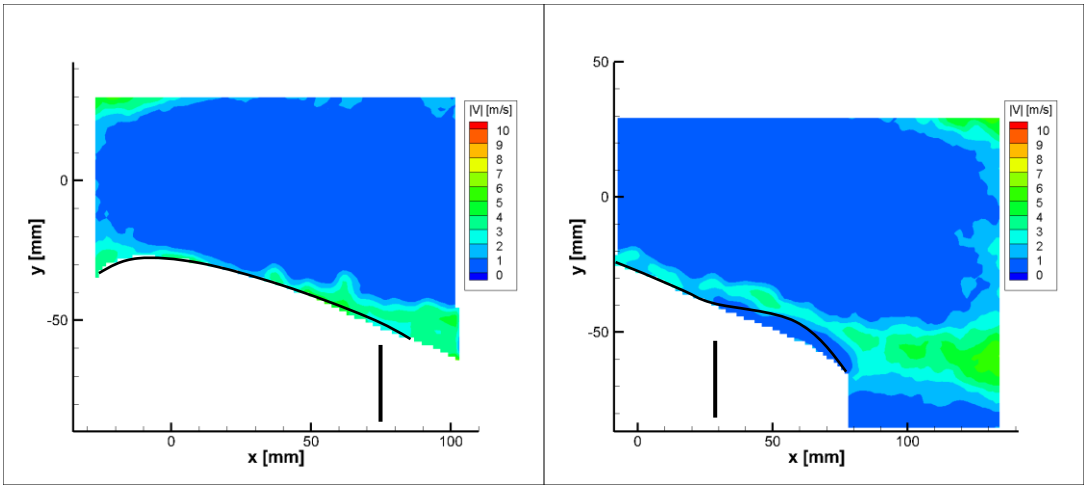

Figure A12. Time-Averaged Velocity Standard Deviation Profile of NACA 0021 Airfoil at 15 AoA During Applied Actuation

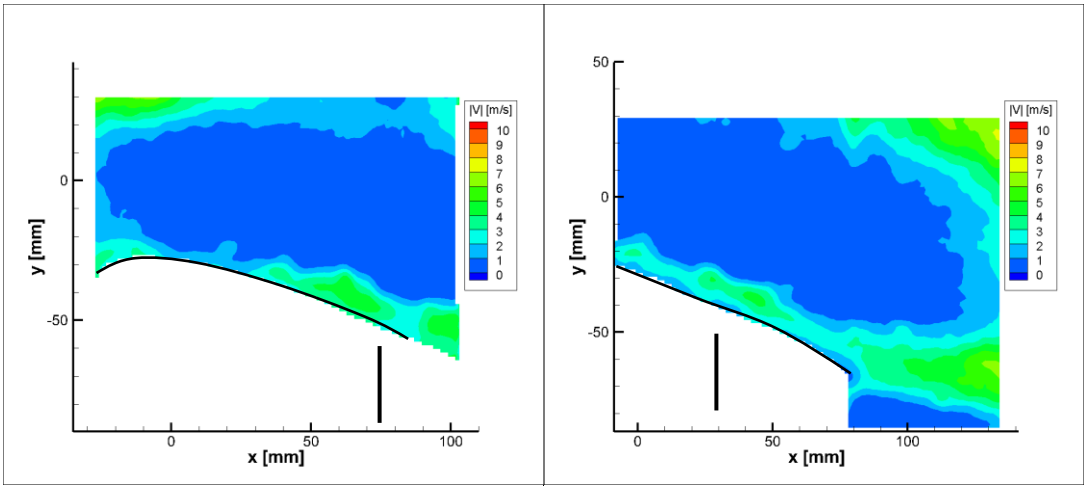

Figure A13. Time-Averaged Velocity Standard Deviation Profile of NACA 0021 Airfoil at 15 AoA After Applied Actuation

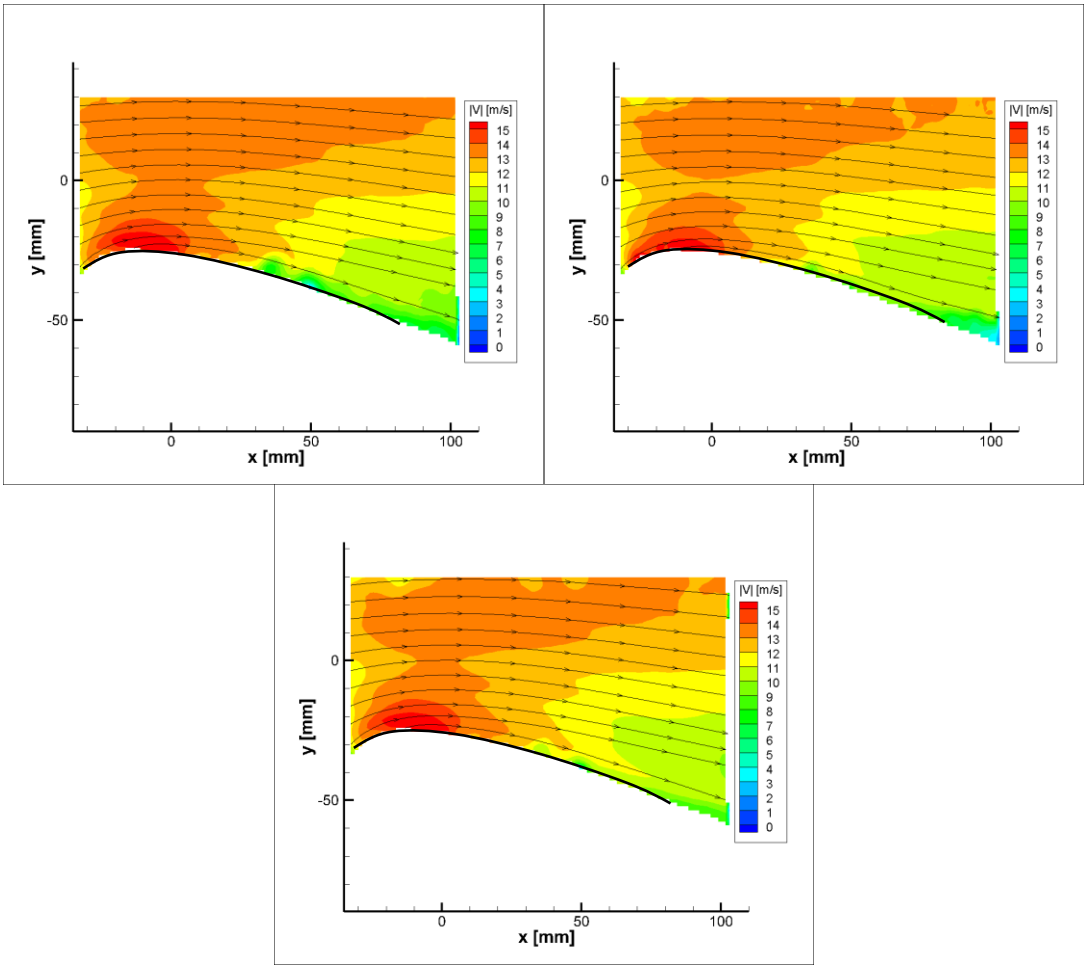

Figure A14. Time-Averaged Velocity Profile of NACA 0021 Airfoil at 12.5 AoA Before (top left), During (top right), and After (bottom) Actuation

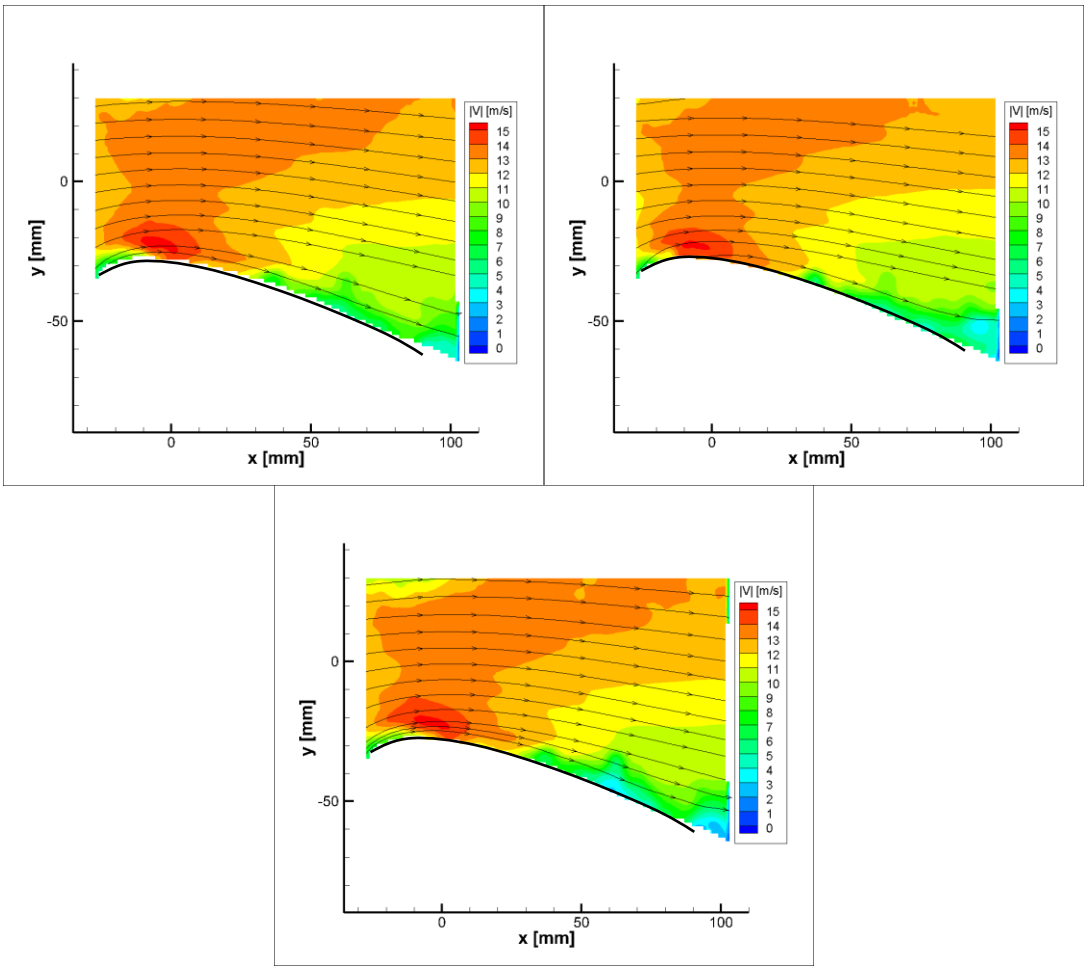

Figure A15. Time-Averaged Velocity Profile of NACA 0021 Airfoil at 15 AoA Before (top left), During (top right), and After (bottom) Actuation

100mm L16 – Actual Size

Miniature Linear Motion Series · L16

Actuonix Motion Devices' unique line of Miniature Linear Actuators enables a new generation of motion-enabled product designs, with capabilities that have never before been combined in a device of this size. These linear actuators are a superior alternative to designing your own push/pull mechanisms.

The L16 actuators are complete, self contained linear motion devices with position feedback for sophisticated position control capabilities, end of stroke limit switches for simple two position automation, or RC servo. Several gear ratios are available to give you varied speed/force configurations.

L16 Specifications

Gearing Option	35:1	63:1	150:1
Peak Power Point	50N @16mm/s	75N @10mm/s	175N @4mm/s
Peak Efficiency Point	24N @24mm/s	38N @15mm/s	75N @7mm/s
Max Speed (no load)	32mm/s	20mm/s	8mm/s
Max Force (lifted)	50N	100N	200N
Back Drive Force	31N	46N	102N
Stroke Option	**50mm**	**100mm**	**140mm**
Mass	56g	74g	84g
Repeatability (-P & LAC)	0.3mm	0.4mm	0.5mm
Max Side Load (extended)	40N	30N	20N
Closed Length (hole to hole)	118mm	168mm	218mm
Feedback Potentiometer	6kΩ±50%	11kΩ±50%	16kΩ±50%
Feedback Linearity	Less than 2.00%		
Input Voltage	0-15 VDC. Rated at 12VDC.		
Stall Current	650mA @ 12V		
Operating Temperature	-10°C to +50°C		
Audible Noise	60dB @ 45cm		
Ingress Protection	IP-54		
Mechanical Backlash	0.25mm		
Limit Switches	Max. Current Leakage: 8uA		
Maximum Static Force	250N		
Maximum Duty Cycle	20%		

Basis of Operation

The L16 is designed to push or pull a load along its full stroke length. The speed of travel is determined by the load applied. (See the Load Curves). Actuator speed can be reduced by lowering the drive voltage. When power is removed the actuator will hold its position, unless the applied load exceeds the back drive force. Repeated stalling or stalling for more than a few seconds will shorten the life of the actuator significantly. Stalling is when an actuator is pushing a load that it cannot move. Actuators should be tested in each specific application to determine their effective life under those loading conditions and environment.

Applications

- → **Robotics**
- → **Consumer appliances**
- → **Toys**
- → **RC vehicles**
- → **Automotive**
- → **Industrial Automation**

ACTUONIX MOTION DEVICES INC
Actuonix Motion Devices Inc
580 Starling Lane
Victoria, BC, V9E 2A9
Canada
1 (206) 347-9684 *phone*
1 (888) 225-9198 *toll-free*
1 (206) 347-9684 *fax*
sales@actuonix.com
www.actuonix.com

Figure A16. L16 Specifications Page 1 [32]

L16 Specifications

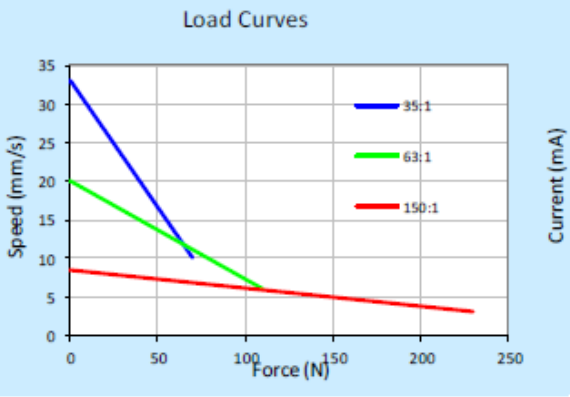

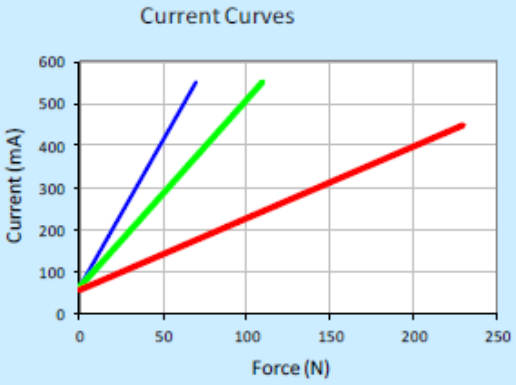

Model Selection

The L16 has 3 configuration choices: Stroke, Gear Ratio and Controller. L16 options are identified according to the following model numbering scheme:

L16-SS-GG-VV-C

Feature	*Options*
SS: Stroke	**50, 100, 140 (mm)**
GG: Gear reduction ratio (refer to load curves above)	**35, 63, 150** (lower ratios are faster but push less force, and vice versa)
VV: Voltage	**12** vdc or **6** vdc (-R only)
C: Controller	**P** Potentiometer Feedback **S** Limit Switches **R** RC Linear Servo

L16 Controller Options

Option S – End of Stroke Limit Switches

WIRING: (see last page for pin numbering)
1 - Red – Motor V+
2 – Black – Motor V- (Ground)

-S actuators are ideal for manually controlled applications and simple two position automated mechanisms. The –S actuators have limit switches that will turn off power to the motor when the actuator reaches within 0.5mm of the end of stroke. Internal diodes allow the actuator to reverse away from the limit switch. The limit switches cannot be moved once the actuator is manufactured. While voltage is applied to the motor power pins, (1 & 2) the actuator extends. Reverse the polarity and the actuator retracts. This can be accomplished manually with a DPDT switch or relay, or using an H-Bridge circuit. The –S model cannot be used with the LAC control board.

Option P – Potentiometer Position Feedback

WIRING: (see last page for pin numbering)
1 - Orange – Feedback Potentiometer negative reference rail
2 - Purple – Feedback Potentiometer wiper
3 - Red – Motor V+ (6V or 12V)
4 - Black – Motor V- (Ground)
5 - Yellow – Feedback Potentiometer positive reference rail

-P actuators are suited to automatically controlled positioning systems, but they can also be driven manually. The –P actuators have no built in controller, but do provide an analog position feedback signal that can be input to an external controller. While voltage is applied to the motor power pins, (3 & 4) the actuator extends. Reverse the polarity and the actuator retracts. This can be accomplished manually with a DPDT switch or relay, or using an H-Bridge circuit. Position of the actuator stroke can be monitored via the internal linear potentiometer. Provide any stable low and high reference voltage on pins 1 & 5, then read the position signal on pin 2. The voltage on pin 2 will vary linearly between the two reference voltages in proportion to the position of the actuator stroke.

The L16 –P actuator can be used as a linear servo by connecting the actuator to an external controller such as the LAC board offered by Firgelli. This control board reads the position signal from the L16, compares it with your input control signal then commands the actuator to move via an on-board H-bridge circuit. The LAC allows any one of the following control inputs: Analog 0-3.3V or 4-20mA, or Digital 0-5V PWM, 1-2ms Standard RC, or USB. The RC input effectively transforms your L16 into a linear servo, which is a direct replacement for any common hobby servo used in RC toys and robotics. Refer to the LAC datasheet for more details.

ACTUONIX MOTION DEVICES INC.
Actuonix Motion Devices Inc
580 Starling Lane
Victoria, BC, V9E 2A9
Canada
1 (206) 347-9684 *phone*
1 (888) 225-9198 *toll-free*
1 (206) 347-9684 *fax*
sales@actuonix.com
www.actuonix.com

Figure A17. L16 Specifications Page 2 [32]

Miniature Linear Motion Series · PQ12

PQ12 Actual Size

Actuonix Motion Devices unique line of Miniature Linear Actuators enables a new generation of motion-enabled product designs, with capabilities that have never before been combined in a device of this size. These tiny linear actuators are a superior alternative to designing your own push/pull mechanisms. Their low cost and easy availability make them attractive to hobbyists and OEM designers alike.

The PQ12 actuators are complete, self contained linear motion devices with position feedback for sophisticated position control capabilities, or end of stroke limit switches for simple two position automation. Driving them couldn't be easier, simply apply a DC voltage to extend the actuator, and reverse the polarity to retract it. Several gear ratios and voltage options are available to give you varied speed/force configurations.

Benefits

- → **Compact miniature size**
- → **Precise position feedback**
- → **Limit switches**
- → **Simple control**
- → **Low voltage**
- → **Equal push/pull force**
- → **Easy mounting**

Applications

- → **Robotics**
- → **Consumer appliances**
- → **Toys**
- → **RC vehicles**
- → **Automotive**
- → **Industrial Automation**

PQ12 Specifications

Gearing Option	30:1	63:1	100:1
Peak Power Point	15N@15mm/s	30N @ 8mm/s	40N @ 6mm/s
Peak Efficiency Point	8N @ 20mm/s	12N@12mm/s	20N @ 8mm/s
Max Speed (no load)	28mm/s	15mm/s	10mm/s
Max Force (lifted)	18N	45N	50N
Max Side Load	5N	10N	10N
Back Drive Force	9N	25N	35N
Stroke	20 mm		
Input Voltage	6 or 12 VDC		
Stall Current	550mA @ 6V, 210mA @ 12V		
Mass	15g		
Operating Temperature	-10°C to +50°C		
Positional Repeatability	±0.1mm		
Mechanical Backlash	0.25 mm		
Audible Noise	55dB @ 45cm		
Ingress Protection	IP-54		
Feedback Potentiometer	5kΩ±50%		
Limit Switches	Max. Current Leakage: 8uA		
Maximum Duty Cycle	20%		

Basis of Operation

The PQ12 is designed to push or pull a load along its full stroke length. The speed of travel is determined by the load applied (see load curves). When power is removed the actuator will hold its position, unless the applied load exceeds the back drive force. Repeated stalling of the actuator against a fixed load will shorten the life of the actuator. Since application conditions (Environmental, loading, duty cycle, vibration, etc) vary so widely, we advise application specific testing to determine the expected life of the actuator.

Ordering

Small quantity orders can be placed directly online at www.Actuonix.com. Each actuator ships with two mounting brackets, M3 mounting hardware, and one FPC ribbon cable connector. To extend the length of the ribbon cable you can purchase one of our PQ12 cable adapters and extension cable, or solder wires directly to the ribbon cable. Contact sales@Actuonix.com for volume quotes and customization options for OEM's.

ACTUONIX MOTION DEVICES INC
Actuonix Motion Devices Inc
580 Starling Lane
Victoria, BC, V9E 2A9
Canada
1 (206) 347-9684 *phone*
1 (888) 225-9198 *toll-free*
1 (206) 347-9684 *fax*
sales@actuonix.com
www.actuonix.com

Figure A18. PQ12 Specifications Page 1 [32]

PQ12 Specifications

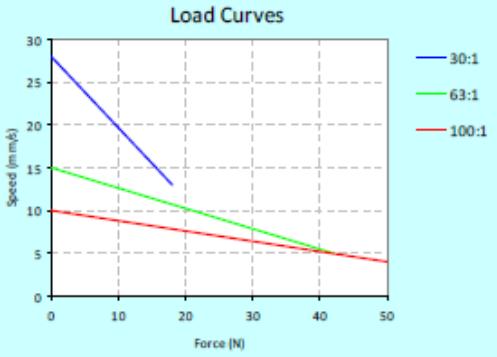

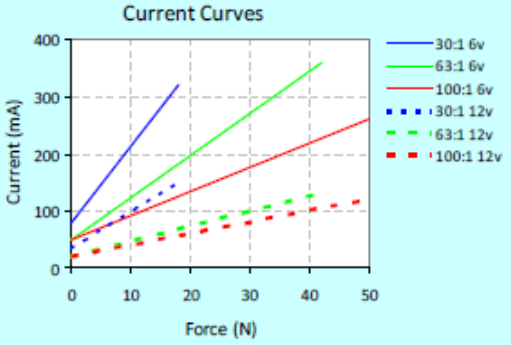

Model Selection

The PQ12 has 3 configuration choices: Gear Ratio, Voltage and Controller. PQ12 options are identified according to the following scheme:

PQ12-GG-VV-C

feature	*options*
GG: Gear reduction ratio (refer to load curves above)	**30, 63, 100** (lower ratios are faster but push less force, and vice versa)
VV: Voltage	**6, 12** (DC volts)
C: Controller	**P** Potentiometer Feedback **S** Limit Switches **R** RC Linear Servo (6V Only)

PQ12 Controller Options

Option S – End of Stroke Limit Switches

WIRING: (see next page for pin numbering)
1- Limit Switch Detection (Optional)
2- Actuator Motor Power
3- Actuator Motor Power
4- Not Connected
5- Not Connected

The –S actuators have limit switches that will turn off power to the motor when the actuator reaches within 1mm of the end of stroke. Internal diodes allow the actuator to reverse away from the limit switch. The limit switches cannot be moved. While voltage is applied to the motor power pins (2 & 3) the actuator extends. Reverse the polarity and the actuator retracts. This can be accomplished manually with a DPDT switch or relay, or using an H-Bridge circuit. The –S model cannot be used with the LAC control board. Pin #1 can be used to sense when the actuator has reached the end limits. See our FAQ page for a simple schematic to light an LED when the limits are reached.

Option P – Potentiometer Position Feedback

WIRING: (see next page for pin numbering)
1 – Feedback Potentiometer negative reference rail
2 – Actuator Motor Power
3 – Actuator Motor Power
4 – Feedback Potentiometer positive reference rail
5 – Feedback Potentiometer wiper

The –P actuators have no built in controller, but do provide analog position feedback. While voltage is applied to the motor power pins (2 & 3) the actuator extends. Reverse the polarity and the actuator retracts. Position of the actuator stroke can be monitored using the internal linear potentiometer. Provide any stable low and high reference voltage on pins 1 & 4, then read the position signal on pin 5. The voltage on pin 5 will vary linearly between the two reference voltages in proportion to the position of the actuator stroke. Connect to an LAC board for easy interface with any of the following control signals: Analog 0-5V or 4-20mA, or Digital 0-5V PWM, 1-2ms Standard RC, or USB.

Option R – RC Linear Servo

WIRING: (see last page for pin numbering)
1 - RC input signal (RC-servo compatible)
2 - Power (+6 VDC)
3 - Ground
Note: Reversing polarity on pins 2 and 3 may cause damage

-R actuators are ideally suited to use in robotics and radio control models. The –R actuators or 'linear servos' are a direct replacement for regular radio controlled hobby servos. The desired actuator position is input to the actuator on lead 1 as a positive 5 Volt pulse width signal. A 2.0 ms pulse commands the controller to fully retract the actuator, and a 1.0 ms pulse signals it to fully extend. If the motion of the actuator, or of other servos in your system, seems erratic, place a 1–4Ω resistor in series with the actuator's red V+ lead wire. The PQ12–R Linear Servos are designed to work with typical RC receivers and battery packs. Consequently, they also are compatible with Arduino control boards, VEX Microcontrollers and many other similar boards designed for robotics.

ACTUONIX MOTION DEVICES INC
Actuonix Motion Devices Inc
580 Starling Lane
Victoria, BC, V9E 2A9
Canada
1 (206) 347-9684 *phone*
1 (888) 225-9198 *toll-free*
1 (206) 347-9684 *fax*
sales@actuonix.com
www.actuonix.com

Figure A19. PQ12 Specifications Page 2 [32]

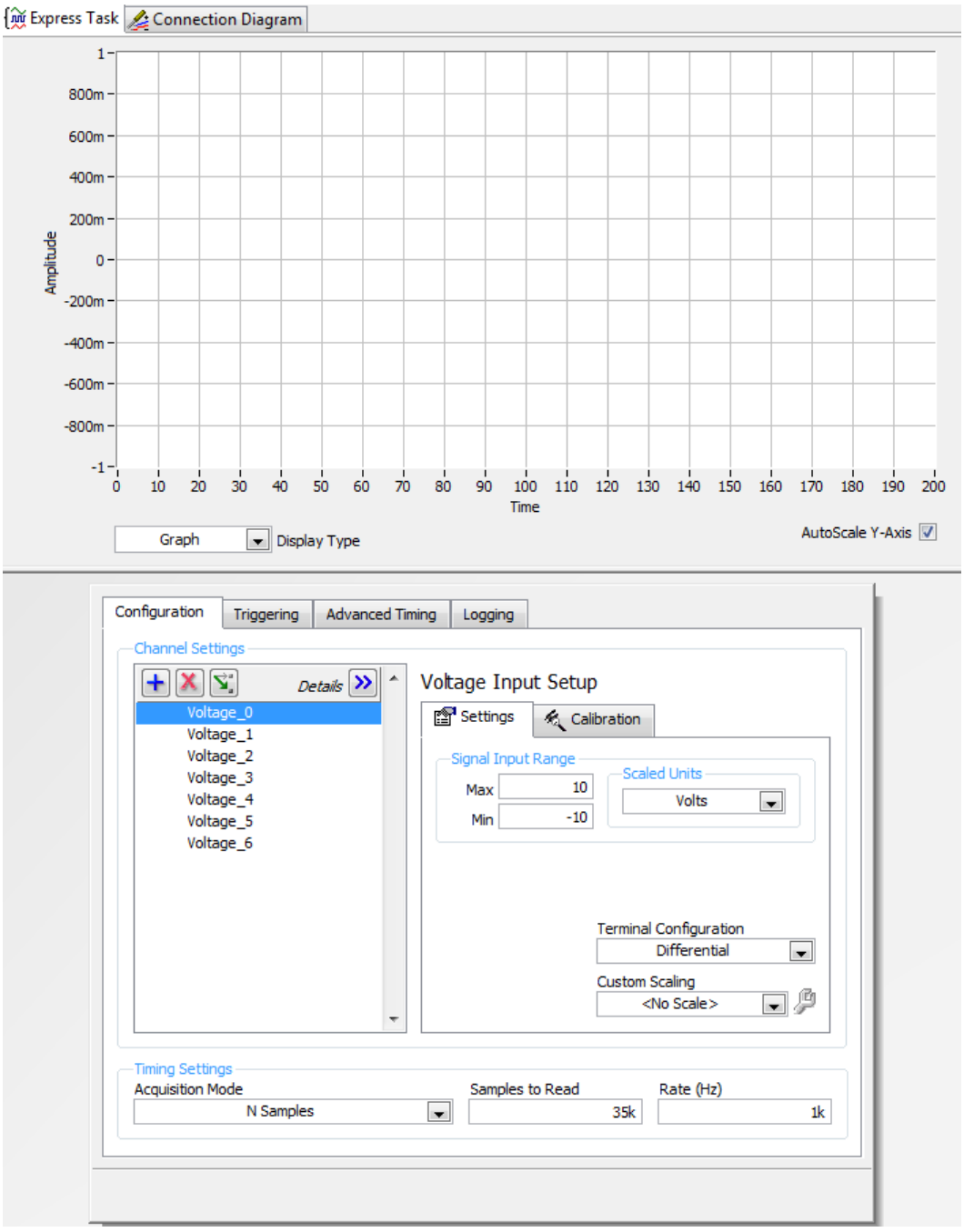

Figure A20. LabVIEW DAQ Assistant Settings Screen

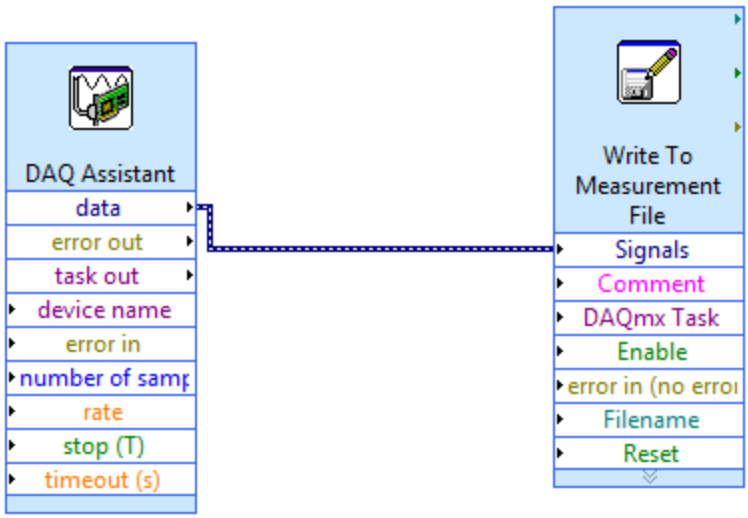

Figure A21. LabVIEW VI Setup

APPENDIX B. MATLAB ACTUATION CONTROL SCRIPTS

Baseline Geometry Actuation Script

```
clear all
clc

a = arduino('COM4','Uno');
pause(10)
writeDigitalPin(a,'D2',1);
pause(11)
writeDigitalPin(a,'D2',0)
pause(12)
disp('End experiment for this angle of attack');
```

0.33 Hz Actuation Script

```
clear all
clc

a = arduino('COM4','Uno');
pause(10)
writeDigitalPin(a,'D2',1);
pause(1)
writeDigitalPin(a,'D2',0)
pause(2)
writeDigitalPin(a,'D2',1);
pause(1)
writeDigitalPin(a,'D2',0);
pause(2)
disp('End experiment for this angle of attack');
```

0.167 Hz Actuation Script

```
clear all
clc

a = arduino('COM4','Uno');
pause(10)
writeDigitalPin(a,'D2',1);
pause(2)
writeDigitalPin(a,'D2',0)
pause(4)
writeDigitalPin(a,'D2',1);
pause(2)
writeDigitalPin(a,'D2',0);
pause(4)
disp('End experiment for this angle of attack');
```

0.11 Hz Actuation Script

```
clear all
clc

a = arduino('COM4','Uno');
pause(10)
writeDigitalPin(a,'D2',1);
pause(3)
writeDigitalPin(a,'D2',0)
pause(6)
writeDigitalPin(a,'D2',1);
pause(3)
writeDigitalPin(a,'D2',0);
pause(6)
disp('End experiment for this angle of attack');
```